
Theses and Dissertations

Spring 2010

Applications and physicochemical characterization of nanomaterials in environmental, health, and safety studies

Sherrie Renee Elzey
University of Iowa

Follow this and additional works at: <https://ir.uiowa.edu/etd>

 Part of the [Chemical Engineering Commons](#)


Copyright © 2010 Sherrie Renee Elzey

This dissertation is available at Iowa Research Online: <https://ir.uiowa.edu/etd/494>

Recommended Citation

Elzey, Sherrie Renee. "Applications and physicochemical characterization of nanomaterials in environmental, health, and safety studies." PhD (Doctor of Philosophy) thesis, University of Iowa, 2010.
<https://doi.org/10.17077/etd.l1uc5e5i>

Follow this and additional works at: <https://ir.uiowa.edu/etd>

 Part of the [Chemical Engineering Commons](#)

APPLICATIONS AND PHYSICOCHEMICAL CHARACTERIZATION OF
NANOMATERIALS IN ENVIRONMENTAL, HEALTH, AND SAFETY STUDIES

by

Sherrie Renee Elzey

An Abstract

Of a thesis submitted in partial fulfillment of the
requirements for the Doctor of Philosophy degree
in Chemical and Biochemical Engineering in
the Graduate College of
The University of Iowa

May 2010

Thesis Supervisor: Professor Vicki H. Grassian

ABSTRACT

As commercially manufactured nanomaterials become more commonplace, they have the potential to enter ecological and biological environments during their lifecycle of production, distribution, use or disposal. Despite rapid advances in the production and application of nanomaterials, little is known about how they may interact with the environment or affect human health. This research investigates an environmental application of nanomaterials and characterizes physicochemical properties of commonly manufactured nanomaterials in environmental, health, and safety studies.

Characterization of nanomaterials for applications and environmental health and safety studies is essential in order to understand how physicochemical properties correlate with chemical, ecological, or biological response or lack of response. Full characterization includes determining the bulk (shape, size, phase, electronic structure and crystallinity) and surface (surface area, arrangement of surface atoms, surface electronic structure, surface composition and functionality) properties of nanomaterials.

This work investigates the selective catalytic reduction (SCR) of NO_2 to N_2 and O_2 with ammonia on nanocrystalline NaY, Aldrich NaY and nanocrystalline CuY using in situ Fourier transform infrared (FTIR) spectroscopy. The kinetics of SCR were 30% faster on nanocrystalline NaY compared to commercial NaY due to an increase in external surface area and external surface reactivity. Nanocrystalline CuY showed an additional increase in the rate of SCR as well as distinct NO_2 and NH_3 adsorption sites associated with the copper cation. These superior de- NO_x materials could contribute to a cleaner environment.

This work consists of characterization of commonly manufactured or synthesized nanomaterials and studies of nanomaterials in specific environmental conditions. Bulk and surface characterization techniques were used to examine carbon nanotubes, titanium dioxide nanoparticles, bare silver nanoparticles and polymer-coated silver nanoparticles, and copper nanoparticles. Lithium titanate nanomaterial collected from a manufacturing facility was also characterized to identify occupational health risks. Particle size distribution measurements and chemical composition data showed the lithium titanate nanomaterial forms larger micrometer agglomerates, while the nanoparticles present were due to incidental processes.

A unique approach was applied to study particle size during dissolution of nanoparticles in aqueous and acidic conditions. An electrospray coupled to a scanning mobility particle sizer (ES-SMPS) was used to determine the particle size distribution of bare silver nanoparticles in nitric acid and copper nanoparticles in hydrochloric acid. The results showed size-dependent dissolution behavior. Size-dependent properties of nanomaterials may influence transport and transformation, and the behavior of larger sized materials cannot be used to predict nanomaterial behavior. The type of nanomaterial and the media it enters are important factors for determining the fate of the nanomaterial. These studies will be important when considering measures for exposure control and environmental remediation of nanomaterials.

Abstract Approved: _____
Thesis Supervisor

Title and Department

Date

APPLICATIONS AND PHYSICOCHEMICAL CHARACTERIZATION OF
NANOMATERIALS IN ENVIRONMENTAL, HEALTH, AND SAFETY STUDIES

by

Sherrie Renee Elzey

A thesis submitted in partial fulfillment of the
requirements for the Doctor of
Philosophy degree in Chemical and Biochemical Engineering in
the Graduate College of
The University of Iowa

May 2010

Thesis Supervisor: Professor Vicki H. Grassian

Copyright by
SHERRIE RENEE ELZEY
2010
All Rights Reserved

Graduate College
The University of Iowa
Iowa City, Iowa

CERTIFICATE OF APPROVAL

PH.D. THESIS

This is to certify that the Ph. D. thesis of

Sherrie Renee Elzey

has been approved by the Examining Committee for the thesis requirement for the Doctor of Philosophy degree in Chemical and Biochemical Engineering at the May 2010 graduation.

Thesis Committee: _____
Vicki H. Grassian, Thesis Supervisor

C. Allan Guymon

Amanda J. Haes

Tonya Peebles

Charles Stanier

To Michael
Scientia Est Potentia

ACKNOWLEDGEMENTS

I want to thank my advisor, Dr. Vicki H. Grassian, for her guidance and mentoring throughout my Ph. D. I also want to thank Dr. Allan Guymon, Dr. Amanda Haes, Dr. Tonya Peebles, and Dr. Charles Stanier for serving on my committee. I am grateful to all the Grassian group members and collaborators I have had the opportunity to work with and learn from. Thanks to Ashley D'Ann Koh, my friend in the highs and lows of graduate school. Thanks to my husband, Michael Belverud, for inspiring me everyday.

TABLE OF CONTENTS

LIST OF TABLES	viii
LIST OF FIGURES	ix
LIST OF ABBREVIATIONS	xiv
CHAPTER	
1. INTRODUCTION	1
1.1 Nanomaterial Properties	1
1.2 Nanomaterial Applications	2
1.3 Environmental and Health Considerations of Nanomaterials	3
1.4 Challenges and Needs for Addressing Nanotechnology Risks	9
1.5 Introduction to Thesis Chapters	11
2. RESEARCH OBJECTIVES	17
3. MATERIALS AND METHODS	20
3.1 Introduction	20
3.2 Sources of Research Materials	20
3.2.1 Sources of Nanomaterials and Micromaterials	20
3.2.2 Sources of Reagents	20
3.3 Characterization Techniques	23
3.3.1 Bulk Characterization Techniques	23
3.3.2 Surface Characterization Techniques	24
3.4 Sample Preparation for Characterization and Experiments	24
3.4.1 SEM and TEM/EDX Microscopy	24
3.4.2 BET Specific Surface Area Analysis	25
3.4.3 Transmission FTIR Spectroscopy	25
3.4.4 Raman Spectroscopy for Carbon Nanotube Characterization	27
3.4.5 Off-line Filter Analysis of Lithium Titanate Metal Oxide Nanomaterial	27
3.4.6 X-ray Photoelectron Spectroscopy	28
3.4.7 Powder X-ray Diffraction	29
3.4.8 Zeta Potential	29
3.4.9 Inductively Coupled Plasma/Optical Emission Spectroscopy	30
3.4.10 Electrospray-Scanning Mobility Particle Sizer	30
4. CHARACTERIZATION OF NANOMATERIALS	39
4.1 Introduction	39
4.2 Characterization Methods	40

4.3 Carbon Nanotube Characterization	40
4.3.1 Microscopy and Specific Surface Area Analysis	40
4.3.2 Raman Spectroscopy	44
4.3.3 X-ray Photoelectron Spectroscopy	45
4.3.4 Summary of Carbon Nanotube Results	45
4.4 Polymer-Coated Silver Nanoparticle Size Characterization	47
4.5 Titanium Dioxide and Polymer-Coated Silver Nanoparticle Characterization	49
4.6 Synthesized Gold Nanoparticle Characterization	54
4.6.1 Silica-Coated Gold Nanoparticles	54
4.6.2 Sodium Citrate Stabilized Gold Nanoparticles	57
4.7 Summary of Nanomaterial Characterization	62
4.8 Acknowledgements	62
5. AIRBORNE MONITORING TO DISTINGUISH ENGINEERED NANOMATERIALS FROM INCIDENTAL PARTICLES FOR ENVIRONMENTAL HEALTH AND SAFETY	63
5.1 Introduction	63
5.2 Methods	64
5.2.1 Manufacturing Facility	64
5.2.2 Off-Line Filter Based Analysis	65
5.2.3 Real Time Activity Based Monitoring	66
5.3 Results	66
5.3.1 Off-Line Filter Based Analysis	66
5.3.2 Real Time Activity Based Monitoring	67
5.4 Discussion	73
5.5 Conclusions	74
5.6 Acknowledgements	75
6. SELECTIVE CATALYTIC REDUCTION OF NO ₂ WITH AMMONIA USING NANOCRYSTALLINE NaY AND CuY ZEOLITES	76
6.1 Introduction	76
6.2 Experimental Methods	79
6.2.1 Synthesis and Copper Exchange of Nanocrystalline NaY	79
6.2.2 Characterization of Zeolites	80
6.2.3 FTIR Experiments	82
6.3 Results	83
6.3.1 Characterization of Zeolites	83
6.3.2 Adsorption of NO ₂ at T = 298 K	86
6.3.3 Adsorption of NH ₃ at T = 298 K	89
6.3.4 NH ₃ -SCR of NO ₂ at T = 298 K: Gas Phase	93
6.3.5 NH ₃ -SCR of NO ₂ at T = 298 K: Surface Species	96
6.3.6 Nanocrystalline Zeolites: NaY vs. CuY	97
6.4 Discussion	100

6.4.1	NH ₃ -SCR of NO ₂ : Reactions Between NO ₂ and NH ₃	100
6.4.2	Nanocrystalline CuY: Cationic Interactions	102
6.4.3	Temperature Effects	104
6.5	Conclusions	104
6.6	Acknowledgements	106
7.	AGGLOMERATION, ISOLATION AND DISSOLUTION OF COMMERCIALY MANUFACTURED SILVER NANOPARTICLES IN AQUEOUS ENVIRONMENTS	107
7.1	Introduction	107
7.2	Experimental Methods	109
7.2.1	Materials	109
7.2.2	Powder X-ray Diffraction	109
7.2.3	X-ray Photoelectron Spectroscopy	109
7.2.4	BET Specific Surface Area Analysis	109
7.2.5	Transmission Electron Microscopy	110
7.2.6	Electrospray-Scanning Mobility Particle Sizer	110
7.2.7	Zeta Potential Measurements	112
7.2.8	Inductively Coupled Plasma/Optical Emission Spectroscopy	112
7.3	Results and Discussion	112
7.3.1	Characterization of Commercially Manufactured Silver Nanoparticles in the Dry State with XRD, XPS, BET, and TEM	112
7.3.2	ES-SMPS Analysis of Aqueous Suspensions of Silver Nanoparticles	117
7.3.3	In Situ Measurements Using Complementary Techniques Including Zeta Potential Measurements and ICP/OES	122
7.3.4	Environmental Implications	127
7.4	Acknowledgments	131
8.	NANOPARTICLE DISSOLUTION FROM THE PARTICLE PERSPECTIVE: INSIGHTS ON NANOSCALE PROCESSES FROM PARTICLE SIZING MEASUREMENTS	132
8.1	Introduction	132
8.2	Experimental Methods	133
8.3	Results and Discussion	133
8.4	Conclusions	138
8.5	Acknowledgements	139
9.	COPPER-BASED NANOPARTICLE TRANSITION TO PARATACAMITE NANOPARTICLES USING HYDROCHLORIC ACID	140
9.1	Introduction	140
9.2	Experimental Methods	142

9.2.1	Materials	142
9.2.2	Electrospray-Scanning Mobility Particle Sizer	142
9.2.3	High-Resolution Transmission Electron Microscopy	142
9.2.4	Powder X-ray Diffraction	143
9.3	Results and Discussion	143
9.3.1	Electrospray-Scanning Mobility Particle Sizer	143
9.3.2	Copper Color Transitions in Hydrochloric Acid Solutions	143
9.3.3	High-Resolution Transmission Electron Microscopy	146
9.3.4	Powder X-ray Diffraction	146
9.4	Conclusions	152
9.5	Acknowledgements	153
10. CONCLUSIONS AND FUTURE DIRECTIONS		154
REFERENCES		160

LIST OF TABLES

Table 3.1	Source of Nanomaterials and Micromaterials with Specifications Provided by the Manufacturer or Synthesis Research Laboratory	21
Table 3.2	Source of Reagents	22
Table 3.3	Instrumentation for Bulk Characterization	23
Table 3.4	Instrumentation for Surface Characterization	24
Table 4.1	XPS Analysis of Carbon Nanotubes	45
Table 4.2	Characterization Summary for Carbon Nanotubes	46
Table 4.3	Predicted and Experimental ES-SMPS Particle Size for Gold Nanoparticles in Sodium Citrate Solutions Based on Calculated Citrate Double Layer Thickness	59
Table 5.1	Respirable Mass Concentration and Percent of Respirable Mass Concentration Lithium Titanate by Location	68
Table 6.1	Properties of Synthesized Nanocrystalline NaY and CuY and Aldrich NaY	84
Table 6.2	Assignment of Absorbance Bands Resulting from NO ₂ Adsorption on Commercial NaY, Nanocrystalline NaY and Nanocrystalline CuY	88
Table 6.3	Assignment of Absorbance Bands Resulting from NH ₃ Adsorption on Commercial NaY, Nanocrystalline NaY and Nanocrystalline CuY	92
Table 6.4	Comparison of Initial Rates of Reactions for NH ₃ -SCR of NO ₂ Over Commercial NaY, Nanocrystalline NaY and Nanocrystalline CuY	99
Table 7.1	Summary of Analysis for Silver Nanoparticles Suspended in Water and Aqueous Nitric acid solutions	126

LIST OF FIGURES

Figure 1.1	Commonly manufactured nanomaterials by percentage.	3
Figure 1.2	Nanomaterial properties that can affect characterization measurements.	10
Figure 3.1	Transmission FTIR experimental system.	26
Figure 3.2	Schematic of an electrospray aerosol generator coupled to a scanning mobility particle sizer.	30
Figure 4.1	Selected images of single walled carbon nanotubes, SEM (A, B) and TEM (C, D).	41
Figure 4.2	Selected images of multi-walled carbon nanotubes, SEM (A, B) and TEM (C, D).	42
Figure 4.3	Diameter size distributions from TEM analysis for single walled carbon nanotubes (A) and multi-walled carbon nanotubes (B).	43
Figure 4.4	Raman spectra of single walled carbon nanotubes (upper) and multi-walled carbon nanotubes (lower). RBM = Radial Breathing Mode, G Band = Tangential Mode, D Band = Disorder-induced Mode, and D* Band = Overtone (2*D).	44
Figure 4.5	TEM image (left) and corresponding particle size distribution (right) for polymer-coated silver nanoparticles.	48
Figure 4.6	ES-SMPS particle size distribution of polymer-coated silver nanoparticles.	48
Figure 4.7	5-nm TiO ₂ and ~6-11-nm Ag aerosol concentration over time produced by water-based electrospray method.	51
Figure 4.8	5-nm TiO ₂ , ~6-11-nm Ag plus polymer coating, and background water size distributions produced by an electrospray generator.	53
Figure 4.9	TEM images of silica-coated gold nanoparticles (A, B). Particle size distributions for bare (C), and silica-coated gold nanoparticles (D).	56
Figure 4.10	ES-SMPS size distributions for bare and silica-coated gold nanoparticles suspended in a 40 nM sodium citrate solution.	57
Figure 4.11	ES-SMPS results for gold nanoparticle suspensions (red) and corresponding sodium citrate background (black).	60

Figure 4.12	Peak maxima for gold nanoparticles in sodium citrate (Au@Citrate in NaCitrate) and sodium citrate solutions (NaCitrate Background) as a function of sodium citrate concentration.	61
Figure 5.1	Facility layout showing sampling locations (filled dots).	65
Figure 5.2	Electron microscopy images from filter samples depict particle size and morphology. a,b, TEM images show three types of particles of different shape and size: large spherically shaped particles (b,1); irregularly shaped particles (b,2); and smaller particle chains (b,3). c-e, SEM images reveal that the larger spherical particles are actually composed of smaller nanoparticles 10-80 nm in size interwoven into larger aggregates (c,d); irregularly shaped particles have an amorphous structure (e); and chain agglomerates are composed of spherical nodules of 5-50 nm in size.	69
Figure 5.3	Titanium content of a group of particles. a, TEM image. b, corresponding elemental map for titanium. X-rays characteristic of an element, in this case titanium, are emitted upon electron excitation as the microscope's electron beam rasters the sample. The elemental map indicates the relative count rate of characteristic x-rays released at each point on the sample. Lithium cannot be detected with EDX due to its low-energy x-rays that cannot pass through the detector's protective beryllium window. Therefore, the nanomaterial produced in this facility was identified by the presence of titanium, which was only found in the spherical agglomerates.	70
Figure 5.4	Chemical composition of a chain agglomerate particle. a, TEM image. b-g, corresponding elemental maps for several elements show that the chain agglomerates do not contain titanium but do contain elements common to welding fume (e.g. Mn).	71
Figure 5.5	Sample results from real-time, activity-based monitoring. Worker production activities are identified with arrows and labeled at the top of the figure. a, very fine particle number concentrations were not related to worker activities indicating the presence of other sources of small particles within the facility. b, respirable and total mass concentrations were strongly related to changing a nanomaterial collection bag and filling the hopper.	72
Figure 6.1	SEM images of NaY: (A) nanocrystalline NaY (scale bar = 400 nm) and (B) Aldrich NaY (scale bar = 5 μ m).	83
Figure 6.2	XRD patterns of synthesized nanocrystalline NaY and CuY and Aldrich NaY.	85

Figure 6.3	EPR spectrum of nanocrystalline CuY recorded at 77 K.	86
Figure 6.4	FTIR spectra of NO ₂ adsorbed on Aldrich NaY, nanocrystalline NaY and nanocrystalline CuY at T = 298 K. A pressure of 1.5 Torr NO ₂ was allowed to equilibrate, and the gas phase was pumped out prior to collecting each spectrum. The blank grid was used as a reference, and the corresponding clean zeolite spectrum prior to NO ₂ adsorption has been subtracted.	87
Figure 6.5	FTIR spectra of NH ₃ adsorbed on Aldrich NaY, nanocrystalline NaY and nanocrystalline CuY at T = 298 K. The gas phase was pumped out prior to collecting each spectrum. The blank grid was used as a reference, and the corresponding clean zeolite spectrum prior to NH ₃ adsorption has been subtracted.	91
Figure 6.6	FTIR spectra of gas phase species detected (A) pre-SCR and post-SCR over nanocrystalline CuY at T = 298 K, and (B) at 30 second intervals for the first 30 minutes during SCR over nanocrystalline CuY at T = 298 K. The blank grid was used as a reference.	94
Figure 6.7	Concentrations of gas phase NO (upper) and N ₂ O (lower) over Aldrich NaY, nanocrystalline NaY and nanocrystalline CuY during NH ₃ -SCR of NO ₂ at T = 298 K.	95
Figure 6.8	FTIR spectra of surface species detected post-SCR over Aldrich NaY, nanocrystalline NaY and nanocrystalline CuY at T = 298 K. The gas phase was pumped out prior to collecting each spectrum, and the blank grid was used as a reference. Corresponding clean zeolite spectra prior to SCR have been subtracted.	97
Figure 6.9	Concentration of gas phase NO ₂ over Aldrich NaY, nanocrystalline NaY and nanocrystalline CuY during NH ₃ -SCR of NO ₂ at T = 298 K.	99
Figure 7.1	Powder x-ray diffraction patterns for silver nanoparticles with XRD patterns shown for several reference compounds.	114
Figure 7.2	X-ray photoelectron spectra for silver nanoparticles (a), silver foil (b), and ion sputtered silver foil (c), showing the Ag 3d region (upper), the O 1s region (middle), and the C 1s region (lower). A peak-fit was applied to each region. The black solid line represents experimental data and the green line represents the total calculated fit. The blue, red, orange, and purple curves represent components used to curve fit the spectra.	115
Figure 7.3	Transmission electron microscopy image of silver nanoparticles substrate-deposited from a water suspension (a) with the corresponding particle size distribution (b).	116

Figure 7.4	SMPS particle size distribution for silver nanoparticles aerosolized from a water suspension (a), and normalized SMPS particle size distributions for silver nanoparticles aerosolized from aqueous nitric acid suspensions at a range of pH values (b).	118
Figure 7.5	TEM images (left) and corresponding particle size distributions (right) for silver nanoparticles substrate-deposited from aqueous nitric acid suspensions at pH 3 (upper) and pH 1 (lower).	119
Figure 7.6	Digital photograph of silver nanoparticle suspensions in water and aqueous nitric acid solutions at various pHs (a) and bulk silver in aqueous nitric acid at pH = 0.5 (b).	121
Figure 7.7	Plot of zeta potential measurements as a function of pH for silver nanoparticles suspended in water and acidified with nitric acid solutions.	124
Figure 7.8	ICP results for percent dissolved silver for nanosilver and microsilver particles in aqueous nitric acid solutions.	124
Figure 7.9	Summary of the behavior trend for commercially manufactured silver nanoparticles in aqueous acidic environments. The state of the nanoparticles (top) shows agglomeration at neutral pH, trending to deagglomeration, isolated particles, and silver ions at low pH. The color of the suspension trends from black (neutral) to gray to yellow to a colorless solution at low pH. The electric potential of the suspended particles trends from stable (neutral) to unstable, and becomes more stable after the isoelectric point minimum. The percent dissolved silver (bottom) is small but detectable at neutral pH and increases rapidly at $\text{pH} \leq 0.5$.	128
Figure 8.1.	PSDs with time during CuNPs dissolution in 0.5 M HCl. Time (minutes) is shown in each PSD plot. It should be noted the data are presented in terms of size bins and reported as $dN/d\log D_p$ versus $\log D_p$, where N is the number concentration of particles and D_p is the particle diameter.	135
Figure 8.2	ES-SMPS PSD data for CuNPs in 0.5 M HCl after 30 minutes (black) and 1 wt % Cu ion standard solution (blue).	136
Figure 8.3	Percent copper dissolved with time based on ICP/OES analysis (black) and ES-SMPS data (red). Water and water with CuNPs removed are shown to confirm no CuNPs were detected as ions.	137
Figure 9.1	ES-SMPS particle size distributions for copper nanoparticles in 0 M HCl (initial), 0.025 M HCl, 0.05 M HCl, and 0.1 M HCl. The inset compares the initial (0 M HCl) and final (0.1 M HCl) PSDs.	144

Figure 9.2	Particle volume versus reaction time for copper nanoparticles reacted in 0.1 M HCl. Volumes are based on the diameter of the peak maximum of the PSDs with time.	145
Figure 9.3	Sample color for copper nanoparticles in HCl during ES-SMPS analysis. Initial, 0.025 M, and 0.1 M samples are suspensions of particles in HCl, and 0.5 M sample with copper ions dissolved in HCl is shown for comparison.	145
Figure 9.4	Sample color for powders collected after reaction of nanoscale and microscale copper particles with HCl solutions.	146
Figure 9.5	TEM images of the initial copper nanoparticles (a) and 0.1 M HCl reacted particles showing isolated nanoparticles (b) and rectangular nanostructured aggregates (c).	148
Figure 9.6	Powder XRD of initial nanoscale and microscale copper samples. Copper metal and copper oxides are shown for reference.	149
Figure 9.7	Powder XRD for nanoscale copper (upper) and microscale copper (lower) after reaction with HCl solutions. Copper metal, copper oxides, and the copper chloride hydroxide mineral paratacamite are shown for reference.	150
Figure 9.8	Possible mechanism of paratacamite formation in aqueous HCl solution on the copper-based nanoparticle surface.	152

LIST OF ABBREVIATIONS

BET	Brauner Emmett Teller
CNT	Carbon Nanotube
DL	Double Layer
DLS	Dynamic Light Scattering
EDX	Energy Dispersive X-ray Spectroscopy
EFAL	Extra Framework Alumina
ES-SMPS	Electrospray Scanning Mobility Particle Sizer
FTIR	Fourier Transmission Infrared
ICP/AES	Inductively Coupled Plasma/Atomic Emission Spectroscopy
ICP/OES	Inductively Coupled Plasma/Optical Emission Spectroscopy
LOD	Limit of Detection
MCE	Mixed Cellulose Ester
MWCNT	Multi-Walled Carbon Nanotube
pI	Isoelectric Point
PSD	Particle Size Distribution
RBM	Radial Breathing Mode
SCR	Selective Catalytic Reduction
SEM	Scanning Electron Microscopy
SERS	Surface Enhanced Raman Spectroscopy
SSA	Specific Surface Area
SWCNT	Single Walled Carbon Nanotube
TEM	Transmission Electron Microscopy
XPS	X-ray Photoelectron Spectroscopy
XRD	X-ray Diffraction

CHAPTER 1

INTRODUCTION

1.1 Nanomaterial Properties

Nanomaterials are defined as materials with primary particles less than 100 nm in length in at least one dimension. The primary particles, nanoparticles, may be spheres, rods or tubes, whiskers, or have any variety of irregular shape. Nanoparticles can form stable agglomerates or aggregates that are larger in size. The ASTM International has differentiated between agglomerates and aggregates by defining agglomerates as a group of particles held together by relatively weak forces that may break apart into smaller particles upon processing. Aggregates are defined as a group of particles held together by strong forces or bonds and are not easily broken apart¹. Nanomaterials can have size dependent properties that result in unique behavior relative to materials composed of larger particles. Nanomaterials can retain such size dependent properties even when the primary particles form agglomerates or aggregates. Therefore, scientific knowledge of materials composed of particles on larger size scales cannot be applied to nanomaterials and is not sufficient to predict the behavior of nanomaterials.

On the nanoscale, electronic, optical and magnetic properties can be size dependent. As particle size decreases, the surface/volume ratio of a material increases. Nanomaterials can have high surface/volume ratios, with a large percent of total atoms present as surface atoms. Therefore, thermodynamic stability is size dependent, with surface free energy becoming an increasingly significant contribution to the total free energy as particle size decreases, according to

$$\Delta G = \Delta G_{\text{surface}} + \square \Delta G_{\text{bulk}} \quad \text{Eq. 1.1.}$$

Thus, the primary particle size of a material can influence surface properties, including surface area, arrangement of surface atoms, surface electronic structure, surface composition and functionality, as well as bulk properties, including shape, size, phase, electronic structure and crystallinity. Size dependent properties may become more pronounced as primary particle size decreases, with the most significant effects seen for the smallest particles², less than 10 nm.

1.2 Nanomaterial Applications

The unique properties of nanomaterials have attracted much attention for scientific discovery and technological applications. The ability to engineer materials with specific properties on the nanometer scale continues to progress, with new capabilities to synthesize highly uniform nanoscale materials, and the advent of new instrumentation to interrogate nanomaterials. These advancements have led to a host of nanomaterials available for energy and environmental applications, and for improving human health through biosensing, drug delivery, etc. Nanomaterials are found in electronic, cosmetic, automotive, food and beverage, medical, and a variety of additional consumer products. The Project On Emerging Nanotechnologies estimates an inventory of more than 1,000 manufacturer-identified nanotechnology-based consumer products available on the market³. Data collected over the last five years show a linear growth in the number of nano-based consumer products, with the largest surge in the health and fitness category. The most commonly manufactured nanomaterials are shown in Figure 1.1⁴. Although silver is a close second to carbon based on material production, the number of nano-based consumer products containing silver is the highest, outranking those containing carbon by more than a factor of three.

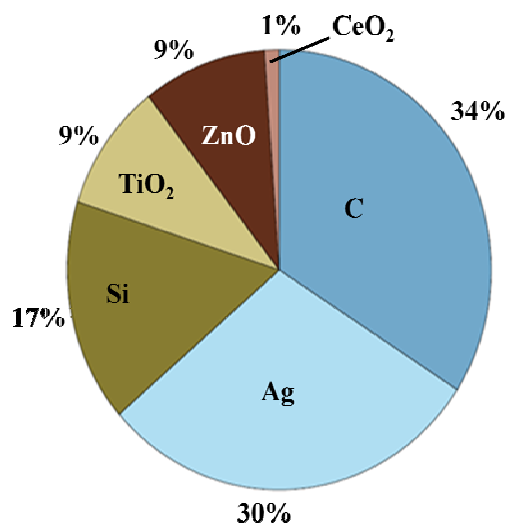


Figure 1.1 Commonly manufactured nanomaterials by percentage. (Maynard, A. D. *Nanotechnology: A research strategy for addressing risk*; Woodrow Wilson International Center for Scholars: 2006.)

1.3 Environmental and Health Considerations of Nanomaterials

As the production of engineered nanomaterials continues to increase, an understanding of the impact these materials will have on the environment and human health remains a pressing concern. It can be expected that nanomaterials will become present in the environment, including air, water and soil, at some point during their life cycle of production, distribution, usage or disposal. Additionally, nanomaterials are being developed for health applications and may enter the human body through inhalation, ingestion, or skin contact. This has led to questions about how well we understand the environmental health and safety risks of nanomaterials. Can material safety data sheets developed for bulk materials be used for nanomaterials? What necessary measures are needed to ensure the implications of nanomaterials are well

understood as these materials are developed and applied in a wide-range of applications? Furthermore, what can be done to reduce the uncertainties in our understanding of the environmental health and safety implications of nanotechnology? A high level of scientific understanding is essential so that sound policies can be developed and implemented with certainty while nanoscience and nanotechnology continue to grow.

It is clear from the literature that the full impact of manufactured nanomaterials on human health and the environment has yet to be fully understood⁵⁻⁷. Since nanomaterials are of varying chemical complexity (bulk and surface) with properties that can fluctuate based on particle size, a thorough characterization of bulk and surface properties is necessary. Bulk characterization methods examine the shape, size, phase, electronic structure and crystallinity, and surface characterization methods include surface area, arrangement of surface atoms, surface electronic structure, surface composition and functionality.

As nanomaterials are transported through the environment or the human body, they may undergo transformations that could influence their properties. The transport and transformation of nanomaterials as they interact, react, and breakdown in the natural environment and biological systems will determine their fate and toxicity. Studies of the environmental fate and transport of nanomaterials, as well as human health and safety, need to be correlated to nanomaterial characterization to understand how nanomaterials may behave in the environment and the cause of any toxicity or hazards attributed to nanomaterials. Therefore, nanomaterial properties must be studied in a variety of environmentally and biologically relevant conditions to consider how they may be transformed and transported in specific environments. This requires an assessment of the

physical and chemical properties of nanoparticles in each state, as aerosols, dissolved ions, or liquid suspensions. For example in aqueous environments, nanoparticles may undergo greater aggregation, or in some cases deaggregation, dissolution, precipitation or sedimentation. These processes will depend on the type of nanomaterial and its properties, as well as conditions such as aqueous phase composition (e.g. ionic strength, pH, and the presence of organic matter) and temperature. Water solubility is an important factor affecting the fate and transport of nanomaterials in the environment and their bioavailability in the human body. Many nanomaterials are coated to suppress or enhance their solubility and bioavailability in specific surroundings. However, these coatings may also affect the way the particles interact with the natural environment or biological systems upon exposure to water or air.

Manufactured nanoparticles can become a component of indoor and outdoor environments and thus the air we breathe. An abundance of SiO_2 nanoparticles around 10 nm in size were detected with a single particle mass spectrometry in Houston, Texas⁸. Although the exact source of these SiO_2 nanoparticles was unclear, it appeared to be from manufactured or industrial processes. Since nanoparticles and their agglomerates are likely to be in the respirable size range, it is important to investigate the potential health effects of these particles suspended in air as aerosols^{7, 9, 10}.

Nanoparticle exposure to biological systems can occur through skin contact, ingestion, and inhalation. Many skincare products contain nano-based TiO_2 or ZnO , and quantum dots and metal nanoparticles are being developed for drug delivery applications, ensuring dermal and ingestion exposure routes. Oxidation-reduction (redox) reactions are known to cause environmentally and biologically relevant transformations for certain

nanomaterials. Titanium dioxide (TiO_2), for example, can oxidize organic compounds in the environment and inactivate microorganisms^{11,12}. This oxidative property of TiO_2 has led to applications such as skin care and water treatment, where antimicrobial properties are desirable, but it may be detrimental to microorganisms that are beneficial to the natural environment. Additionally, solar radiation can cause photochemical reactions or photoactivated reactive species. It can also contribute to the degradation of nanoparticles or their surface coatings. Many nanoparticles are designed with surface coatings or surface functionalization to enhance dispersion or biocompatibility¹³. The bioactive coatings of quantum dots can be photosensitive, degrading to expose the metal core to the surroundings^{14,15}. Once nanoparticles are absorbed in a biological system they may be able to translocate. Surface modifications can change the size of the particles and affect their ability to translocate in the human body^{16,17}, and for nanoparticles < 10 nm, surface modification may result in a significant size increase relative to the particle diameter. Studies have shown that TiO_2 inhaled into the lungs can be distributed to other organs¹⁸, and some nanoparticles are even able to cross the blood-brain barrier^{19,20}. The distribution of nanoparticles will depend on their properties, such as size, shape and chemical composition.

As noted in Figure 1.1, carbon based nanomaterials are the most commonly manufactured, with silver a close second, and a variety of metal oxides comprise the remaining one third. For this reason, many environmental and human health studies have focused on carbon based nanomaterials²¹⁻²³ and metal oxides^{24,25}. Commercial applications of carbon nanotubes (CNTs) are rapidly expanding (gene therapy agents²⁶, drug delivery agents²⁷, and sorbents for wastewater treatment²⁸), but their potential

effects on the environment and human health are not well understood^{6, 29, 30}. Carbon nanotubes are sheets of graphite rolled into hollow tubes with lengths ranging from 1-100 μm and diameters from 1-25 nm ³¹. Single walled carbon nanotubes (SWCNTs) consist of one graphite tube, while multi-walled carbon nanotubes (MWCNTs) may consist of two or more concentric graphite tubes. The surface of CNTs can be functionalized with oxides to promote dispersion³²⁻³⁴, but surface oxidation can also occur in the natural environment. The extent of surface oxidation, type and relative ratio of surface oxide functional groups on CNTs can dictate the sorption properties of CNTs and whether the CNT aggregates form stable suspensions or settle out of solution³⁵.

The fibrous shape of CNTs has led to concerns that they may show pathogenic behavior similar to asbestos. A recent study examined the potential of MWCNTs to show asbestos-like toxicity in the abdominal cavity of mice²³. A size-dependent granuloma response was observed, with long fibers ($> 20 \mu\text{m}$) showing significant granulomas and shorter fibers showing no significant granulomas, suggesting that CNTs of sufficient fiber length may have the potential to produce a toxic response similar to asbestos. This study compared four CNT samples from three different sources, therefore, physical and chemical properties, as well as type and percentage of metal contaminants, were not the same for each sample. The percentage of long fibers was not determined for the short fiber samples. Six metal contaminants were identified in varying amounts in the four samples. An earlier study aimed at evaluating the pulmonary toxicity of carbon nanotubes was inconclusive because toxic effects resulting from CNT inhalation could not be distinguished from known toxic effects of the nickel metal contaminant in the carbon nanotube sample²².

Commercial oxide nanoparticles (titanium dioxide, zinc oxide, iron oxide) are used in paints and sunscreens for their pigmentation and antibacterial properties. Oxide nanoparticles purchased commercially as powders or liquid suspensions contain aggregates of the primary nanoparticles, formed during the manufacturing process. While the primary particles may be ~5-25 nm in diameter, aggregates greater than 100 nm tend to dominate aqueous suspension even after extensive sonication^{36,37}. Oxide nanoparticles can be manufactured with surface functional groups to allow dispersion of the primary particles, thus, oxide nanoparticles may exist in aquatic environments as primary particles or aggregates of larger sizes.

Studies of the size-dependent inflammatory response resulting from instillation or inhalation of nanomaterial and bulk metal oxides have shown inflammation correlated with the surface area of the nanomaterials³⁸. However, this study compared one nanoscale TiO₂ sample with one microscale TiO₂ sample. Recently, an investigation of inflammatory response in mice compared 5 nm and 21 nm TiO₂, and showed that inflammation did not correlate to the surface area for the two nano-TiO₂ sizes, but is instead a nano-effect possibly related to the greater agglomeration of smaller particles²⁴. Other studies have shown that the crystalline phase³⁹ and particle shape⁴⁰ of TiO₂ nanoparticles affect toxicity and the results do not correlate with surface area alone.

The characterization and toxicity studies in the current literature demonstrate the surface chemistry, specific surface area (SSA), morphology, crystallinity, and contamination of nanomaterials can influence their properties, and the inability to attain a thorough characterization, or relate toxic results to the properties of nanomaterials, has been a limitation in accurately interpreting results of health and safety studies.

Additionally, widespread variation in the properties of manufactured nanomaterials (variation from manufacturer's specifications and variation from batch to batch) is becoming apparent, further demonstrating the need for characterization to accompany environmental, health and safety studies for each batch of every nanomaterial studied.

1.4 Challenges and Needs for Addressing Nanotechnology Risks

There are current challenges in identifying or developing proper tools to evaluate the risks of nanomaterials, and the proper dose metric for measuring nanoparticle concentration. For instance, materials of larger particle size are measured on a mass basis, but nanomaterials typically have low mass concentration but a large particle number concentration⁴¹⁻⁴⁴. There is a recognized need to identify proper methods to measure nanoparticles in various media⁴⁵⁻⁴⁸. Accurate nanomaterial measurements can be challenging to acquire, and especially challenging to monitor over time due to the nanomaterial properties outlined in Figure 1.2⁴⁶. Instrumentation and methods capable of overcoming or accounting for the unique challenges of studying nanomaterials are necessary. Different methods can be coupled to obtain a greater amount of information, and a variety of techniques can be used to verify results and provide a complete understanding of the physiochemical properties and their changes.

Another challenge is evaluating the effectiveness of current personal protective equipment and safety devices, such as respirators, filters and ventilation systems, to see if they are sufficient for protection from nanomaterial exposure. Thus, there is a need for an interdisciplinary approach to tackle the complex problem of understanding the environmental and health impacts of nanomaterials from every perspective: fundamental material studies, instrumentation development, environmental and health risk evaluation,

and implementation of standards and protocols. Characterization is necessary as a starting point so that results of subsequent investigations can be correlated to specific properties of any variety of nanomaterial. Only when all areas of nanomaterial interaction with the environment and human health are understood, and proper equipment is recognized for evaluating and protecting against nanomaterials, can there be an accurate risk assessment and recommendations for appropriate guidelines, safety standards and protocols regarding nanomaterials.

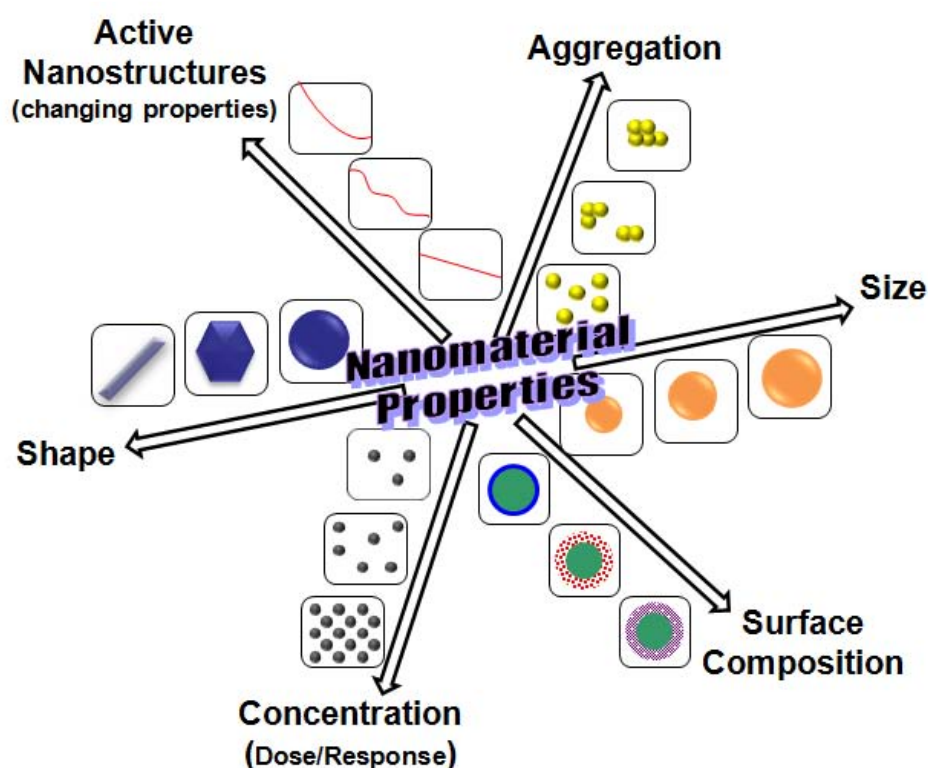


Figure 1.2. Nanomaterial properties that can affect characterization measurements. (Modified and adapted from Tinke, A. P.; Govoreanu, R.; Vanhoutte, K., Particle Size and Shape Characterization of Nano and Submicron Liquid Dispersions. *American Pharmaceutical Review* 2006, September/October.)

The research presented here addresses an environmental application of a novel nanomaterial, characterization of a variety of nanomaterials, and includes novel methods to study nanomaterials, with collaborative efforts that target an integrated approach for understanding nanomaterial environmental, safety and health effects. Specific objectives of each chapter of this thesis are stated in Chapter 2, and a brief introduction of the subsequent chapters is presented below.

1.5 Introduction to Thesis Chapters

Chapter 3 discusses the materials, experimental methods, and instrumental techniques used to conduct the research composing this thesis. Materials studied in this work include synthesized nanocrystalline zeolites and gold nanoparticles (silica-coated and sodium citrate stabilized), as well as commercially manufactured zeolite, single-walled carbon nanotubes (SWCNTs), multi-walled carbon nanotubes (MWCNTs), titanium dioxide nanoparticles, lithium titanate nanomaterial, polymer-coated silver nanoparticles, silver nanoparticles, and copper nanoparticles. These materials were studied with a combination of analytical techniques capable of determining bulk and surface properties, including shape, size, phase, electronic structure, crystallinity, specific surface area, arrangement of surface atoms, surface electronic structure, surface composition and functionality.

Bulk characterization techniques include scanning electron microscopy (SEM), transmission electron microscopy (TEM), energy dispersive X-ray photoelectron spectroscopy (EDX), electrospray-scanning mobility particle sizer (ES-SMPS), inductively coupled plasma optical emission spectroscopy (ICP/OES), and powder X-ray diffraction (XRD). Collectively, these techniques can characterize particle size

distributions, particle shape, morphology, aggregation, elemental composition, and crystallinity. Surface characterization techniques include Fourier transform infrared spectroscopy (FTIR), BET surface area analysis, X-ray photoelectron spectroscopy (XPS), and zeta potential. These techniques can characterize surface chemical composition, surface chemistry, and specific surface area. This suite of techniques is capable of characterizing nanomaterials in powder form, as aerosols, as a colloidal suspension, and as dissolved ions in solution.

Chapter 4 consists of characterization of commonly manufactured nanomaterials, including carbon nanotubes (CNTs), titanium dioxide nanoparticles, and silver nanoparticles, and synthesized gold nanoparticles. The CNTs were characterized in preparation for toxicology studies, and analyzed for specific surface area, diameter distributions, conductivity, and contamination of metal precursors or other carbonaceous material. Titanium dioxide nanoparticles were analyzed using the ES-SMPS to determine particle size distributions (PSDs) and aggregation as part of an investigation of nanoparticle aerosol generation methods. Polymer-coated silver nanoparticles were studied using the ES-SMPS coupled with TEM to measure coating thickness. Synthesized gold nanoparticles, bare and with silica shells, were studied using the ES-SMPS to determine coating thickness. Results also revealed information about particle-solution interactions.

Chapter 5 presents a collaborative study focused on measurements of nanomaterials in a manufacturing facility for occupational health and safety. Two methods were used to distinguish airborne engineered nanomaterials from incidental nanomaterials in a facility that produces lithium titanate metal oxide nanopowder. The first method involved off-

line analysis of filter samples collected within the facility. Throughout most of the facility and outdoors, respirable mass concentrations were attributed to particles other than the nanomaterial, as determined with ICP analysis. In a single area with extensive material handling, mass concentrations indicated the presence of airborne nanomaterial. Analysis of the filter samples collected in this area by TEM/EDX and SEM revealed the airborne nanomaterial particles were spherical aggregates larger than 200 nm in diameter. The second method, conducted by researchers with the Department of Occupational and Environmental Health at The University of Iowa, used two handheld, direct-reading instruments to obtain a time series of particle number for particles less than 300 nm, respirable mass, and total mass concentration. These data were related to activities within the area of extensive material handling. This activity-based monitoring showed particle number concentrations for particles less than 300 nm did not correlate with worker activities but that sharp peaks in the respirable and total mass concentration coincided with specific worker activities. These findings were consistent with the filter-based analysis, demonstrating airborne nanoparticles in this facility are dominated by incidental sources and airborne engineered product is predominately composed of particles larger than several hundred nanometers. The methods presented here are applicable to any occupational or environmental setting to distinguish incidental sources from engineered product.

In Chapter 6, an environmental application of novel nanocrystalline zeolites is investigated. The selective catalytic reduction (SCR) of NO_2 to N_2 and O_2 with ammonia at 298 K on nanocrystalline NaY, Aldrich NaY and nanocrystalline CuY was investigated using in situ FTIR spectroscopy. It was determined that the kinetics of SCR were 30%

faster on nanocrystalline NaY compared to commercial NaY. The superior performance of the nanocrystalline zeolite was attributed to an increase in external surface area and external surface reactivity. External surface sites, which include silanol groups and extra framework alumina, gave rise to differences in the adsorption of NO_2 and NH_3 on nanocrystalline NaY compared to commercial NaY. Copper-cation exchanged nanocrystalline Y resulted in an additional increase in the rate of SCR as well as distinct NO_2 and NH_3 adsorption sites associated with the copper cation. Nanocrystalline zeolites have potential as catalysts for enhanced NO_x emission reduction through NH_3 -SCR. The data presented from this work show nanocrystalline CuY resulted in increased reaction rates for NO_2 loss at a low temperature and achieved the highest NO reduction at increased temperatures. This is the first study of a transition metal cation-exchanged nanocrystalline zeolite and its potential use as a catalyst in the SCR of nitrogen oxides.

In Chapter 7, the dissolution of silver nanoparticles in acidic aqueous environments is presented. A complete characterization of the silver nanoparticles included XRD, XPS, BET analysis, TEM, ES-SMPS analysis, and zeta potential measurements. The ES-SMPS was used to investigate the state of manufactured silver nanoparticles in water and aqueous nitric acid environments. Over the range of pH values investigated, 0.5 to 6.5, silver nanoparticles with a bimodal primary particle size distribution show distinct size distributions indicating agglomeration between pH 6.5 and pH 3 and isolated nanoparticles at pH values from 2.5 to 1. At the lowest pH investigated, pH 0.5, there are no peaks detected by the SMPS, indicating complete nanoparticle dissolution. Further analysis of the solution with ICP/OES shows dissolved Ag ions at a pH of 0.5. Interestingly, silver nanoparticle dissolution shows size dependent behavior as larger,

micron-sized silver particles show no dissolution at this pH. Environmental implications of these results are discussed.

Chapter 8 presents real time data for particle size distributions of copper nanoparticles during dissolution in acid. In this study, the ES-SMPS is used to monitor the dissolution of copper nanoparticles in hydrochloric acid solutions in real-time. The PSD of copper nanoparticles with an average primary particle size of 15 nm was monitored in hydrochloric acid (HCl) solutions with molarities in the range of 0.01 – 0.5 M. Results with 0.5 M HCl show the peak maximum of the PSD is observed to decrease with time until no PSD is detected, indicating complete dissolution of the sample. Analysis with ICP/OES confirms dissolution of the copper nanoparticles. This work demonstrates the ES-SMPS system can be used to study dissolution of nanoparticles from the particle perspective, as a decrease in particle size. Experimental results are compared with simulated dissolution based on specific surface area. These data provide new insights into how the PSD changes from single modal to multimodal and show there are size dependent processes occurring that cannot be attributed to surface area and are not easily discerned when dissolution is measured as concentration of solution phase ions.

Chapter 9 presents interesting results seen for copper nanoparticles in lower concentrations of hydrochloric acid (0 – 0.1 M). With 0.025 M HCl, a pale green colloidal suspension was observed, and PSDs decreased and maintained a peak maximum of 8 nm. Further analysis with XRD revealed a chemical transition had occurred, from a copper metal to a copper chloride hydroxide mineral, paratacamite. Analogous experiments using micrometer copper showed no transition in chemical composition.

Conclusions and future directions for this research are discussed in Chapter 10. The advancement of nanotechnology-based consumer products is predicted to grow substantially, and it is clear there will be many issues that need to be addressed and questions that need to be answered concerning the potential impact this technology will have on the environment and human health. Characterization of nanomaterials will pave the way for research that seeks to address these issues and answer these questions. These studies are crucial to ensure nanotechnology can be beneficial to the environment and human health, and properly controlled to reduce hazardous exposure. The goals of the work presented here, and ongoing research of this nature, are broad and require an interdisciplinary approach composed of specific experiments that will combine to help shape the bigger picture. The work in this thesis contributes to an area of science that has a great need for further understanding through research.

CHAPTER 2

RESEARCH OBJECTIVES

The previous chapter introduced nanomaterials and their unique and size dependent properties. It also discussed the rapid advancement of nanotechnology, the questions and uncertainties nanotechnology have raised, and the challenges that remain as nanoscience and nanotechnology move forward. This research includes studies that address both an application of nanomaterials as well as the environmental and health concerns of nanomaterials, and uses new approaches to meet the challenges of studying the unique size-dependent chemistry of nanomaterials. As previously mentioned, the scope of this work is broad, but the overall goals are made up of specific sets of experiments with well defined objectives. The objectives of each of the following chapters are listed below.

- Chapter 4: Characterization of Nanomaterials.

Objective: I) Carbon Nanotube Characterization: Evaluate specific surface area, diameter distributions, conductivity, and contamination in preparation for toxicology inhalation experiments.

Objective II) Titanium Dioxide Nanoparticle Characterization: Use ES-SMPS analysis to determine particle size distributions as part of an investigation of nanoparticle aerosol generation methods.

Objective III) Silver Nanoparticle Characterization: Use the ES-SMPS coupled with TEM to measure polymer coating thickness.

Objective IV) Gold Nanoparticle Characterization: Use the ES-SMPS to determine coating thickness and changes in particle size due to particle-solution interactions.

- Chapter 5: Airborne Monitoring to Distinguish Engineered Nanomaterials from Incidental Particles for Environmental Health and Safety.

Objective: Use TEM/EDX and SEM to correlate chemical composition with particle size and shape for lithium titanate nanomaterial collected on filters at a manufacturing facility.

- Chapter 6: Selective Catalytic Reduction of NO_2 with Ammonia using Nanocrystalline NaY and CuY Zeolites.

Objective: Determine the activity and selectivity of nanocrystalline zeolites NaY and CuY for NH_3 -SCR (selective catalytic reduction) of NO_2 and compare the performance with commercial NaY.

- Chapter 7: Agglomeration, Isolation and Dissolution of Commercially Manufactured Silver Nanoparticles in Aqueous Environments.

Objective: Identify the state (aggregates, primary particles, or ions) of silver nanoparticles in aqueous nitric acid solutions as a function of pH.

- Chapter 8: Nanoparticle Dissolution from the Particle Perspective: Insights on Nanoscale Processes from Particle Sizing Measurements.

Objective: Use the ES-SMPS to monitor PSDs in real time to observe the decrease in mobility diameter as copper nanoparticles dissolve in hydrochloric acid.

- Chapter 9: Copper Nanoparticle Transition to Paratacamite Nanoparticles using Hydrochloric Acid

Objective: Use powder X-ray diffraction to identify the crystalline structure of

copper-based nanoparticles exposed to varying concentrations of hydrochloric acid and compare with copper microparticles.

CHAPTER 3

MATERIALS AND METHODS

3.1 Introduction

The materials considered in this research include nanomaterials synthesized by collaborators (Professor Larsen and Haes groups in the Department of Chemistry at The University of Iowa), as well as purchased commercial nanomaterials and micron-sized materials, and a nanomaterial collected on-site from the manufacturing facility. The experimental methods use state-of-the-art instrumentation and techniques capable of investigating particles on the nanoscale, particularly < 10 nm. Bulk techniques are used to examine the shape, size, phase, electronic structure and crystallinity, and surface techniques examine surface area, arrangement of surface atoms, surface electronic structure, surface composition and functionality.

3.2 Sources of Research Materials

3.2.1 Sources of Nanomaterials and Micromaterials The source of nanomaterials and micromaterials purchased from manufactures are listed in Table 3.1. The manufacturer's specifications, including material phase (powder or colloidal suspension), is given for each material. The source of the synthesized materials and specifications from characterization conducted prior to receiving the materials for this research are also listed in Table 3.1. All materials were used as is unless otherwise stated.

3.2.2 Sources of Reagents For experiments requiring aqueous solutions or dilutions, Optima water (Fisher Scientific) was used in all cases. The source of all other chemical reagents used in the research of the nanomaterials and micromaterials listed in Table 3.1 are shown in Table 3.2 with manufacturer's specified purity.

Table 3.1 Source of Nanomaterials and Micromaterials with Specifications Provided by the Manufacturer or Synthesis Research Laboratory

Nanomaterial	Source	Specifications
NaY zeolite Micromaterial	Purchased from Aldrich, Milwaukee, WI	Powder: 1000 nm particle diameter Total SSA: 442 m ² /g
NaY zeolite Nanomaterial	Synthesized, research lab of Dr. Sarah Larsen, Department of Chemistry, The University of Iowa	Powder: 38 nm particle diameter Total/External SSA: 523/106 m ² /g Si/Al ratio: 1.8
CuY zeolite Nanomaterial	Synthesized, research lab of Dr. Sarah Larsen, Department of Chemistry, The University of Iowa	Powder: 34 nm particle diameter Total/External SSA: 538/118 m ² /g Si/Al ratio: 1.8 Cu/Al ratio: 0.3
Single Walled Carbon Nanotubes	Purchased from Nanostructured & Amorphous Materials, Inc., Houston, TX	Powder: 90% CNT, 80% SWCNTs Outside diameter: 1-2 nm Length: ~15 μm SSA: > 400 m ² /g
Multi-Walled Carbon Nanotubes	Purchased from Nanostructured & Amorphous Materials, Inc., Houston, TX	Powder: 90% CNT, 50% DWCNT Outside diameter: < 5 nm Inside diameter: 1.3-2.0 nm Length: 5-15 μm SSA: > 400 m ² /g
Silver Nanoparticles (polymer-coated)	Purchased from Vive Nano, Toronto, Canada	Colloidal suspension in water, <1 wt % Ag 2-5 nm core diameter 2-3 nm polymer shell
Titanium Dioxide Nanoparticles	Purchased from Nanostructured & Amorphous Materials, Inc., Houston TX	Powder: 5 nm particle diameter SSA: ~ 250 m ² /g
Lithium Titanate Metal Oxide Nanomaterial	Collected from Altair Nanotechnologies, Reno, Nevada	Powder, collected from aerosol phase on filters, details of the material are proprietary
Silver Nanoparticles	Purchased from Nanostructured & Amorphous Materials, Inc., Houston TX	Powder: Ag with 0.3 % PolyVinyPyrrolidone surfactant 5-15 nm particle diameter SSA: 9-11 m ² /g
Silver Microparticles	Purchased from Aldrich, Milwaukee, WI	Powder: ~ 10 micron diameter flakes 99.9% Ag metals basis

Table 3.1 Continued

Gold Nanoparticles (citrate surface layer)	Synthesized, research lab of Dr. Amanda Haes, Department of Chemistry, The University of Iowa	Colloidal suspension in water, 25 nM 13.3 ± 0.6 nm particle diameter
Copper Nanoparticles	Purchased from Nanostructured & Amorphous Materials, Inc., Houston TX	Powder: Cu with 10% oxygen 25 nm particle diameter SSA: 30-50 m ² /g
Copper Microparticles	Purchased from Alfa Aesar, Ward Hill, MA	Powder: 10 µm diameter spheres 99.9% Cu metals basis

Table 3.2 Source of Reagents

Reagent	Source	Purity
Methanol	Fisher Scientific, Fair Lawn, NJ	99.9%, HPLC Grade
Ammonia	Matheson Tri-Gas, Montgomeryville, PA	Anhydrous, 99.99%
Nitrogen Dioxide	Matheson Tri-Gas, Montgomeryville, PA	99.5%
Nitric Acid	Fisher Scientific, Fair Lawn, NJ	15.8 Normal
Hydrochloric Acid	Fisher Scientific, Fair Lawn, NJ	12.1 Normal
Silver Atomic Spectroscopy Standard	PerkinElmer, Shelton, CT	Silver, 2% HNO ₃ 1000 µg/mL
Copper Atomic Spectroscopy Standard	PerkinElmer, Shelton, CT	Copper, 2% HNO ₃ 1000 µg/mL
Copper Inductively Coupled Plasma Standard	Elements, Shasta Lake, CA	Copper, 5% HNO ₃ 10,000 µg/mL
Nitrogen	Airgas, Inc., Radnor, PA	99.999%, Research Grade
Carbon Dioxide	Airgas, Inc., Radnor, PA	99.999%, Research Grade

3.3 Characterization Techniques

3.3.1 Bulk Characterization Techniques Bulk techniques used to examine the shape, size, phase, electronic structure and crystallinity of the materials studied are listed in Table 3.3. The instrument specifications, phase of the material during analysis, and the information obtained for each technique are given.

Table 3.3 Instrumentation for Bulk Characterization

Technique / Instrument	Nanomaterial Phase	Information
ES-SMPS (Electrospray-scanning mobility particle sizer) TSI, Inc. models 3480, 3080, 3085, and 3776.	Aerosol	Particle size distributions
TEM/EDX (transmission electron microscopy and energy dispersive x-ray capability) JEOL JEM-1230 JEOL JEM-2100F Hitachi H-7000	Bulk Powder	Particle size distributions, particle shape, morphology, aggregation, and elemental analysis
SEM (scanning electron microscopy) Hitachi S-4800	Bulk Powder	Particle size distributions, particle shape, morphology, and aggregation
Powder XRD (X-ray diffraction) Siemens D5000 X-ray diffractometer	Powder	Crystallinity
ICP (inductively coupled plasma) Varian ICP-OES 720-ES	Solution	Elemental composition
Raman Spectroscopy	Powder	Molecular structure

3.3.2 Surface Characterization Techniques Surface techniques used to examine surface area, arrangement of surface atoms, surface electronic structure, surface composition and functionality of the materials studied are listed in Table 3.4. The instrument specifications, phase of the material during analysis, and the information obtained for each technique are given.

Table 3.4 Instrumentation for Surface Characterization

Technique / Instrument	Nanomaterial Phase	Information
XPS (X-ray photoelectron spectroscopy) Kratos Axis Ultra system	Powder	Surface elemental composition and surface chemistry
Transmission FTIR (Fourier transform infrared) Spectroscopy Mattson, model GL-6021	Powder (thin film)	Surface chemistry
BET Surface Area Instrument Quantachrome Nova 4200e	Powder	Specific surface area
Zeta Potential Zetasizer Nano ZS, Malvern Instruments	Suspension	Surface charge

3.4 Sample Preparation for Characterization and Experiments

3.4.1 SEM and TEM/EDX Microscopy Microscopy analysis, including SEM and TEM, was used as a characterization technique throughout the research presented in this

thesis. Both techniques provide information on particle size, particle shape, morphology, and can provide insight into particle aggregation. Sample preparation for SEM analysis included sonicating a dilute suspension of the nanomaterial in water or methanol for 20-30 minutes and dropping a portion onto an aluminum SEM stub with a pipette. Once the droplet was dry, SEM analysis was performed. For TEM analysis, samples were prepared in the same way but were dropped onto a TEM grid and allowed to air dry. TEM grids were purchased from Ted Pella, Inc. (Redding, CA) as Carbon-B 300 Mesh Copper Grids. For the study presented in Chapter 6, TEM was coupled with EDX to provide chemical composition data for individual particles. The unique sample preparation and EDX analysis for that study is discussed in Section 3.4.5. Sample deposition onto TEM grids using the ES-SMPS coupled to TEM are discussed in Section 3.4.10.

3.4.2 BET Specific Surface Area Analysis BET (Brauner-Emmett-Teller) specific surface area analysis used physical adsorption of nitrogen gas molecules onto the material surface to calculate surface area. For each material studied, a sample was weighed and placed in a sample cell that was volume calibrated. The sample was heated to the highest acceptable temperature for the particular material and degassed overnight. Nitrogen adsorption isotherms were collected using the seven-point N₂-BET method to calculate the SSA. For the nanocrystalline zeolite samples, BET analysis was carried out before and after calcination to remove the template in order to measure both external and total SSA.

3.4.3 Transmission FTIR Spectroscopy The investigation of zeolite materials in Chapter 6 used transmission FTIR spectroscopy to study surface chemistry and gas phase

species during surface-catalyzed reactions. Zeolite samples (10-15 mg) were sonicated in methanol for 30 minutes at room temperature. For the nanocrystalline samples, the powder was crushed with a mortar and pestle to break up agglomerates prior to sonication. The suspension was transferred by pipette to one half of a tungsten grid, and the methanol evaporated at room temperature to create a uniform thin film. A thermocouple wire was attached to the tungsten grid to allow resistive heating. The sample holder was placed in a stainless steel reaction chamber equipped with a linear translator to allow either the gas phase or the zeolite sample to be placed in the path of the FTIR beam. The reaction chamber was connected to a power supply and vacuum/gas handling system. A diagram of the FTIR experimental system is shown in Figure 3.1.

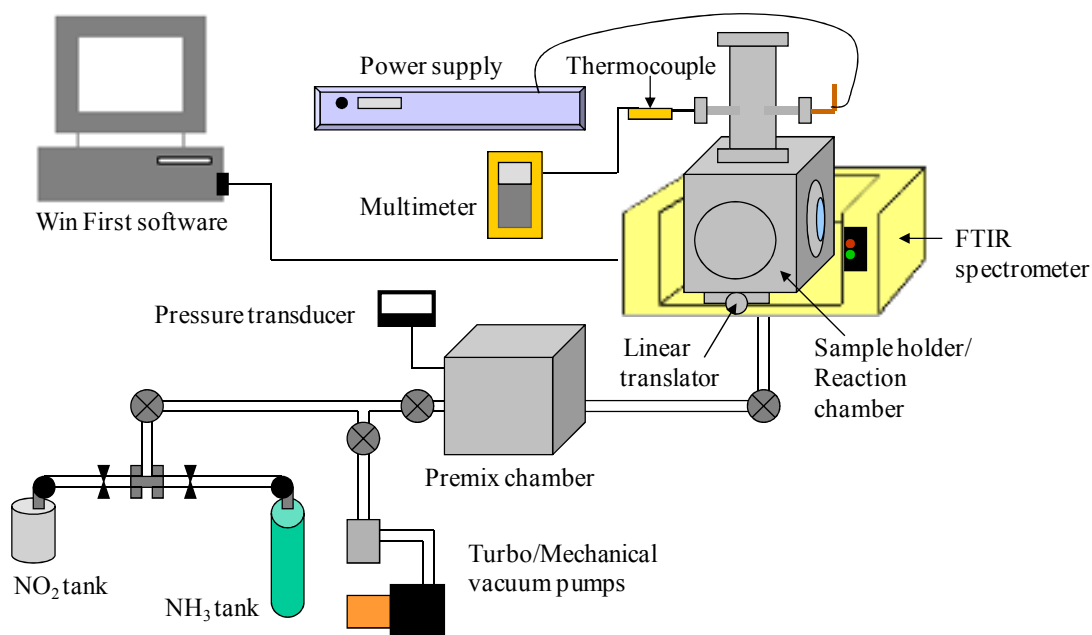


Figure 3.1 Transmission FTIR experimental system.

WinFirst software was used to acquire the data, and spectra were recorded using 64 averaged scans with a resolution of 4 cm^{-1} . Gas-phase spectra were referenced to the blank grid, and absorbance spectra were referenced to the corresponding gas phase background with the clean zeolite subtracted. Zeolite samples were heated overnight at 600 K under vacuum prior to experiments, and the sample was allowed to cool to room temperature before gases were admitted into the reaction chamber.

3.4.4 Raman Spectroscopy for Carbon Nanotube Characterization

Raman spectroscopy is a technique that uses the inelastic scattering of monochromatic light to gain information about chemical bonds. Carbon nanotubes were characterized by Raman spectroscopy to approximate tube diameter, identify characteristic graphite peaks, classify conductivity, and estimate carbonaceous contamination. The Raman analysis was performed using a Mark II holographic fiber-coupled stretch probehead attached to the HoloLab5000R modular research Raman spectrograph (Kaiser Optical Systems, Inc., Ann Arbor, MI, USA) with optical microscope (DMLP, Leica Microsystems GmbH, Wetzlar, DEU). Samples were analyzed as dry powders on a glass slide and exposed to a 8 mW laser (785 nm wavelength) for 30 seconds with two accumulations.

3.4.5 Off-line Filter Analysis of Lithium Titanate Metal Oxide Nanomaterial

Researchers from the Department of Occupational and Environmental Health at The University of Iowa collected samples of lithium titanate metal oxide nanomaterial on mixed cellulose ester (MCE) filters (SKC, Inc., Eighty Four, PA) from the manufacturing facility, Altair Nanotechnologies (Reno, NV).

The samples were analyzed using TEM/EDX and SEM analysis to characterize particle size, shape, aggregation, and chemical composition. The samples were deposited

onto a TEM grid from the MCE filter following an established method, Burdett and Rood⁴⁹. Square sections of the MCE filters were placed sample side up on TEM grids, and the filters were collapsed with a mixture of 50% deionized water, 35% dimethylformamide, and 15% glacial acetic acid, etched using a plasma asher to remove organic material, and coated with a carbon layer for conductivity. The TEM grids were placed in a Jaffe washer filled with dimethylformamide for two hours to completely dissolve any remaining filter residue. The grids were placed in the TEM instrument equipped with EDX capability for analysis.

During EDX analysis, x-rays characteristic of an element are emitted upon electron excitation as the microscope's electron beam rasters the sample. An elemental map is generated and indicates the relative count rate of characteristic x-rays released at each point on the sample. Lithium cannot be detected with EDX due to its low-energy x-rays that cannot pass through the detector's protective beryllium window. Therefore, the lithium titanate nanomaterial produced in this facility was identified by the presence of titanium.

3.4.6 X-ray Photoelectron Spectroscopy XPS uses x-rays to eject core electrons from a sample, and an electron from a higher energy level relaxes to a lower energy state, releasing a photoelectron with characteristic binding energy. The surface of silver nanoparticles was analyzed using XPS to gain information about the surface chemical composition and oxidation states. The silver nanopowder sample was pressed onto indium foil and mounted onto a copper stub. The copper stub with the sample was introduced into the surface analysis chamber, maintained at a pressure in the 10^{-9} Torr

range during analysis. Silver foil and ion sputtered silver foil were analyzed with XPS for comparison.

3.4.7 Powder X-ray Diffraction Bulk crystallinity was determined using powder XRD analysis. Dry powder samples were placed in the XRD sample holder, and the surface of the powder was smoothed with a razor until flush with the rim of the holder. A Siemens D5000 X-ray diffractometer with Cu K α target and nickel filter was used to collect the XRD powder patterns between angles of 2θ from 10° and 90°.

3.4.8 Zeta Potential A Zetasizer Nano ZS was used for DLS and zeta potential measurements of silver nanoparticles. Particle size distributions of colloidal suspensions can be determined using DLS. This technique uses scattered light to measure diffusion rates (Brownian motion) of particles in stable suspensions to determine a hydrodynamic diameter for particles and aggregates.

Zeta potential, ξ , is based on the mobility of a particle in an electric field and is related to the electrical potential at the junction between the diffuse ion layer surrounding the particle surface and the bulk solution. A stable suspension requires dominant repulsive forces between particles to maintain dispersion. If the attractive forces dominate, or particles collide with sufficient energy to overcome repulsion, they will begin to floc and eventually form agglomerates that sediment.

For both analyses, silver nanoparticles were suspended in water and aqueous nitric acid solutions at pH values between 0.5-3.5 and studied at a concentration of 1 mg/ml. The zeta potential determinations were based on electrophoretic mobility of the nanoparticles in the aqueous medium, which were performed using folded capillary cells in automatic mode.

3.4.9 Inductively Coupled Plasma/Optical Emission Spectroscopy Elemental composition can be calculated using ICP/OES analysis for ions in solution. The concentration of silver ions and copper ions in solution after nanoparticle exposure to acidic solutions was quantified for dissolution studies. The nanoparticle suspensions were filtered with 0.2 μm Xpertek filters and centrifuged at 14,000 rpm for 30 minutes to separate nanoparticles from the solution. Five standard solutions with known silver or copper concentrations were prepared as calibration standards. Exact concentrations of silver or copper in the sample solutions were obtained by projection from the working calibration curve generated from standard solution data.

3.4.10 Electro spray-Scanning Mobility Particle Sizer An electro spray atomizer coupled to a scanning mobility particle sizer (ES-SMPS) is used to characterize PSDs and investigate the state of nanoparticles in acidic conditions. A schematic of this system is shown in Figure 3.2.

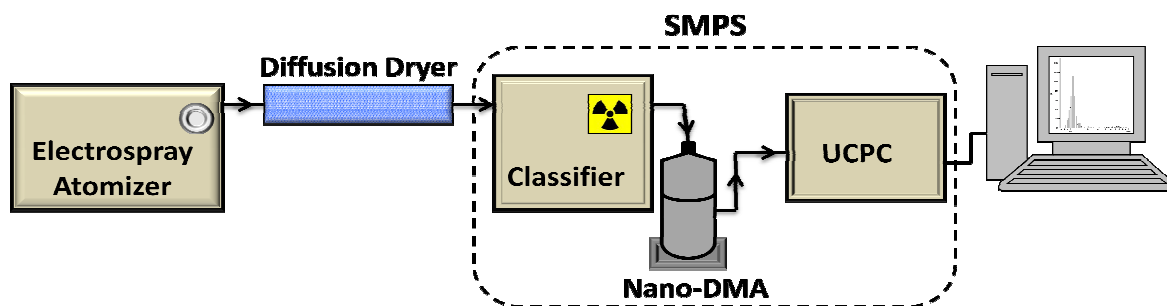


Figure 3.2 Schematic of an electro spray aerosol generator coupled to a scanning mobility particle sizer.

All components of the ES-SMPS system were purchased from TSI, Inc., including the electro spray (model 3480), electro spray capillaries (part no. 3900124), diffusion dryer (model 3062), classifier (model 3080), nano differential mobility analyzer (DMA) (model 3085), and ultrafine condensation particle counter (UCPC) (model 3776). The ES-SMPS can analyze particles in the range of 2-160 nm with the nano-DMA. The ES-SMPS system can use an alternate long-DMA (model 3081) to analyze particles in the range of 10-1000 nm. The electro spray is connected to CO₂ and N₂ gas tanks. The two inlet air streams combine for the carrier gas that transports the aerosols. The electro spray generates an aerosol of nanoparticles by drawing a liquid dispersion containing nanoparticles through the capillary tip, and the droplets are sprayed into the stream of dry air. Nanoparticles exiting the electro spray flow through the diffusion dryer where remaining liquid diffuses away from the particles and is captured by silica beads. The nanoparticle aerosol stream then enters the SMPS for size determination.

Particles entering the SMPS are charged using a radioactive source and their size is classified based on electrical mobility as the particle stream flows down the high voltage column of the nano-DMA. The particle trajectory down the column depends on electrical mobility, Z_p , of particle in applied electrical field and is defined by:

$$Z_p = \frac{neC_c}{3\pi\eta D_p} \quad \text{Eq. 3.1}$$

where n is the number of charges on the particle, e is the elementary charge, C_c is Cunningham slip correction, η is the dynamic viscosity of air and D_p is the diameter of the particle. The classifier scans a voltage range, and particles of a specific size are allowed to exit the DMA outlet at specified voltage values while particles outside that

size bin are carried with the excess air flow. Therefore, only particles within the narrow mobility diameter range of the DMA are allowed to exit the DMA outlet, and the polydisperse aerosol stream at the inlet is converted into a monodisperse aerosol stream at the outlet. The monodisperse particles then enter the UCPC where the particle concentration is determined as particles of known diameter are grown to an optically active size using butanol condensation and counted with a photodetector. The coupled particle sizing of the nano-DMA and particle counting of the UCPC allow the SMPS to provide a particle size distribution for a nanomaterial sample.

It should be noted that ES-SMPS data are shown in terms of bin and reported as $dN/d\log D_p$ versus $\log D_p$. The AIM (Aerosol Instrument Manager) software collects data in equally spaced size bins in log space (64 bins per decade) on the x-axis, mobility diameter. Therefore, the size bins become larger for larger mobility diameters. The number concentration on the y-axis is normalized to the bin size so that the total particle count over the full size range can be accurately compared. Thus, the total particle count within a bin, dN , is divided by the size of the bin, $d\log D_p$.

The primary advantages of the ES-SMPS method of characterizing particles are excellent resolution, discriminating between changes in size as small as 0.2 nm, and the ability to size particles as small as 2nm and up to 1000 nm. The desired size range is based on selection of the nano- or long-DMA, and further controlled by adjusting the air flow of the SMPS. The electrospray requires very small volumes (< 0.5 ml) of particle suspensions or solutions and consumes a negligible volume, even during extensive analysis times > 24 hrs. There are also challenges and limitations to using ES-SMPS analysis, as discussed below.

Figure 1.2 outlines nanomaterial properties that can influence characterization, and each of these properties is relevant for ES-SMPS characterization. The properties of shape, size, aggregation, concentration, surface composition, and active nanostructures are discussed as related to ES-SMPS characterization considerations. The shape of the particles will influence the resulting mobility diameter, since the particles are rotating through air in three dimensions. If the nanoparticles or aggregates are larger than the range of the ES-SMPS, measurements could be coupled to an aerodynamic particle sizer (APS) which is useful for detecting the larger particle agglomerates found in the micron size regime to obtain a more complete size distribution. Because the SMPS and APS instruments operate on very different principles the measured diameters would need to be related for comparison purposes.

For spherical particles, it is easy to relate the measured diameters from the different instruments mentioned above because no corrections need to be made for shape and volume, but for non-spherical particles or aggregates that are irregularly shaped these diameters are not equivalent. The APS reports an aerodynamic diameter, D_a , for the irregular particle by comparing the settling velocity to that of a spherical particle with a density of 1 g cm^{-3} to compute the particle size. The difference in measurements creates a need for a volume equivalent diameter, D_{ve} , which is defined as the volume of a sphere with the same volume as a particle with an irregular shape. The relationships between the mobility diameter, D_m , aerodynamic diameter, D_a , and volume equivalent diameter, D_{ve} , were outlined in Hudson et al⁵⁰.

$$D_{ve} = D_a \sqrt{\chi \frac{\rho_o}{\rho_p} \frac{C_s(D_a)}{C_s(D_{ve})}} \quad \text{Eq. 3.2}$$

$$D_{ve} = D_m \frac{C_s(D_{ve})}{\chi C_s(D_m)} \quad \text{Eq. 3.3}$$

$$D_m = D_a \chi^{3/2} \sqrt{\frac{\rho_o}{\rho_p} \frac{C_s(D_m) \sqrt{C_s(D_a)}}{C_s(D_{ve})^{3/2}}} \quad \text{Eq. 3.4,}$$

where χ is the dynamic shape factor, ρ_o is the reference density (1 g/cm³), ρ_p is the density of the particle, and $C_s(D_m)$, $C_s(D_a)$, and $C_s(D_{ve})$ are the Cunningham slip factors for the mobility, aerodynamic and volume equivalent diameters, respectively. For spherical particles the dynamic shape factor, χ , is equal to one, and the volume equivalent diameter (D_{ve}) is equal to the measured mobility diameter (D_m).

The nanomaterials studied by ES-SMPS in this work were well within the mobility diameter range of the ES-SMPS with the nano-DMA and were spherical in shape; therefore, no shape corrections were necessary. However, since nanomaterials are available in a wide range of sizes and shapes, it is important to be aware of particle shape effects and shape correction techniques when characterizing nanomaterials as aerosols. For example, the CNTs studied in this work were not characterized by ES-SMPS because the fibrous shape of the nanotubes would result in mobility diameters that do not represent the diameter or the length of the nanotubes. Thus, the data would not provide useful property information. If the shape of the nanomaterial is unknown, microscopy techniques could be used to assess particle shape prior to aerosol characterization.

The size of the nanoparticles is a property that affects ES-SMPS characterization. As mentioned earlier in this section, the desired size range of the ES-SMPS can be controlled with DMA selection and air flow through the SMPS. For nanoparticles in the range of 2-

64 nm, the nano-DMA was used with the high flow mode (15 lpm sheath flow, 1.5 lpm sample flow). For nanoparticles in the range of 4.5 - 160 nm, the nano-DMA was used in low flow mode (3 lpm sheath flow, 0.3 lpm sample flow). The low flow mode extends the mobility diameter range but results in increased diffusion losses for the smallest particles, < 10 nm. An optional “Diffusion Correction” can be applied to the data using the AIM software. This correction was only applied when the nanoparticles of interest were known to be < 10 nm in diameter; otherwise the correction will simply increase the background particle count in this small size range. For nanoparticles greater than 160 nm, the long-DMA could be used. For the nanomaterials studied in this work, the size range of the nano-DMA was sufficient for all samples by adjusting the flow rate to extend up to 160 nm when needed.

Aggregation and concentration are possibly the most important factors to consider when using ES-SMPS characterization. For an accurate characterization of nanoparticle size and aggregation properties, it is necessary to verify whether mobility diameters are those of the primary particles, or particle aggregates. To distinguish between aggregates of particles that are present in the suspension, and those formed during the aerosol generation process, a range of concentrations was considered for each nanomaterial studied. An appropriate concentration was chosen for each nanomaterial such that particle aggregates were not formed as the droplets dried. This was verified by checking that successively smaller mobility diameters did not result with decreased concentration. In the case of aggregation of the primary particles in suspension, individual particles could not be measured even with decreased concentrations. Nanomaterials that aggregate excessively can cause nearly instantaneous clogging of the electrospray capillary tubes

and cannot be studied using the ES-SMPS with standard 25-40 μ m tip capillaries.

Samples that are highly aggregated require more frequent changing of the capillary tubes as they clog. Suspensions were prepared by adding the solution (water or aqueous acidic solutions) to the powder sample and sonicating for 20 minutes for characterization studies, or \sim 1 minute for silver nanoparticle dissolution studies to disperse the particles without addition of the excess heat and energy of long sonication times. For copper nanoparticle dissolution studies the samples were not sonicated, but were analyzed with the ES-SMPS immediately upon adding solution to the powder.

Besides nanomaterial concentration, the concentration of salts or acids in solution can also influence ES-SMPS characterization. Background peaks resulting from ions in solution may be seen, or these ions may add to the surface of the nanoparticles, increasing the mobility diameter. Therefore, it is important to always analyze the background solution without nanoparticles to see the size and intensity of the background peak. High ionic concentration will also increase conductivity of the solution, and may cause the sample to spray in an unstable corona mode. If the sample enters this mode, it is easily seen by an erratic conductivity reading on the electrospray, and can also be seen by viewing the capillary tip where the sample is sputtering from the tip rather than spraying with the stable cone-jet shape. It is especially important to monitor highly ionic solutions during analysis, because scans acquired during corona mode can result in extremely monodisperse PSDs with high particle counts, but the results are inaccurate and unreliable. Samples in corona mode can be returned to the desired cone-jet mode by decreasing the voltage setting on the electrospray.

The surface composition of the nanoparticles will influence the ES-SMPS

characterization by adding to the size of the nanoparticles and/or affecting their propensity to aggregate. Many nanomaterials are coated or functionalized to control their properties for specific applications. These surface modifications affect the size of primary particles, aggregation, and interactions with the surrounding solution. It is important to understand the surface composition of the nanoparticles to interpret ES-SMPS results. As much information as possible specifying surface composition should be provided by manufacturers or synthesis labs, and complementary techniques, such as XPS, can be used to characterize the surface chemistry of nanomaterials. Two nanomaterials of the same bulk composition may behave very differently in solution due to surface composition. This was seen with ES-SMPS analysis of bare silver nanoparticles (Chapter 7) and polymer-coated silver nanoparticles (Chapter 4) in water.

ES-SMPS analysis must consider the stability of active nanostructures, or nanoparticles with properties that change on the time scale of analysis (~ 2 - 2.5 min/scan). This was not relevant for the nanomaterials characterized in water in this work but was very important for nanomaterials analyzed in acidic solutions. Experiments were designed so that dissolution of copper nanoparticles could be monitored in real time using ES-SMPS analysis. A range of HCl concentrations was studied so that dissolution did not occur too quickly to be observed with the ES-SMPS. However, with the silver nanoparticles, the HNO_3 concentration that induced dissolution of the smaller primary particles (≤ 5 nm) caused complete dissolution too quickly to be observed using ES-SMPS. The parameters controlling a chemical processes would need to be varied to allow at least ~ 15 - 20 minutes for completion for the ES-SMPS to collect real time, reproducible data.

While these nanomaterial properties (shape, size, aggregation, concentration, surface composition, and active nanostructures) present challenges for ES-SMPS characterization, they can often be accounted for or controlled with experimental design. It is important to know as much about the nanomaterial as possible, analyze a range of nanomaterial concentrations, control the solution composition, collect background scans, monitor sample spraying during analysis, and collect reproducible results. ES-SMPS data was often coupled with other bulk and surface techniques to verify results and understand PSDs shifts.

ES-SMPS and TEM analysis were coupled for the work in Chapter 4, Section 4.4, and Chapter 7. Using this coupled approach, the nanoparticles are deposited on a TEM grid between the Nano-DMA and the UCPC (Figure 3.2). The aerosol flow stream exiting the nano-DMA is directed onto a TEM grid contained in a leak proof holder, with the flow perpendicular to the grid, and then exits the holder and enters the UCPC. The TEM analysis and ES-SMPS PSDs represent the same nanoparticle population and can be directly compared.

CHAPTER 4

CHARACTERIZATION OF NANOMATERIALS

4.1 Introduction

As discussed previously, there is a need for characterization of nanomaterial properties to accompany investigations of nanomaterials in applications and environmental health and safety studies. This broad goal will be achieved through numerous characterization studies of specific nanomaterials with varying material specifications and properties. These studies can be combined throughout the scientific community, and a set of standard nanomaterial properties can begin to development. Currently, commercially available nanomaterials show too much variation from manufacturer to manufacturer, batch to batch, and characterized properties compared with specified properties. Therefore, at the research level, it remains essential to compliment any nanomaterial study with a full characterization of material properties. The aim of each interdisciplinary study, the material properties or potential effects of interest, and the methods used to analyze the material and evaluate the results should be considered in designing the characterization.

This chapter presents characterization data on some of the most commonly manufactured nanomaterials, including carbon nanotubes, silver nanoparticles, and titanium dioxide nanoparticles. Carbon nanotubes were characterized in preparation for inhalation studies to evaluate their toxicity. Important properties affecting inhalation toxicity include particle size (nanotube diameter and length), specific surface area, particle aggregation, and amounts of contaminants present in the sample. Polymer-coated silver nanoparticles were characterized to determine the coating thickness to aid the manufacturer in accurately specifying the material's properties. Titanium dioxide and

polymer-coated silver nanoparticles were characterized as part of a project evaluating nanoparticle aerosol generation methods for application in inhalation studies. This involved comparing PSDs determined using the ES-SMPS with both the manufacturer's specified particle size and the known particle size from TEM characterization.

Synthesized gold nanoparticles designed with controlled properties for integration into microfluidic devices with potential applications in biosensing were also characterized.

These nanoparticles were analyzed to determine PSDs to provide insights into particle-coating and particle-solution interactions.

4.2 Characterization Methods

The bulk and surface characterization methods used to obtain the results presented in this chapter were outlined in Tables 3.3 and 3.4. One or more of these techniques were combined to obtain the desired nanomaterial property information for the objective of each study. All materials were used as received unless otherwise noted.

4.3 Carbon Nanotube Characterization

4.3.1 Microscopy and Specific Surface Area Analysis SWCNTs and MWCNTs were analyzed with SEM and TEM to observe morphology, aggregation, contamination, and determine nanotube diameters. Figure 4.1 shows sample SEM and TEM images for SWCNTs, and Figure 4.2 shows sample SEM and TEM images for MWCNTs. Images were analyzed using ImageJ software to determine size distributions for nanotube diameter for both CNT samples, as shown in Figure 4.3. The specific surface area of the SWCNTs and MWCNTs were determined to be $457 \pm 4 \text{ m}^2/\text{g}$ and $575 \pm 10 \text{ m}^2/\text{g}$, respectively, from five averaged BET measurements.

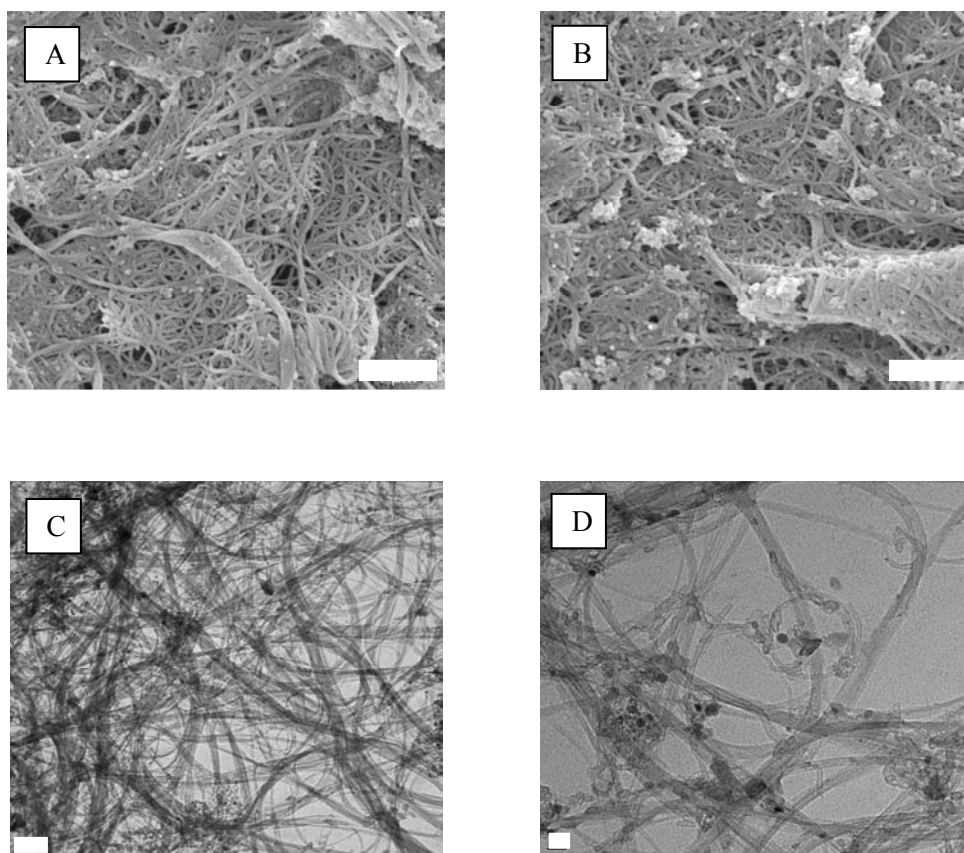


Figure 4.1 Selected images of single walled carbon nanotubes, SEM (A, B) and TEM (C, D). Scale bars are 1 μm (A), 500 nm (B), 100 nm (C), and 20 nm (D).

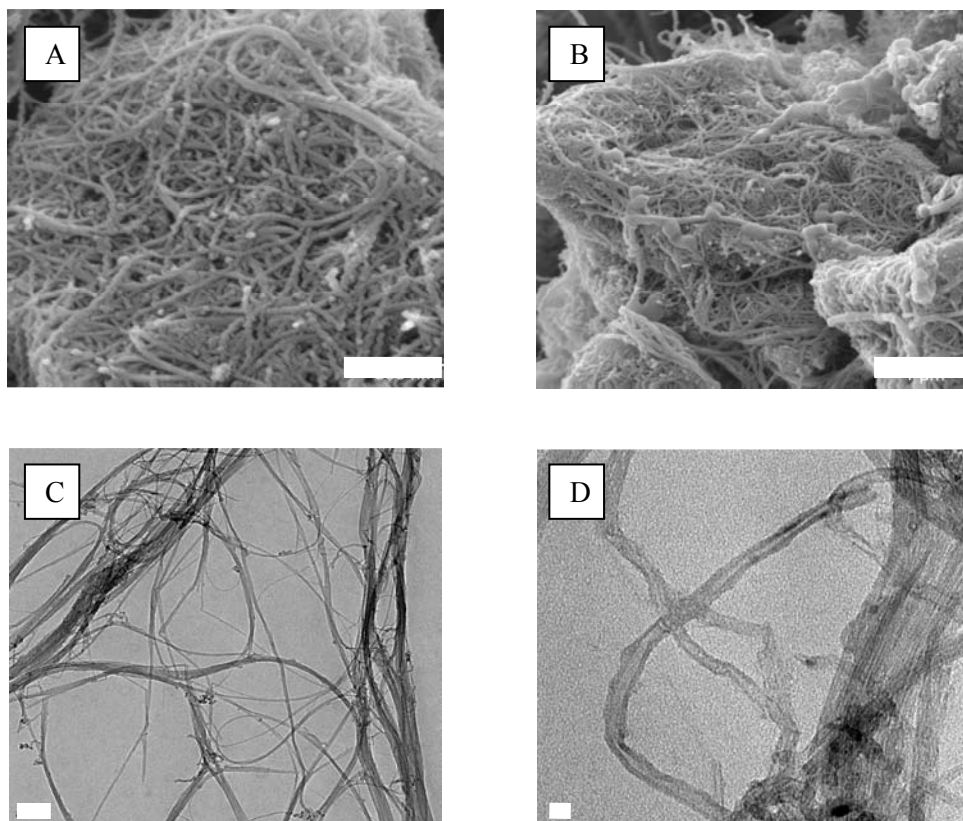


Figure 4.2 Selected images of multi-walled carbon nanotubes, SEM (A, B) and TEM (C, D). Scale bars are 500 nm (A), 1 μm (B), 100 nm (C), and 20 nm (D).

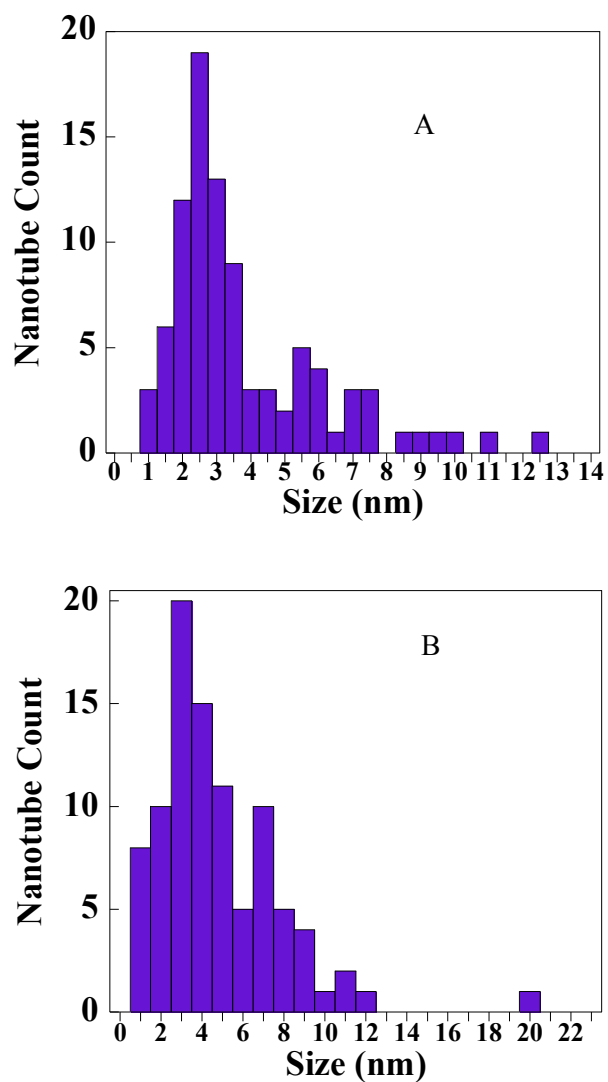


Figure 4.3 Diameter size distributions from TEM analysis using ImageJ software for single walled carbon nanotubes (A) and multi-walled carbon nanotubes (B).

4.3.2 Raman Spectroscopy SWCNTs and MWCNTs were analyzed using Raman spectroscopy to approximate tube diameter, identify characteristic graphite peaks, classify conductivity, and estimate carbonaceous contamination. The results for both CNT samples are shown in Figure 4.4.

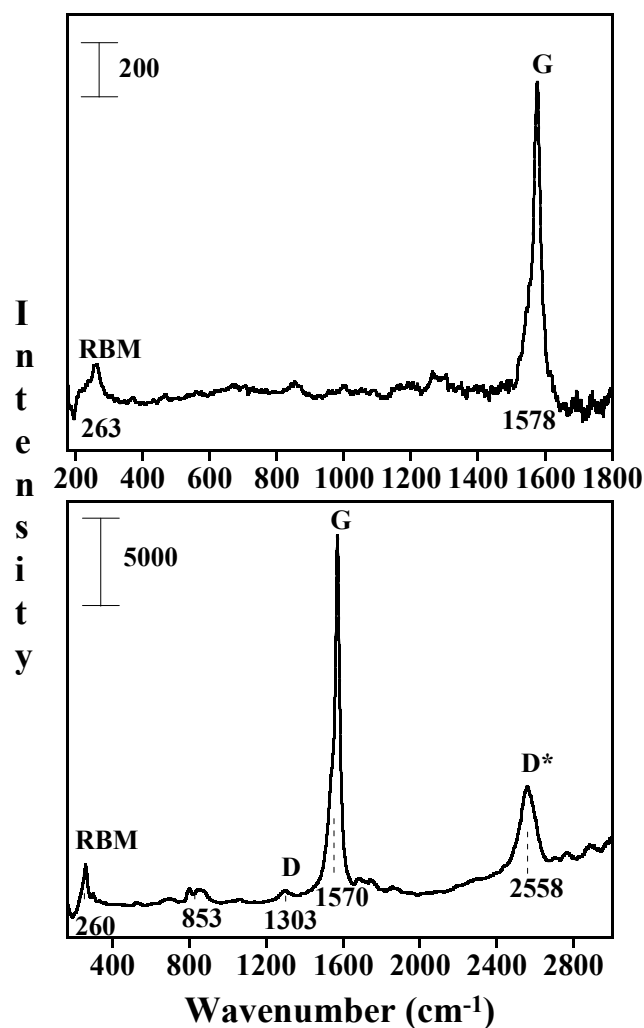


Figure 4.4 Raman spectra of single walled carbon nanotubes (upper) and multi-walled carbon nanotubes (lower). RBM = Radial Breathing Mode, G Band = Tangential Mode, D Band = Disorder-induced Mode, and D* Band = Overtone (2*D).

4.3.3 X-ray Photoelectron Spectroscopy SWCNTs and MWCNTs were analyzed with x-ray photoelectron spectroscopy to quantify metal contamination. The results for both CNT samples are given in Table 4.1.

Table 4.1 XPS Analysis of Carbon Nanotubes

Carbon Nanotube Sample	SWCNT	MWCNT
Carbon (Atomic %)	98.7	99.0
Oxygen (Atomic %)	1.2	1.0
Metal (Atomic %)	Co < 0.2 %	None detected

4.3.4 Summary of Carbon Nanotube Results Results of the CNT characterization are summarized in Table 4.2. SEM and TEM images show tangled nanotubes and spherical contamination for both SWCNTs and MWCNTs. Measurement of tube diameters from TEM gives 1.8 ± 2.3 nm and 3.3 ± 3 nm for SWCNTs and MWCNTs, respectively. Comparison with Table 3.1 shows the diameter and SSA of the SWCNTs are in good agreement with the manufacturer's specifications, but the tube diameter for the MWCNTs is larger, and shows a larger size distribution, than the manufacturer's specifications. The MWCNTs SSA is also much larger than suggested by the manufacturer. XPS analysis verifies very pure samples with respect to metal contamination, indicating the spherical particles seen in the SEM and TEM images are

likely carbonaceous. Such low metal content suggest these are appropriate samples for inhalation studies, since any toxic effects would not be confused with metal contamination.

Raman spectroscopy results provide additional material information through assignment of spectral peaks. The radial breathing mode (RBM) is indicative of CNTs, and the wavenumber of this mode can be used to estimate the diameter of the bundled CNTS⁵¹. These results indicate diameters of $\sim 0.88 - 1.1$ nm for both the SWCNTs and MWCNTs. The G-band is a stretching mode in the graphite plane. The shape of the G-band is indicative of the electronic properties of CNTs. The symmetric shape of the G-band in both SWCNTs and MWCNTs indicates semiconductive CNTs as opposed to metallic CNTs. The D-band is a disorder mode observed for MWCNTs and indicates contamination if observed for SWCNTs. The ratio of the G-band and D-band intensities is indicative of the purity of a CNT sample. The large G-band and very weak D-band shown here indicate a high purity sample⁵².

Table 4.2 Characterization Summary for Carbon Nanotubes

Result	Method	SWCNT	MWCNT
Mode Diameter (nm)	TEM analysis	1.8 ± 2.3	3.3 ± 3
Specific Surface Area (m ² /g)	BET measurement	457 ± 4	575 ± 10
Metal Contamination	XPS	Co < 0.2 %	None detected
Conductivity	Raman spectroscopy	Semiconductive	Semiconductive

4.4 Polymer-Coated Silver Nanoparticle Size Characterization Manufactured silver nanoparticles with a polymer coating were received as a colloidal suspension of < 1 wt % Ag in water. The manufacturer estimates the coating thickness to be 2-3 nm but has no direct means of determining the coating thickness. With a silver core specified at 2-5 nm, the coating thickness contributes largely to the total particle diameter and volume. Therefore, it is important to obtain an accurate coating thickness value and distribution for a useful characterization.

This work used coupled ES-SMPS and TEM analysis to determine size distributions for the silver core and the total particle diameter, including the core plus the coating. Organic coatings have minimal contrast in electron microscopy, making it difficult to determine the coating thickness, and usually only the size of the inorganic core can be measured. By coupling TEM with the ES-SMPS, the coating thickness can be quantified by subtracting the core size from the total particle size. The results for the silver core PSD from TEM analysis are shown in Figure 4.5, and the PSD for the total particle diameter from ES-SMPS analysis is shown in Figure 4.6.

The TEM image shows isolated nanoparticles, and peaks at 3 nm and 4.5 nm are observed. The PSD ranges from 2-10 nm for the silver core. This range is larger than the manufacturer's specified 2-5 nm, however, it can be seen that the particle count drops rapidly above 5 nm, and a very small fraction of particles exist within 6-10 nm. For ES-SMPS analysis, a range of dilutions of the stock suspension were considered to ensure primary particles were detected. This was verified by checking that successively

smaller mobility diameters did not result with decreased concentration. The data presented in Figure 4.6 use a 0.5 wt % Ag suspension. Below this concentration, particle

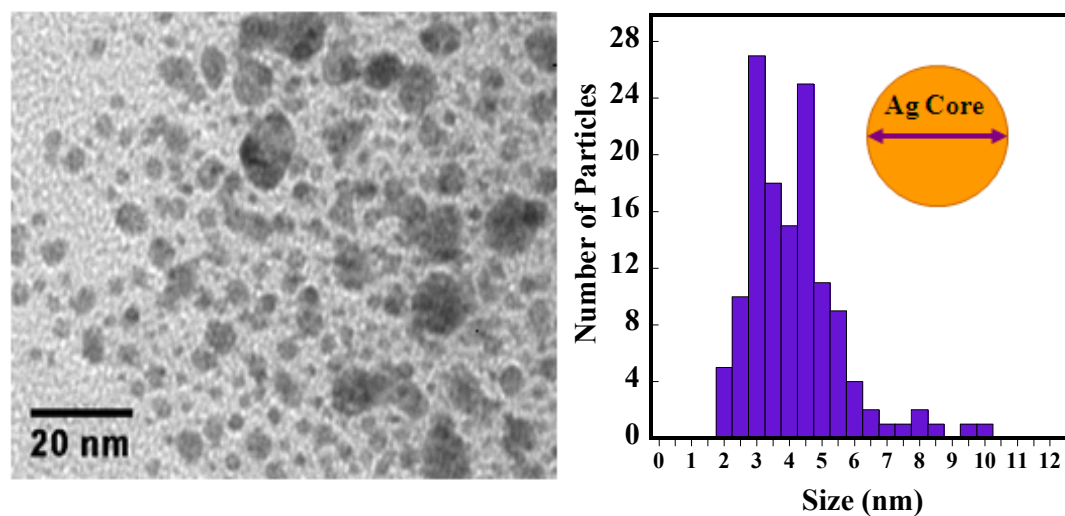


Figure 4.5 TEM image (left) and corresponding particle size distribution (right) using ImageJ software for polymer-coated silver nanoparticles.

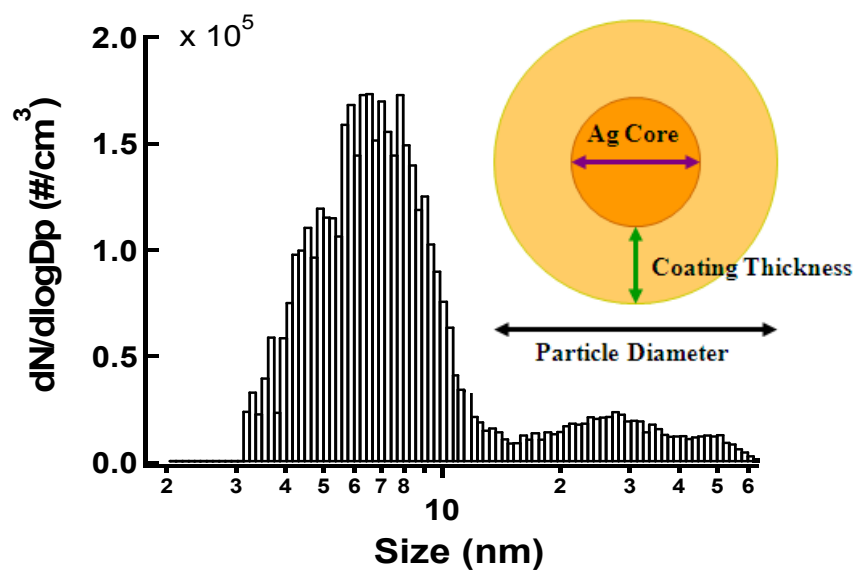


Figure 4.6 ES-SMPS particle size distribution of polymer-coated silver nanoparticles.

count dropped so that the PSD due to primary particles was not clearly distinguishable. The PSD from the ES-SMPS shows two peaks for the primary particles at 4.8 nm and 7 nm. The small distribution at ~ 25 nm is most likely due to a small fraction of droplets containing multiple particles. By the manufacturer's specifications, the total particles size should range from 6-11 nm. The data show a larger PSD from ~ 3-15 nm for the primary particles (core plus coating).

Comparison of the peak maxima for the PSDs from TEM and the ES-SMPS gives a coating thickness of ~ 1-2.5 nm. This is smaller than the specified 2-3 nm. These results confirm a larger PSD for the silver core and the total particle diameters, and a smaller polymer coating thickness, relative to the manufacturer's specifications. The characterization using coupled TEM and ES-SMPS analysis provide detailed PSD data for a complete description of organic coated nanoparticle size.

4.5 Titanium Dioxide and Polymer-Coated Silver Nanoparticle Characterization

Titanium dioxide and polymer-coated silver nanoparticles were characterized as part of a project to evaluate nanoparticle aerosol generation methods from bulk powders for inhalation exposure studies. The goal of this study was to test a variety of wet and dry aerosolization techniques for their ability to produce an acceptable aerosol from bulk powders applicable for animal exposure studies. Characteristics of an acceptable aerosol include: (1) a consistent concentration maintained at a desired level for hours, (2) a homogenous composition free from contaminants, and (3) a size distribution that is preferably unimodal and has both a small geometric mean diameter (< 200 nm) and small geometric standard deviation (< 2.5 nm).

The dry methods tested included a small-scale powder disperser, acoustic dry aerosol generator/elutriator, and fluidized bed aerosol generator. The wet methods tested included the electrospray aerosol generator and the Collison nebulizer. A variety of nanoparticle powders were used to test the aerosol generation methods including titanium dioxide and silicon dioxide with primary particle sizes of 21 nm and 20 nm, respectively, as well as single walled carbon nanotubes. A 5-nm primary particle size TiO₂ powder and 6-11 nm polymer-coated silver nanoparticles were also tested but only with the use of the electrospray. These nanoparticle powder types were selected because they have different physical characteristics that may affect the way they are aerosolized. Further details of the powder characteristics and methods can be found in Schmoll et al.⁵³

When conducting inhalation toxicology studies it is important to produce an aerosol with a consistent concentration over time that is reproducible within and between days of exposure so that the dose is known and uniform. The electrospray was not capable of producing an aerosol from the 21-nm TiO₂ powder due to excessive aggregation that clogged the capillary. However, when 5-nm TiO₂ was aerosolized using the electrospray, a consistent concentration over time with counts that varied less than 5% from the average was observed. A consistent aerosol concentration over time was also observed when ~6-11-nm Ag nanoparticles were suspended in water and aerosolized using the electrospray. Aerosolization of 5-nm TiO₂ and ~6-11-nm Ag using the electrospray produced average counts of 70,750 per cm³ and 15,770 per cm³, respectively (Figure 4.7).

The electrospray was the only wet aerosol method able to produce an aerosol with a geometric mean similar to the primary particle size of a powder. Even the electrospray

was unable to produce a monodisperse aerosol with a geometric mean that coincided with the primary particle size except in the case of the aerosol of silver particles coated with a polymer to enhance dispersion and prevent agglomeration. The 5-nm TiO₂ aerosol produced by the electro spray using water was bimodal with a major peak at 25.9 nm and minor peak at 5.9 nm and a geometric mean of 21.4 nm, and the Ag (~6-11- nm) aerosol that was produced by suspending in water and electro spraying had a geometric mean of 7.76 nm and was bimodal with a major peak at 6.61 nm and a minor peak at 27.9 nm (Figure 4.8).

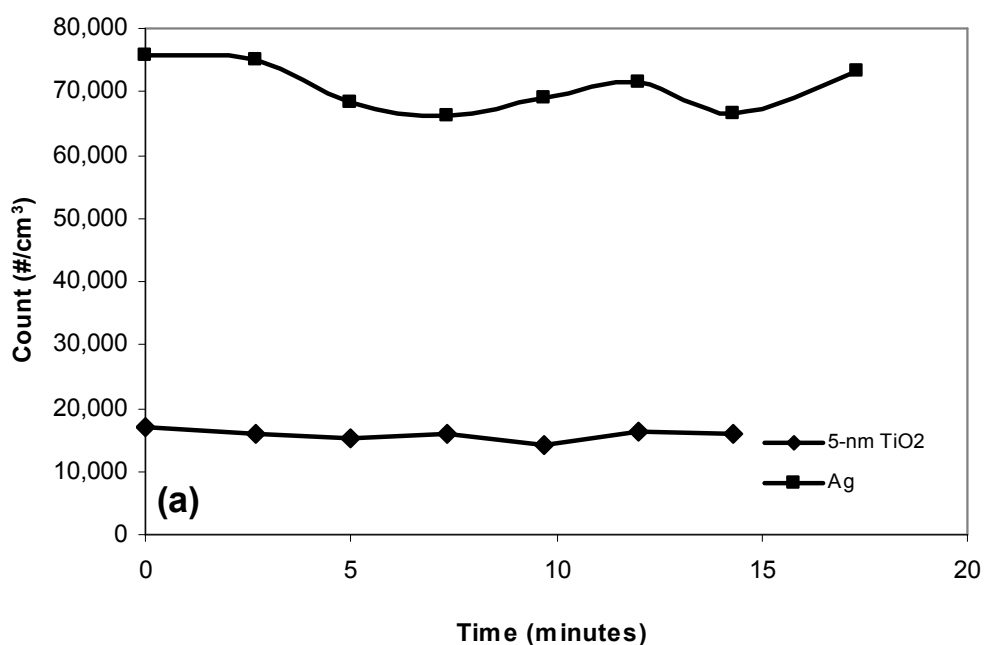


Figure 4.7 5-nm TiO₂ and ~6-11-nm Ag aerosol concentration over time produced by water-based electro spray method.

The aerosols produced through nebulization and the water-based electrospray method were not homogenous; however the non-nanopowder component can be attributed to residual impurities found in the ultrapure water. The background impurities found in water can cause an aerosolized nanoparticle size distribution to be bimodal unless a concentrated solution is used. Background contamination was observed in aerosols produced by both wet generation methods that was attributed to residuals found in the ultrapure water used to suspend the nanopowders. Various methods were used to filter the water and various sources of water were tried; but background contamination was still observed when ultrapure water alone was tested. The presence of this contamination can be seen in the size distribution data shown in Figure 4.8, which shows a peak diameter near 20 nm. The intensity of the water background was nearly three orders of magnitude lower than the nanoparticle samples.

In summary, none of the devices investigated were able to satisfy all criteria for an acceptable aerosol. A detailed evaluation of each method tested with each powder can be found in Schmoll et al.⁵³ Three methods were able to produce a consistent concentration over time, the acoustic dry aerosol generator/elutriator, nebulizer, and electrospray. However, the acoustic dry aerosol generator/elutriator was only able to produce a consistent concentration over time when aerosolizing SiO₂. The electrospray was able to produce a consistent concentration over time for 5-nm TiO₂ and ~6-11 nm Ag, but not for 21-nm TiO₂.

None of the generation methods except for the electrospray were able to produce an aerosol with a size distribution similar to that of the primary particle size indicated by the manufacturer, but most were capable of producing an agglomerate size distribution with a

geometric mean < 200 nm. Interestingly, sonication of the powder solution did not decrease the size distribution of the resulting aerosol.

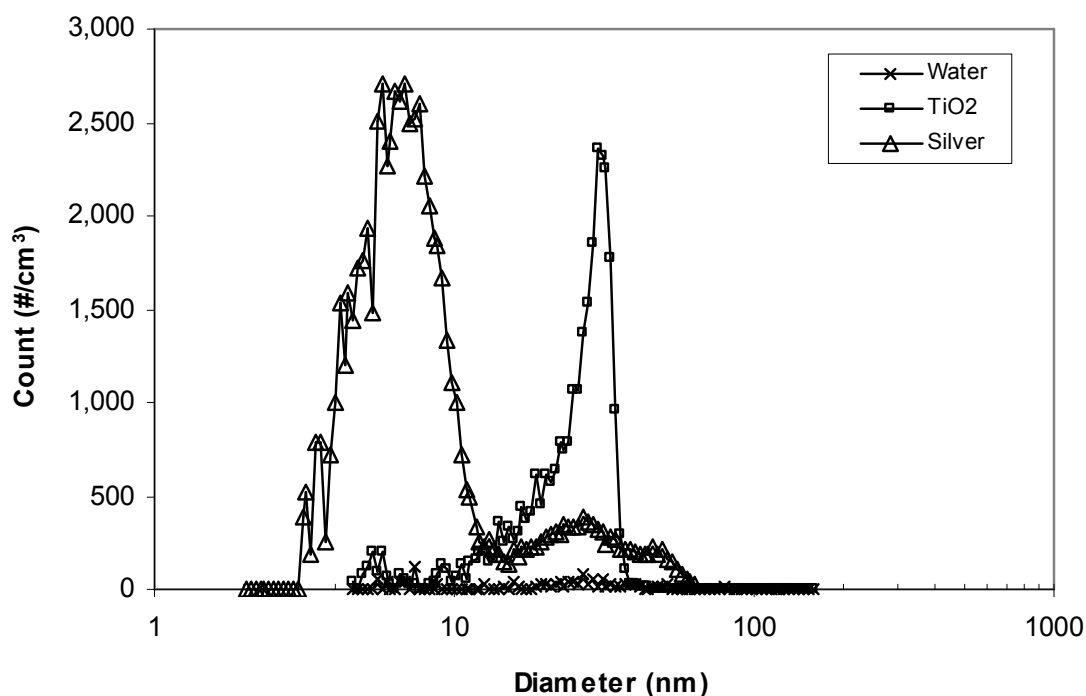


Figure 4.8 5-nm TiO₂, ~6-11-nm Ag plus polymer coating, and background water size distributions produced by an electro spray generator.

There were two devices, the small-scale powder disperser and acoustic dry aerosol generator/elutriator, which produced a homogeneous aerosol. The wet methods produced a non-homogeneous aerosol, but it is suspected that the impurities contributing to the heterogeneity of the aerosol may be attributed to residual salts in the water source and are therefore nontoxic. The presence of these impurities implies the need for a water-only exposure to serve as a control. However, results suggest that an adequate powder

solution concentration can overwhelm the secondary peak caused by the water contaminants. Based on the three evaluation criteria, results suggest the nebulizer was the most useful device of those tested.

4.6 Synthesized Gold Nanoparticle Characterization

4.6.1 Silica-Coated Gold Nanoparticles Surface enhanced Raman spectroscopy (SERS) is a technique that uses a metallic surface to enhance the Raman scattering signal intensity of adsorbed molecules. Consistent SERS signals can be achieved by controlling the properties (size, shape, chemical composition) of the metallic substrate and surrounding chemical environment. To improve SERS measurements, the metal particles can be protected with surface capping molecules or encapsulated in silica shells^{54, 55}.

This work characterizes silica-coated gold nanoparticles synthesized as a step toward the development of encapsulated gold nanoparticles in microporous silica membranes⁵⁶. The microporous silica membranes are designed to overcome diffusion limitations of silica-coated nanoparticles for SERS applications. The nanoparticles were received and characterized as synthesized, according to Roca et al.⁵⁶, with specified size properties based on TEM analysis. The work presented here analyzed TEM images provided by Dr. Maryuri Roca (laboratory of Dr. Amanda Haes, The University of Iowa) using ImageJ software for PSDs of the bare and coated gold nanoparticles (Figure 4.9). The ES-SMPS was used to measure the PSDs of the bare gold nanoparticles and silica-coated nanoparticles suspended in a sodium citrate solution for stabilization (Figure 4.10). Coating thickness and particle interactions with the local salt environment were quantified.

The peak maxima for the PSDs in Figure 4.9 are larger than the specified size by ~ 1 - 2 nm for both nanoparticle samples. This is due to differences in the measurement methods applied to the TEM images. The specified size was determined with ImageJ software using an automated measurement that averages diameters across three lines that intersect the center for each particle. The characterized PSDs were determined with ImageJ software by manually measuring the diameter across the largest distance through the center for each particle so the data could be directly compared with ES-SMPS PSDs, which represent diameters based on the largest distance across a particle. For these near spherical particles the difference is small.

ES-SMPS PSDs in Figure 4.10 show the bare nanoparticles with an average diameter of 20 nm, and the silica-coated nanoparticles with an average diameter of 46 nm. The shoulder at ~ 85 nm for the silica-coated nanoparticle PSD is likely due to larger, elliptical particles and/or agglomerates. The coating thickness determined by TEM and ES-SMPS analysis agree and are also in agreement with the specified coating thickness. The ES-SMPS peak maxima are ~ 6 nm greater than TEM results for both the bare and coated nanoparticles, indicating that the sodium citrate solution is interacting with the particles to form a surface layer(s).

Identical surface layer thickness (3 nm) despite the large size difference for the bare and coated samples (~ 26 nm) indicates a molecular interaction with the particle surface. If the citrate ions were simply coating the particles due to drying of the droplets exiting the electrospray, it would be expected that the bare particles would have a larger surface coating thickness due to 1) a greater solution phase volume per droplet because the solid

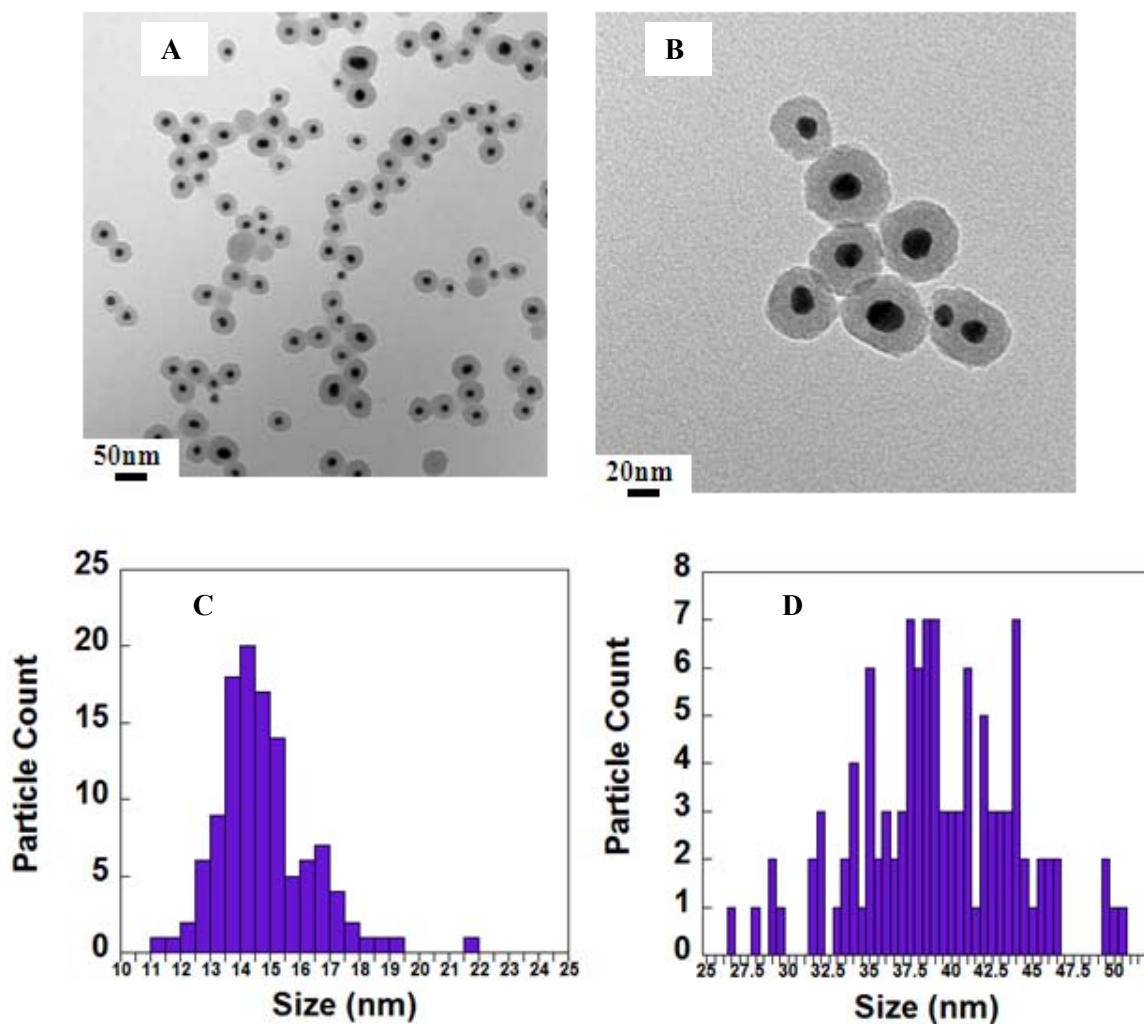


Figure 4.9 TEM images of silica-coated gold nanoparticles (A, B). Particle size distributions for bare (C), and silica-coated gold nanoparticles (D) using ImageJ software. (TEM images by Dr. Maryuri Roca, laboratory of Dr. Amanda Haes, The University of Iowa).

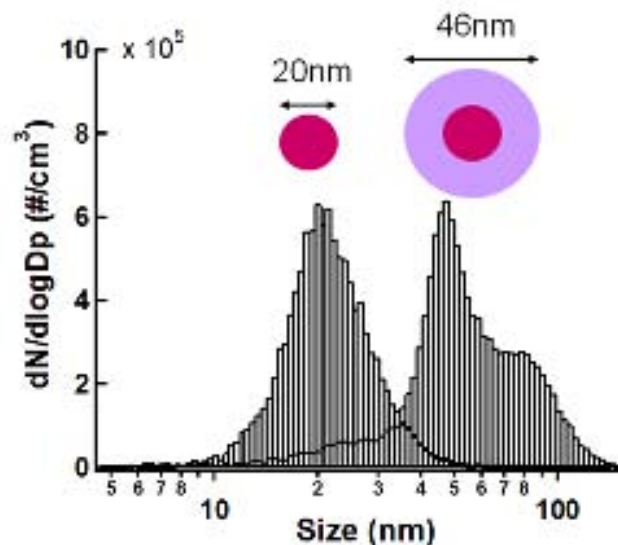


Figure 4.10 ES-SMPS size distributions for bare and silica-coated gold nanoparticles suspended in a 40 nM sodium citrate solution.

particles are smaller, and 2) the smaller surface area of a bare particle compared with a silica-coated particle. To better understand the particle-citrate interaction, a study of bare gold nanoparticles in solutions of varying sodium citrate concentration was designed and is presented in the following section.

4.6.2 Sodium Citrate Stabilized Gold Nanoparticles A charged colloidal particle in solution with ions will be surrounded by ions of the opposite charge. The arrangement of the electric charges on the particle, plus the opposite charges in the solution that surround the particle surface, is called the electrical double layer (DL)⁵⁴. The thickness of the DL is a function of ionic concentration of the solution and decreases as the concentration increases due to compression of the double layer. The thickness of the DL is the quantity $1/\kappa$, where κ is the Debye-Huckel parameter, expressed as

$$\kappa = (e^2 \sum n_i^0 z_i^2) / (\epsilon k T)^{1/2} \quad \text{Eq. 4.1}$$

where e is the elementary charge, n_i^0 is the number of ions of species i per unit volume in the bulk solution, z_i is the ion valency of species i , ϵ is the dielectric constant, k is the Boltzmann constant, and T is the temperature.

The apparent particle-citrate interaction observed for the gold nanoparticles pointed toward a citrate DL with the particle surface. A study was designed with the goal of quantifying the change in the thickness of the citrate DL with changes in citrate concentration using the ES-SMPS. To achieve this, bare gold nanoparticles were synthesized by Anna Volkert (laboratory of Dr. Amanda Haes, The University of Iowa) and suspended in solutions with varying concentrations ranging from 1 – 10 mM sodium citrate. The suspensions were analyzed with the ES-SMPS to obtain PSDs for each concentration. The peak maxima of the ES-SMPS PSDs were then compared to predicted particle sizes calculated using Eq. 4.1 to estimate the DL thickness and add that thickness to the particle size from TEM for the bare particles. Gold nanoparticle size and concentration were controlled for minimal variation, and ES-SMPS analyses were all conducted at ambient temperature, making the sodium citrate concentration the only significant variable factor affecting the Debye-Huckel parameter in Eq. 4.1.

TEM image analysis by Anna Volkert showed the gold nanoparticles were 13.6 ± 1 nm in diameter. Based on this known particle size for the bare gold nanoparticles, a predicted total particle size (bare particle plus citrate DL) was calculated for each sodium citrate solution using Eq. 4.1. Table 4.3 reports results for the predicted ES-SMPS total particle size and experimental ES-SMPS particle size. The calculated DL thickness has a lower limit, accounting for the citrate ions in solution, and an upper limit, accounting for all ions in solution (Na, Cl from the gold salt). Therefore, the predicted ES-SMPS

particle size is reported as a range. Results show good agreement between the predicted ES-SMPS particle size plus citrate DL and experimental ES-SMPS particle size. It should be noted that gold nanoparticles in 0 mM sodium citrate could not be successfully analyzed with the ES-SMPS due to insufficient conductivity of the suspension without the salt solution. Increased particle concentration can be used to increase conductivity, but typical particle concentrations in water for ES-SMPS analysis are 5-6 orders of magnitude greater than the concentration used in this study. Such significant increased concentration is hard to achieve using solution-phase synthetic methods. The sodium citrate solutions alone were also analyzed with the ES-SMPS for comparison.

Table 4.3 Predicted and Experimental ES-SMPS Particle Size for Gold Nanoparticles in Sodium Citrate Solutions Based on Calculated Citrate Double Layer Thickness

Sodium Citrate Concentration (mM)	Predicted ES-SMPS Particle Size (nm)	Experimental ES-SMPS Particle Size (nm)
1	19.1-21.5	21.4
2	17.5-18.9	18.9
3	16.7-17.7	17.4
5	15.8-16.5	15.7
10	14.9-15.3	14.8

The ES-SMPS PSD data for each gold nanoparticle suspension with corresponding sodium citrate solution are shown in Figure 4.11. The data show the shift in the PSD between the sodium citrate background solution and the gold nanoparticle suspension. However, the shift is small due to the bare nanoparticle size and the selected sodium citrate concentrations that result in a citrate DL thickness that brings the total particle size near the PSD of the background solution. Figure 4.12 shows the trend in peak maxima

for the sodium citrate concentrations and the peak maxima for the gold nanoparticles with citrate DL. The total particle size for the suspended gold nanoparticles decreases with sodium citrate concentration due to double layer compression. It could be expected that for a given bare nanoparticle size, these data will tend towards closer peak maxima with increased sodium citrate concentration, and may reach a point of PSD overlap, as is seen in Figure 4.11 at 10 mM. To overcome this result, the nanoparticle size needs to be large enough that even with double layer compression at high salt concentrations the total particle size will be substantially greater than the salt background.

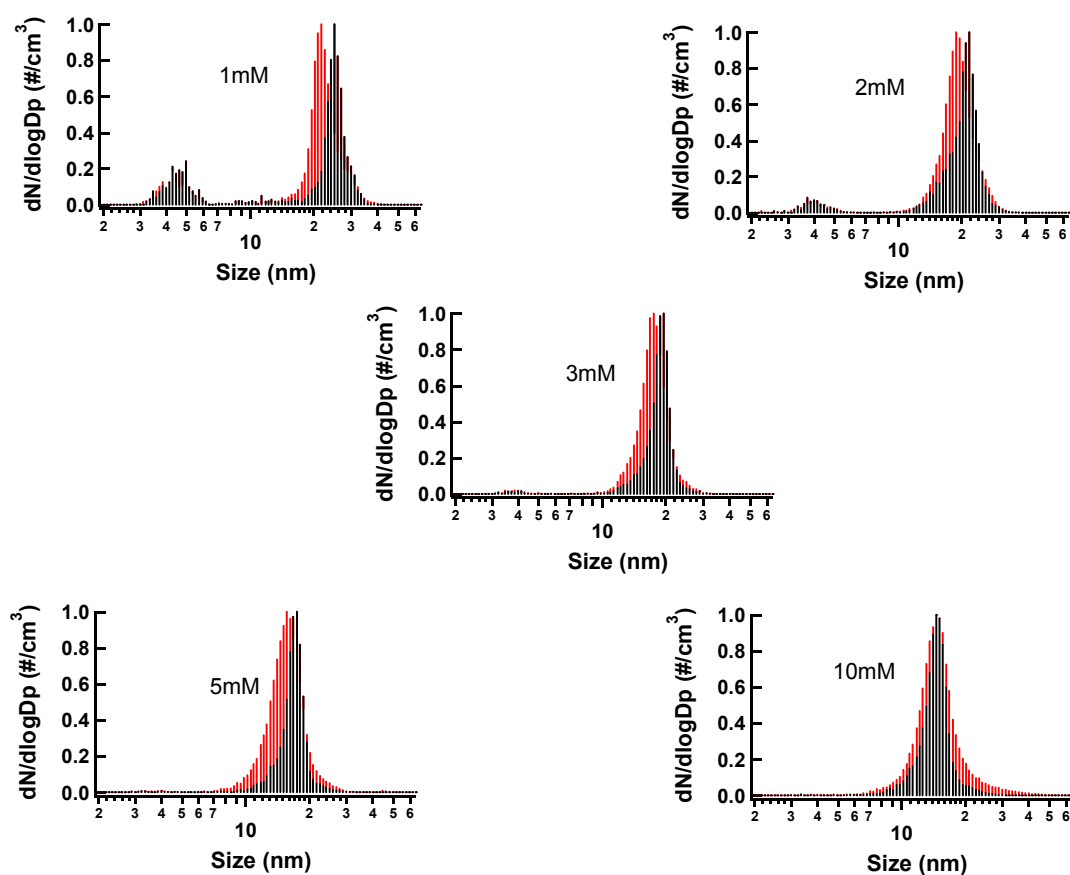


Figure 4.11 ES-SMPS results for gold nanoparticle suspensions (red) and corresponding sodium citrate background (black).

Although the PSDs in Figure 4.11 show some overlap, it should be noted that the shift in peak maxima between the nanoparticles and the salt background is ~ 4 nm, and this is a shift of nearly 25% relative to the nanoparticle PSD. While the PSD overlap appears considerable, a 4 nm separation is significant with respect to the capabilities of the ES-SMPS, and the consistency of the data for these size-controlled nanoparticles and salt background is absolute, with PSD peak maxima that do not shift by one size bin with continuous analysis. These data indicate a greater separation of the nanoparticle and salt peaks should be achieved with larger nanoparticles, and the separation of the peaks will confirm the citrate DL thickness is accurately measured using the ES-SMPS.

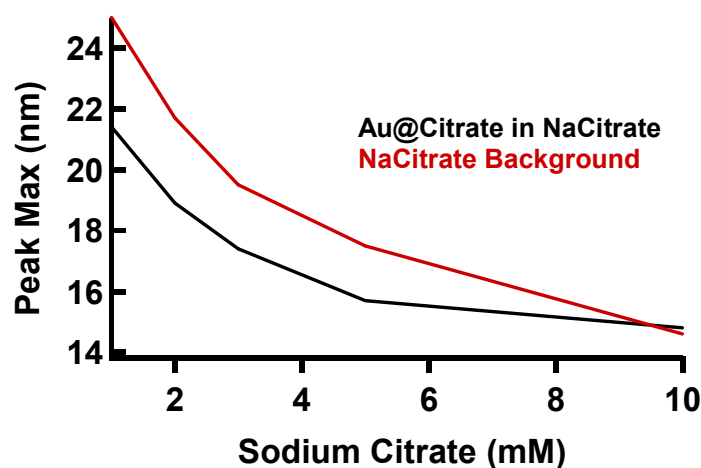


Figure 4.12 Peak maxima for gold nanoparticles in sodium citrate (Au@Citrate in NaCitrate) and sodium citrate solutions (NaCitrate Background) as a function of sodium citrate concentration.

4.7 Summary of Nanomaterial Characterization

The work presented in this chapter highlights a variety of needs related to nanomaterial characterization. The CNT work is an example of the complete characterization of material properties that must accompany any toxicity study of nanomaterials. The PSD characterization of polymer-coated silver nanoparticles demonstrates how applying appropriate methods, and coupling different methods, can provide additional information that may be difficult to obtain in order to more accurately specify the properties of a manufactured nanomaterial. The characterization of titanium dioxide nanoparticles and polymer-coated silver nanoparticles relates to the need for evaluation of methods to study nanomaterials to identify the appropriate method for specific applications with specific nanomaterials. The synthesized gold nanoparticle characterization highlights the need for fundamental studies of nanoparticle surface chemistry to understand physiochemical properties and interactions that can influence particle behavior and performance in applications. These characterization data are part of collaborations between researchers from Chemical and Biochemical Engineering, Occupational and Environmental Health, Chemistry, and industry, and point toward the inherently interdisciplinary nature of nanoscience and nanotechnology.

4.8 Acknowledgements

This material is based on work supported by NIOSH R01 OH008806-01, NIOSH R01 OH009448, NIEHS P30 ES05605-11, and the DoD through the National Defense Science and Engineering Graduate (NDSEG) fellowship program.

CHAPTER 5

AIRBORNE MONITORING TO DISTINGUISH ENGINEERED NANOMATERIALS FROM INCIDENTAL PARTICLES FOR ENVIRONMENTAL HEALTH AND SAFETY

5.1 Introduction

Incidental nanoparticles, byproducts of combustion or hot processes, have been associated with a range of adverse health effects resulting from inhalation^{57, 58}. Engineered nanomaterials, materials designed with at least one dimension < 100 nm, may also pose inhalation hazards that are the same or unique compared with incidental nanoparticles. Current estimates suggest that 2 million workers will be employed in nanotechnology industries by 2020⁵⁹ and may be exposed to airborne nanomaterials. A way to distinguish airborne engineered nanomaterials from incidental particles would be of practical value when assessing workplace inhalation risks. Each engineered nanomaterial will likely have unique toxicity relative to other engineered nanomaterials and the incidental nanoparticles they may coincide with. Conventional methods used to assess risk from airborne particles that use a mass-based metric are ill suited for assessing nanoparticle exposure because nanoparticles weigh relatively little compared to larger particles that contribute most to mass concentration^{60, 61}. Additionally, adverse health effects from exposure to nanoparticles have been shown to relate to particle number or surface area concentration rather than particle mass concentration³⁸. These health effects may differ substantially depending on the size, morphology, composition (both bulk and surface), and concentration of airborne particles⁶².

Microscopy analysis of particles collected on filter media is one method to distinguish airborne engineered nanomaterials from incidental particles. Alternatively, real-time particle monitoring together with workplace activity logs might be used to distinguish

engineered nanoparticles from incidental particles by size. Activity-based monitoring has been used in occupational settings to identify exposure to respirable mass concentrations⁶³ but not to number or surface area concentrations³⁸. In this work, two complementary methods are used to distinguish airborne engineered nanomaterials from incidental particles in a facility that produces nano-structured lithium titanate metal oxide powder. The first method uses off-line analysis of filter samples by SEM and TEM/EDX to identify various particle size, morphology, and composition. The second method relies on activity-based aerosol monitoring as a lower cost alternative to filter-based sampling. The assessment of airborne nanoparticle exposure risk can support development of informed protective standards for the rapidly expanding field of nanotechnology.

5.2 Methods

5.2.1 Manufacturing Facility Full details of the facility and methods used in this work can be found in Peters et al.⁶⁴ The manufacturing facility produces lithium titanate metal oxide nanomaterial for high surface area and superior performance in fuel cells, but the detailed process of making this particular powder is proprietary, and the order of the steps cannot be disclosed. The material was produced in six primary work areas (Figure 5.1): wet mill; spray dryer; rotary calciner; an open area with a powder sifting hood and a stationary calciner; an area with new equipment installation; and a loading dock. In the rotary calciner area workers dumped material every 30 min from a bucket into a hopper that was located at one end of the rotary calciner. They also had to change nanomaterial collection bags at the opposite end of the rotary calciner approximately every 4 hrs. During sample collection and monitoring, employees performed various welding and grinding operations to install new equipment and occasionally used a propane-powered

forklift to move pallets. The doors on the loading dock were typically open, allowing circulation of outside air.

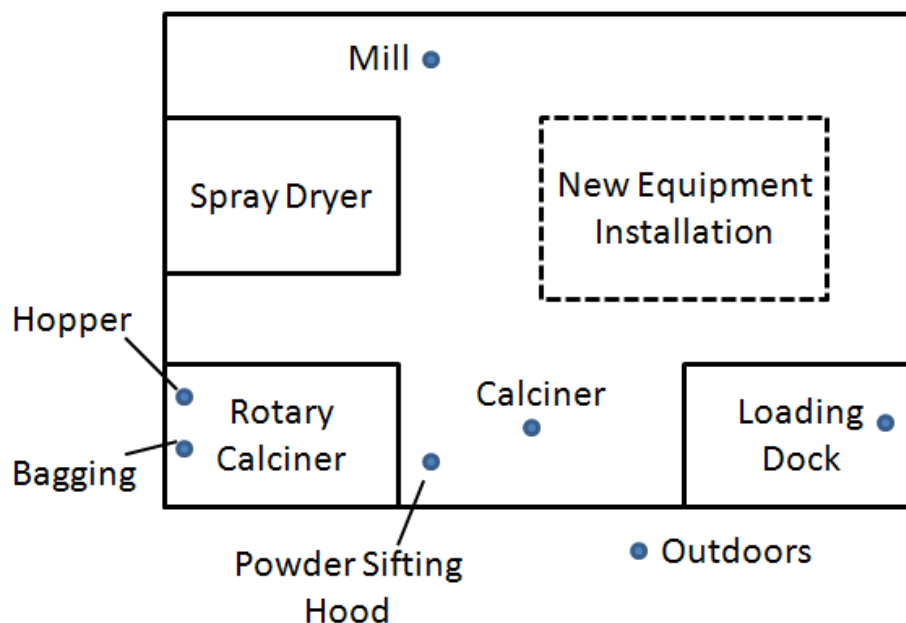


Figure 5.1 Facility layout showing sampling locations (filled dots).

5.2.2 Off-Line Filter Based Analysis Seven locations were selected for collection of respirable samples: the bagging end of the rotary calciner; the hopper end of the rotary calciner; mill; powder sifting hood; calciner, loading dock, and outside of the facility. The spray dryer area was not selected because it was non-operational at that time. Samples were collected on consecutive days using respirable cyclones for gravimetric analysis and electron microscopy. Occupational and Environmental Health researchers in

the laboratory of Dr. Thomas Peters at The University of Iowa collected the samples and conducted gravimetric analysis.

Filters were analyzed by inductively coupled argon plasma atomic emission spectroscopy (ICP-AES) for titanium and lithium to determine the percentage of the respirable mass concentration composed of lithium titanate. For microscopy analysis, filters were digested to deposit the particles on TEM grids according to Burdett and Rood⁴⁹. TEM images were used to classify particles by shape and determine PSD, surface morphology (SEM), and chemical composition (TEM/EDX) for each shape class.

5.2.3 Real Time Activity Based Monitoring Particle number and mass concentrations over time were correlated with worker activities (filling a hopper and changing a collection bag) near a rotary calciner. Airborne concentrations were obtained using two direct-reading instruments, a condensation particle counter and an optical particle counter, for compact size and battery operation. Instruments like a scanning mobility particle sizer would have provided better size resolution but are expensive and not easily transportable. The combined particle size range of particle counter instruments was 10 nm to 20 μm and spanned the range of expected particle sizes. Details of the calculations and statistical analysis used to quantify respirable mass concentrations and percent lithium titanate can be found in Peters et al.⁶⁴

5.3 Results

5.3.1 Off-Line Filter Based Analysis Gravimetric analysis is summarized in Table 5.1 for respirable mass concentration and bulk composition measured throughout the facility. Respirable mass concentrations were greater at the bagging end of the rotary calciner than at the other locations within the facility. Outside the facility, all respirable mass

concentrations were lower than the limit of detection (LOD). At the bagging end of the rotary calciner, the mass concentration of lithium titanate was 39 +/- 11% of the respirable mass concentration. The percentage respirable mass concentration attributed to lithium titanate was 10% at the hopper end of the rotary calciner and 4% at the powder sifting hood.

TEM analysis of samples collected at the bagging end of the rotary calciner revealed distinct particle morphologies (Figure 5.2a and 5.2b): 1) large 200-nm to 10- μ m spheres; 2) irregularly shaped particles of varying size; and 3) submicron particle chains. Analysis with SEM revealed the spheres were composed of clusters of fused 10-80 nm nanoparticles (Figure 5.2c and 5.2d). The irregularly shaped particles had amorphous morphology (Figure 5.2e), while the smaller particle chains were either irregular clumps or chains of spherical 5-50 nm nodules (Figure 5.2f). Titanium was present in all the spherical nanostructured aggregates (Figure 5.3b) but was not present in the chain agglomerates (Figure 5.4) or the irregularly shaped particles. The chain agglomerates contained Al, Fe, K, Mn, and small amounts of Si (Figure 5.4).

5.3.2 Real Time Activity Based Monitoring Figure 5.5 gives results from one of five activity-based monitoring events. Worker activities in the rotary calciner room (loading a hopper and replacing collection bags) were unrelated to the very fine particle number concentrations (Figure 5.5a), but coincided with respirable and total mass concentrations (Figure 5.5b). Similar results were obtained for the other four activity-based monitoring events.

Table 5.1 Respirable Mass Concentration and Percent of Respirable Mass Concentration Lithium Titanate by Location (Results acquired and analyzed by Dr. Thomas Peters, Ronald Johnson, and Dr. Patrick O'shaughnessy at The University of Iowa.) (Peters, T. M.; Elzey, S.; Johnson, R.; Park, H.; Grassian, V. H.; Maher, T.; O'Shaughnessy, P. *Journal of Occupational and Environmental Hygiene* 2009, 6, (2), 73-81.)

Area / Location	Respirable Mass Concentration, mg m ⁻³ Mean ± Std. Dev.	Percent Lithium Titanate
Rotary Calciner / Bagging	0.118 ± 0.023 *	39% ± 11%
Rotary Calciner / Hopper	0.035 ± 0.006	<10% **
Spray Dryer ***	--	--
Wet Mill	0.026 ± 0.007	<LOD
Powder Sifting Hood	0.039 ± 0.016	<4% **
Loading Dock	0.036 ± 0.015	<LOD
Calciner	0.028 ± 0.012	<LOD
Outdoors	<LOD	<LOD

* Duncan multiple range test identified mean as statistically different from other means.

** One or more sample below LOD for titanium; value reported based on sample(s)

>LOD.

*** No samples available because spray dryer was not operational.

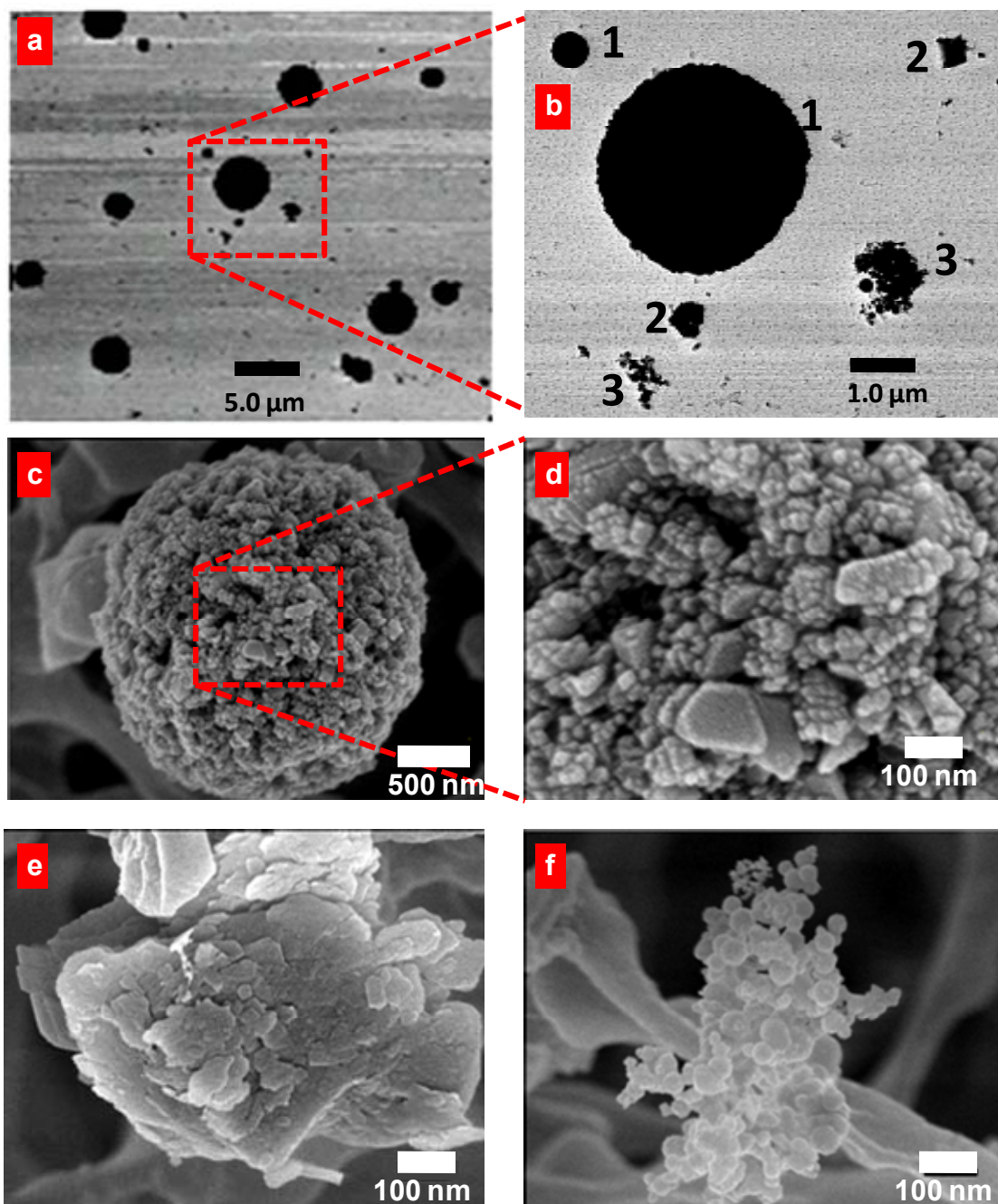


Figure 5.2 Electron microscopy images from filter samples depict particle size and morphology. a,b, TEM images show three types of particles of different shape and size: large spherically shaped particles (b,1); irregularly shaped particles (b,2); and smaller particle chains (b,3). c-e, SEM images reveal that the larger spherical particles are actually composed of smaller nanoparticles 10-80 nm in size interwoven into larger aggregates (c,d); irregularly shaped particles have an amorphous structure (e); and chain agglomerates are composed of spherical nodules of 5-50 nm in size.

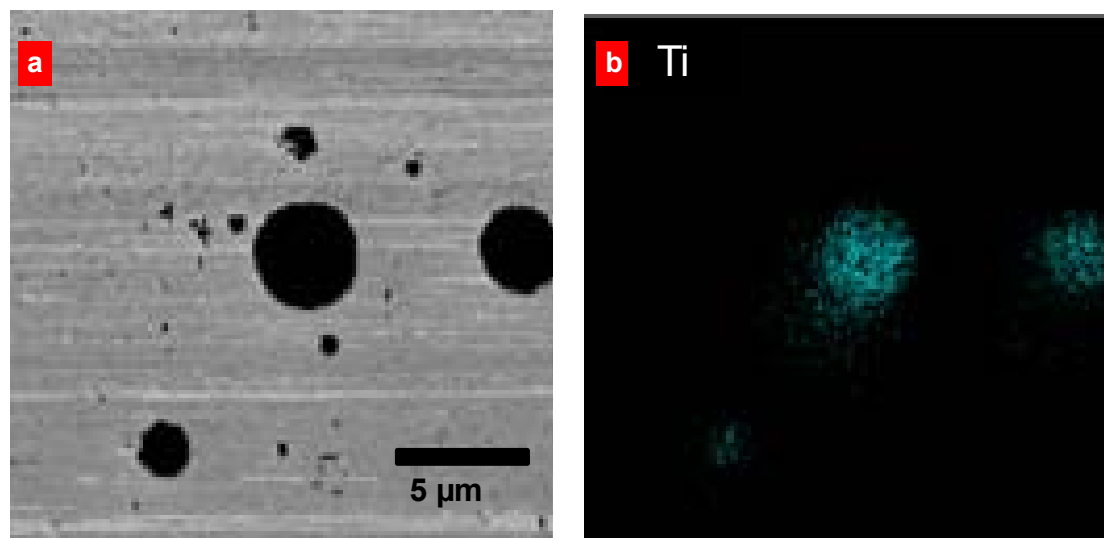


Figure 5.3 Titanium content of a group of particles. a, TEM image. b, corresponding elemental map for titanium. X-rays characteristic of an element, in this case titanium, are emitted upon electron excitation as the microscope's electron beam rasters the sample. The elemental map indicates the relative count rate of characteristic x-rays released at each point on the sample. Lithium cannot be detected with EDX due to its low-energy x-rays that cannot pass through the detector's protective beryllium window. Therefore, the nanomaterial produced in this facility was identified by the presence of titanium, which was only found in the spherical agglomerates.

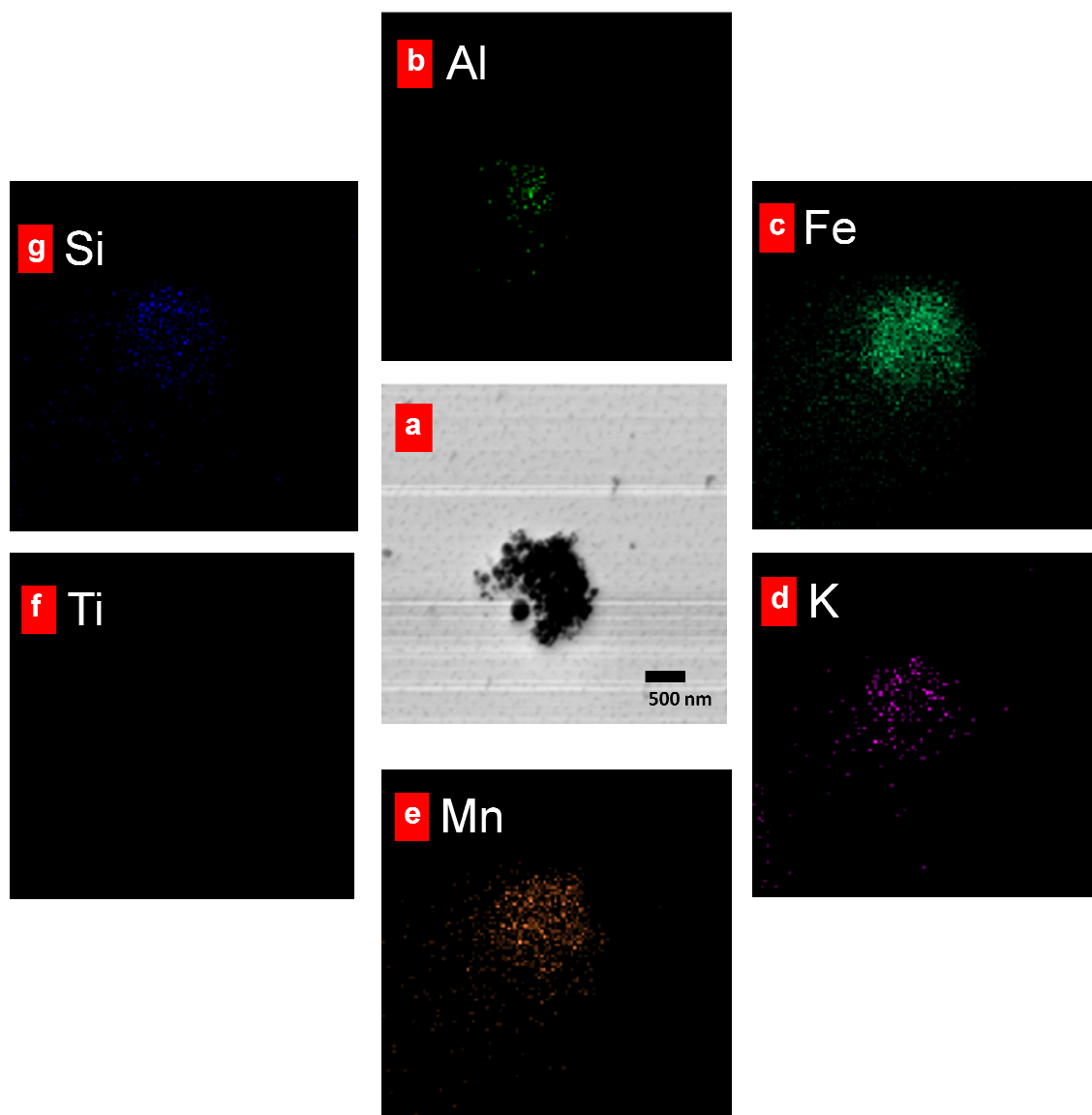


Figure 5.4 Chemical composition of a chain agglomerate particle. a, TEM image. b-g, corresponding elemental maps for several elements show that the chain agglomerates do not contain titanium but do contain elements common to welding fume (e.g. Mn).

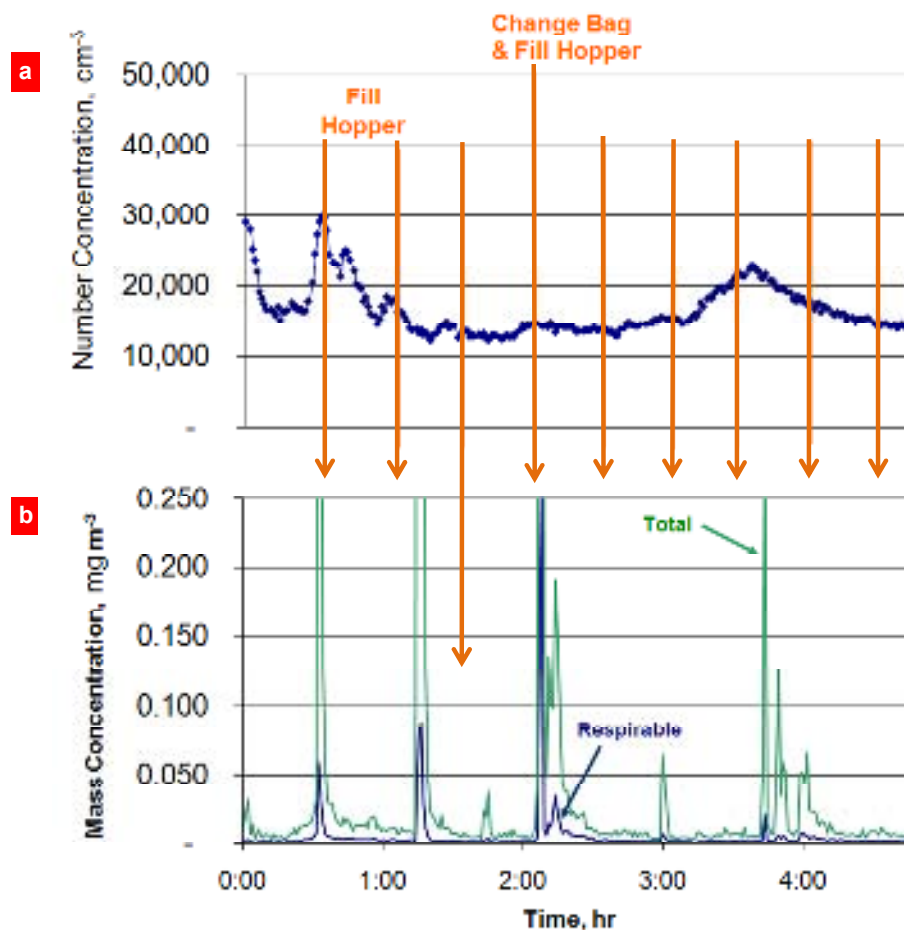


Figure 5.5 Sample results from real-time, activity-based monitoring. Worker production activities are identified with arrows and labeled at the top of the figure. a, very fine particle number concentrations were not related to worker activities indicating the presence of other sources of small particles within the facility. b, respirable and total mass concentrations were strongly related to changing a nanomaterial collection bag and filling the hopper. (Collected by Dr. Thomas Peters, Ronald Johnson, and Dr. Patrick O'shaughnessy at The University of Iowa.) (Peters, T. M.; Elzey, S.; Johnson, R.; Park, H.; Grassian, V. H.; Maher, T.; O'Shaughnessy, P. *Journal of Occupational and Environmental Hygiene* **2009**, 6, (2), 73-81.)

5.4 Discussion

Two methods were used to distinguish airborne engineered nanomaterials from incidental particles in an occupational setting. In the first method using off-line analysis of particles collected onto filters, the greatest respirable mass concentrations with a large percentage of nanomaterial were identified in an area with extensive nanomaterial handling. Thus, this area was identified as having the greatest potential for airborne nanomaterial exposure. Analysis of filter samples collected in this area by TEM and SEM showed only spherical aggregates larger than 200 nm contained titanium and were thus positively identified as engineered and distinct from the other particle types that were incidental to production. The presence of elements such as Mn in particles with chain agglomerate morphology suggests that these particles were fume from welding. The irregularly shaped particles may have come from grinding or possibly from activity outside the facility. A major strength of this microscopy-based method is the ability to evaluate the important particle properties of physical size, morphology, and composition. Detailed data of these type are critical for designing appropriate toxicity tests relevant to environmental and occupational monitoring.

Results from activity-based monitoring were consistent with those from filter-based sampling. The fact that the number concentrations of very fine particles were unrelated to worker activity suggests the nanoparticles present in the rotary calciner area were incidental to production of the nanomaterial. The finding that respirable and total mass concentrations were related to worker activity suggests the particles associated with nanomaterial production were quite large. Although respirable mass concentration includes all particles that collect on a filter $< 4 \mu\text{m}$, it is dominated by the largest particles

because mass is dependent on particle diameter cubed. From these results, it can be concluded that airborne engineered nanomaterials were larger than nanosize in this area.

The activity-based monitoring provided information about the work environment that was unavailable from microscopy-based analysis: time-series data revealed that handling was the primary source of airborne nanomaterial. Based on this work, the Environmental Health and Safety director for the facility implemented reduced handling of the nanomaterial, increased ventilation, and nearly complete enclosure of the process. The company that owns this facility is engaged in research to evaluate the toxic properties of the lithium titanate nanomaterial produced in this facility.

5.5 Conclusions

In summary, two methods (analysis of filter samples by electron microscopy and activity-based monitoring) can be used to distinguish airborne engineered nanomaterials from incidental particles. In this study, both methods lead to the conclusion, for the process being evaluated, that the production of engineered nanomaterial generated relatively large particles and the nanoparticles observed were not associated with the production. Although time-intensive and costly, microscopic analysis provides detailed compositional and structural information that is critical in the design of environmentally relevant toxicological studies. On the other hand, activity-based monitoring provides information on how particles enter and move through the workplace, which is central to developing strategies to reduce inhalation exposures. Exposure information derived from these methods, combined with appropriate toxicity tests, can ensure that informed standards are implemented that will protect workers employed in the nanotechnology industry.

5.6 Acknowledgements

The collaboration of Altair Nanotechnologies, Inc., is greatly appreciated. Supported by NIH P30 ES05605 and CDC 1K01OH009255-01.

CHAPTER 6

SELECTIVE CATALYTIC REDUCTION OF NO₂ WITH AMMONIA USING NANOCRYSTALLINE NaY AND CuY ZEOLITES

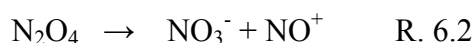
6.1 Introduction

Emissions of NO_x (NO + NO₂) are generated during combustion processes and adversely affect the environment and human health by contributing to ground-level ozone formation, water quality deterioration, global warming, production of toxic reaction products and inhalable fine particles that lead to visibility degradation and pose a respiratory hazard. The primary sources of NO_x emissions include motor vehicles (55%) and industrial, commercial, and residential combustion processes (45%). Current NO_x reduction technology uses catalysts to convert NO_x to environmentally benign products, such as N₂, O₂ and H₂O, during reaction with a reductant through the process of selective catalytic reduction (SCR). NO_x emissions remain in excess of Environmental Protection Agency (EPA) emission limits, and catalysts that improve NO_x reduction are necessary to tackle this problem.

Metal oxides have commonly been used as catalysts for SCR of NO_x, but zeolites have been shown to have superior activity due to their ability to achieve higher NO_x conversions at lower temperatures⁶⁵. Zeolites are crystalline aluminosilicates, consisting of regularly occurring internal pores of molecular dimensions, and a framework of linked cages or channels. The porous nature of zeolites has led to a wide variety of applications based on adsorption/desorption, ion-exchange, and catalysis. Many studies have focused on ZSM-5 zeolites for deNO_x applications, but, despite the superior activity of ZSM-5 zeolites, results have shown problematic deactivation occurs under typical combustion conditions where water and oxygen are present⁶⁶. Zeolite Y has a different channel

structure that could provide unique SCR pathways and may offer a more practical choice of catalyst for post-combustion NO_x treatment. Zeolite Y has a three-dimensional pore structure consisting of sodalite cages with a 7.4 Å diameter assembled to form larger supercages with a 1.2 nm diameter⁶⁷. The framework carries a net negative charge, and charge-compensating metal cations can reside within the interior of the framework and on the exterior as extra-framework cations.

Metal cations associated with the zeolite framework are loosely bound and can be easily exchanged. Such cation exchange can influence the activity of zeolites, and the effect of transition metal cation exchange on the activity of zeolite Y for SCR of NO_x has been thoroughly studied⁶⁸⁻⁷⁰. Polyvalent cations were shown to enhance activity compared with monovalent cations, and copper cation exchange resulted in the highest activity. Sachtler et al. suggested that the multipositive charge of polyvalent cations can dissipate due to dissociative adsorbates such as H₂O and N₂O₄, allowing the cation to migrate toward localized negative charges, thus lowering the energy of the system⁷¹. Such energetically favorable dissociation could improve the activity of CuY for SCR of NO₂, as NO₂ is known to form dimers that dissociate during adsorption on zeolite Y as



Due to the increased activity of copper-exchanged zeolites, and the larger copper ion exchange capacity of zeolite Y compared with other zeolites, several studies have investigated the copper cation interaction with the zeolite Y framework^{70, 72-76}. Selyama et al. identified sites occupied by Cu(II) cations within the framework of zeolite Y and determined that there were five unique sites of Cu(II) cations within the sodalite and

supercage of zeolite Y. The sodalite cage sites were much more densely populated than the supercage sites, but adsorbed water and ammonia can coordinate with the copper cations and cause migration from the sodalite cages to the supercage. Such migration upon water or ammonia adsorption and enhanced mobility of copper ions in CuY has also been reported by others^{70, 73, 74}. The catalytic activity of CuY for SCR of NO_x has shown a unique temperature dependence with maximum activity occurring at 393 K. The coordination of ammonia with Cu(II) to form a [Cu(NH₃)₄]²⁺ complex, accompanied by migration to the supercage, was suggested to be the cause of the unusual temperature dependency⁷⁰. At increased temperatures, ammonia molecules desorb, causing migration back to the sodalite cages and a decrease in activity. In contrast to studies suggesting SCR occurs in the presence of coordinated Cu(II), a kinetic study of NH₃-SCR of NO over CuY suggested a three step mechanism based on an Eley-Rideal interaction where one ammonia molecule is initially bound to Cu(I)⁷⁷. In this mechanism, Cu(I) is oxidized to Cu(II)N_xO_y by oxygen then by NO, and the ammonia reacts with the N_xO_y on the same cation to produce N₂ and H₂O and regenerate the initial NH₃Cu(I).

In addition to the effect of metal cation exchange on deNO_x performance, the effect of particle size of zeolites as catalysts for deNO_x applications has recently been considered^{71, 78, 79}. Commercial zeolites have particle sizes ranging from several hundred nanometers to over a micron. Nanocrystalline zeolites with particle sizes less than one hundred nanometers have been synthesized and possess unique properties compared with commercial zeolites, including greater total and external surface area, a larger percentage of total surface area as external surface area, decreased diffusion pathlengths, and an increased concentration of reactive sites⁷⁸.

Most relevant to the work in this paper are previous studies comparing nanocrystalline NaY with commercial Aldrich NaY for propylene-SCR of NO₂ and urea-SCR of NO₂^{71, 79}. Nanocrystalline NaY zeolite with a particle size of 23 nm was shown to be superior to Aldrich NaY with a particle size of over 500 nm for both propylene-SCR and urea-SCR of NO₂ due to faster reaction rates and decreased formation of undesirable products. The superior performance of the smaller particle sized nanocrystalline NaY was attributed to increased external surface area, silanol groups found in greater concentration on nanocrystalline zeolites, and extra framework alumina (EFAL) sites with Bronsted and Lewis acidity identified on the external surface of the nanocrystalline NaY.

The mechanisms, thermodynamic dependencies and kinetics of the reactions involved in NH₃-SCR of NO_x using commercial zeolites have been investigated in a number of studies⁸⁰⁻⁸⁶. In this study, Aldrich NaY, nanocrystalline NaY and nanocrystalline CuY were evaluated for NH₃-SCR of NO₂. A comparison of surface species before and after SCR, as well as intermediates and product formation, for Aldrich NaY, nanocrystalline NaY, and nanocrystalline CuY is presented. Results for reaction rates and temperature studies are also discussed.

6.2 Experimental Methods

6.2.1 Synthesis and Copper Exchange of Nanocrystalline NaY The synthesis of nanocrystalline NaY has been described previously^{67, 87}. The original synthesis gel composition for zeolite Y was:



where TMAOH is tetramethylammonium hydroxide. Aluminumisopropoxide and tetraethylorthosilicate (TEOS) were used as aluminum and silicon sources, respectively, with isopropanol (*i*-PrOH) and ethanol (EtOH) as their respective hydrolysis products. The synthesis solution for zeolite Y was heated to 363 K in a glass flask containing a magnetic stirrer for 240 h for the first batch, and 72 h for later batches. After each batch, the zeolite crystals were recovered by centrifugation at 14,000 rpm for 30 min. After washing and drying, X-ray powder patterns and BET surface areas of the powders were measured to determine crystal structures and crystal sizes. The NaY was then calcined at 773 K under oxygen flow for 16 hours to remove the TMAOH template. The sodium in nanocrystalline NaY was exchanged with copper ions using the vapor phase exchange method⁸⁷. Approximately 250 mg of synthesized, calcined nanocrystalline NaY and 25 mg of dry copper(I) chloride were ground together using a mortar and pestle. The solid mixture was placed in a glass tube and evacuated for 3 hours at room temperature and then heated under vacuum at 673 K for 6 hours.

6.2.2 Characterization of Zeolites The synthesized nanocrystalline NaY and CuY, as well as commercial NaY purchased from Aldrich, were characterized as described below.

Characterization of elemental analysis was performed by Anamika Mubayi (laboratory of Dr. Sarah Larsen, The University of Iowa) using a Perkin Elmer Plasma 400 Inductively Coupled Plasma Atomic Emission Spectrometer (ICP/AES) spectrometer was used to determine the Si/Al ratio of the NaY samples. NaY samples were acid digested by dilute HF solution followed by neutralization in NaBO₃. Four standard solutions with known silicon (aluminum, sodium, copper) concentrations were prepared as calibration standards. Exact concentrations of silicon, aluminum, sodium and copper

in the sample solution were obtained by projection from the working curve generated from standard solution data.

SEM samples were prepared by sonicating the calcined zeolite powder in a dilute methanol suspension to break up particle agglomerates. A drop of the suspension was applied to the SEM sample stud, and the methanol was allowed to evaporate at room temperature. The sample was then coated with gold, and SEM images were acquired.

A Siemens D5000 X-ray diffractometer with Cu K α target and nickel filter was used to collect XRD powder patterns for the samples. XRD patterns were collected between 2θ angles of 5 and 35°.

Continuous wave electron paramagnetic resonance (EPR) spectra were acquired using a Bruker EMX61 EPR spectrometer equipped with a PC for spectrometer control and data acquisition. Typical EPR spectral parameters were: X-band frequency = 9.43 GHz, modulation amplitude = 0.5 G and modulation frequency = 100 kHz. The magnetic field and microwave frequency were measured using a Hall probe and a frequency counter, respectively. XRD and EPR analysis was performed by Anamika Mubayi (laboratory of Dr. Sarah Larsen, The University of Iowa).

To determine specific surface area, nitrogen adsorption isotherms were collected using a Quantachrome Nova 4200e multipoint BET apparatus. Approximately 0.1-0.2 g of each sample was used for the measurements. Samples were heated at 533 K and degassed overnight prior to nitrogen adsorption. The specific surface area of each sample was then measured. BET adsorption isotherms were collected for nanocrystalline NaY samples before and after calcination to remove the template.

6.2.3 FTIR Experiments Details of the methods used in FTIR experiments were discussed in Section 3.4.3. Briefly, zeolite samples were coated on one half of a tungsten grid, and a thermocouple wire was attached to the tungsten grid to allow resistive heating. The sample holder was placed in a stainless steel reaction chamber equipped with a linear translator to allow either the gas phase or the zeolite sample to be placed in the path of the FTIR beam. The reaction chamber was connected to a power supply and vacuum/gas handling system. Further details of the FTIR experimental system have been described previously⁸⁸.

WinFirst software was used to acquire the data, and gas-phase spectra were referenced to the blank grid, and absorbance spectra were referenced to the corresponding gas phase background with the clean zeolite subtracted. Zeolite samples were heated overnight at 600 K under vacuum prior to experiments. The sample was allowed to cool to room temperature before gases were admitted into the reaction chamber. For absorbance spectra of the surface species resulting from adsorption of reactant gases (NO_2 and NH_3), the gas was loaded into the reaction chamber and the pressure was allowed to stabilize to ensure adsorption equilibrium. The gas phase was then pumped out prior to collecting the spectra. For SCR experiments, 1.5 Torr of NO_2 was loaded into the reaction chamber. Upon equilibration of the NO_2 , 1.5 Torr NH_3 was loaded into the reaction chamber, and heat was applied for experiments conducted at elevated temperatures. Time course experiments automatically collected FTIR spectra of the gas phase every 30 seconds for 2 hours. All spectra shown were recorded at 298 K.

Concentrations of species present in the gas phase were obtained by multiplying the integrated absorbance of the characteristic absorption bands by a correlation factor based

on the extinction coefficient of each species. The extinction coefficients were calibrated using the integrated absorbance of the characteristic bands at corresponding pressures measured with an absolute pressure transducer⁷¹. Changes in NO₂ concentration with reaction time were used to determine initial reaction rates for each zeolite sample at various reaction temperatures.

6.3 Results

6.3.1 Characterization of Zeolites SEM images of nanocrystalline NaY and Aldrich NaY are shown in Figure 6.1. The image of Aldrich NaY (Figure 6.1b) shows large crystals and a wide range of particle sizes, with diameters of ~ 0.5-1.5 μm , and an average particle diameter estimated to be ~ 1 μm . The image of nanocrystalline NaY (Figure 6.1a) shows uniform particles with a narrow size range and an average diameter of approximately 38 nm. The particle size, surface area and catalyst composition for the three zeolite samples are given in Table 6.1.

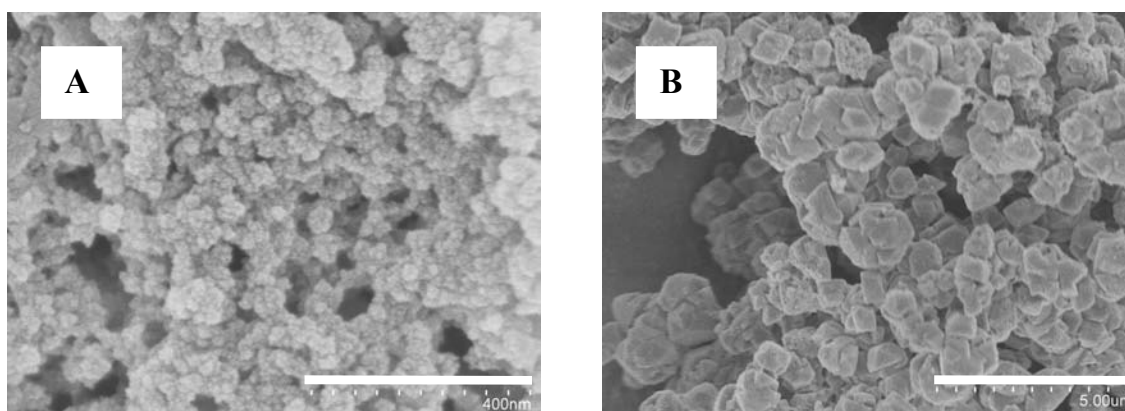


Figure 6.1 SEM images of NaY: (A) nanocrystalline NaY (scale bar = 400 nm) and (B) Aldrich NaY (scale bar = 5 μm).

The total specific surface area of calcined NaY was measured using nitrogen adsorption and the BET method. The external surface area was determined using the BET method for as-synthesized zeolites, which still have template blocking the pores and was used to calculate crystal size⁸⁹. Two different batches of nanocrystalline NaY were used in this study but the crystal sizes were similar, 38 nm and 34 nm, as determined from the external surface area. The external surface areas of the nanocrystalline NaY samples were >100 m²/g, representing ~20% of the total surface area.

The samples were characterized by powder X-ray diffraction (XRD) and electron paramagnetic resonance (EPR) spectroscopy. XRD powder patterns of the NaY samples (Figure 6.2) were obtained before and after vapor phase exchange. Broadening of the XRD pattern is observed for nanocrystalline NaY relative to Aldrich NaY, and this is due to line broadening that occurs as the crystal size becomes very small as expected. The crystal structure is intact after the vapor phase exchange as indicated by the XRD pattern in Figure 6 2c.

Table 6.1 Properties of Synthesized Nanocrystalline NaY and CuY and Aldrich NaY

Zeolite Catalyst	Particle Size (nm)	Specific Surface Area (m ² /g)	Si/Al	Cu/Al
		Total / External		
Aldrich NaY	~1000 nm	615 / <1 ^a	1.8	----
Nano-NaY	38 nm ^b	523 / 106	1.8	----
Nano-CuY	34 nm ^b	538 / 118	1.8	0.3

^a Estimated based on geometric considerations.

^b Determined from BET external surface area measurements, as in Song, W.; Grassian, V. H.; Larsen, S. C. *Chemical Communications* **2005**, 23, 2951.

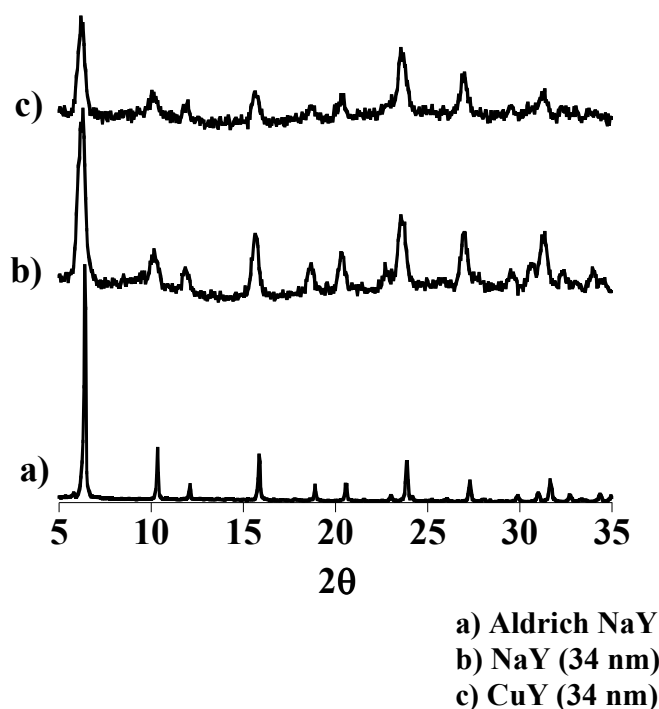


Figure 6.2 XRD patterns of synthesized nanocrystalline NaY and CuY and Aldrich NaY. (Acquired by Anamika Mubayi in the laboratory of Dr. Sarah Larsen at The University of Iowa) (Elzey, S.; Mubayi, A.; Larsen, S. C.; Grassian, V. H. *Journal of Molecular Catalysis A: Chemical* **2008**, 285, (1-2), 48-57.)

The EPR spectrum was obtained for nanocrystalline CuY at 77 K and is shown in Figure 6.3. Cu(II) has a d^9 electronic configuration with $S=1/2$ and $I=3/2$. The EPR spectrum of nanocrystalline CuY has the same general features as hydrated, octahedral $[\text{Cu}(\text{H}_2\text{O})_6]^{2+}$ or $[\text{Cu}(\text{H}_2\text{O})_5\text{OH}]^+$ complexes, but the spectral broadening makes it difficult to quantitatively determine the EPR parameters through simulation or fitting routines^{90, 91}. The spectral broadening is attributed to the heterogeneity of the copper sites in the nanocrystalline CuY.

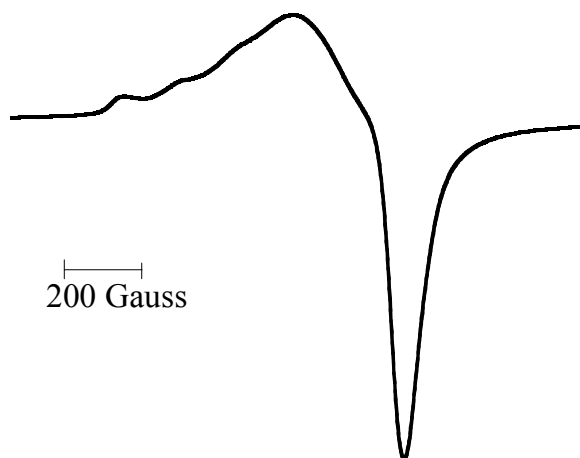


Figure 6.3 EPR spectrum of nanocrystalline CuY recorded at 77 K. (Acquired by Anamika Mubayi in the laboratory of Dr. Sarah Larsen at The University of Iowa). (Elzey, S.; Mubayi, A.; Larsen, S. C.; Grassian, V. H., FTIR study of the selective catalytic reduction of NO₂ with ammonia on nanocrystalline NaY and CuY. *Journal of Molecular Catalysis A: Chemical* **2008**, 285, (1-2), 48-57.)

6.3.2 Adsorption of NO₂ at T = 298 K The FTIR spectra of Aldrich NaY, nanocrystalline NaY and nanocrystalline CuY with adsorbed NO₂ are shown in Figure 6.4. The assignment of absorbance bands resulting from NO₂ adsorption on all three zeolites is summarized in Table 6.2. Absorbance bands appear at 1212, 1308, 1395, and 2180 cm⁻¹ upon NO₂ adsorption on Aldrich NaY. The assignment of these bands is based on comparison with previous literature^{71, 80, 81, 83}. The band at 1212 cm⁻¹ is due to nitrite adsorbed on sodium cationic sites, and the band at 1395 cm⁻¹ and its shoulder at 1308 cm⁻¹ are due to nitrate adsorbed on sodium cationic sites. The two nitrate bands result from splitting of the asymmetric stretching vibration and merge into one band at higher NO₂ loadings as the bands broaden due to intermolecular interactions⁸⁸. The band at 2180 cm⁻¹ resulted from the formation of [NO⁺][NO₂] adducts on Lewis base sites⁷⁹.

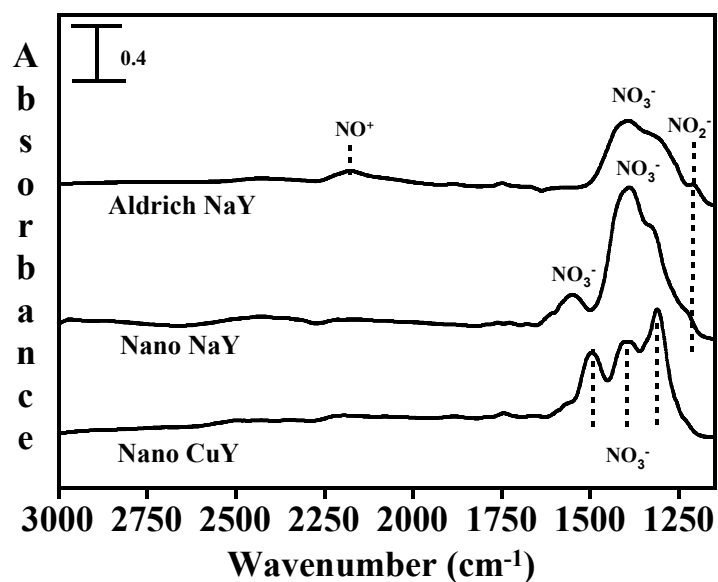


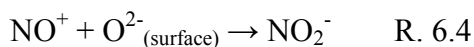
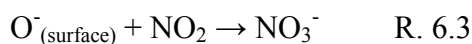
Figure 6.4 FTIR spectra of NO_2 adsorbed on Aldrich NaY, nanocrystalline NaY and nanocrystalline CuY at $T = 298$ K. A pressure of 1.5 Torr NO_2 was allowed to equilibrate, and the gas phase was pumped out prior to collecting each spectrum. The blank grid was used as a reference, and the corresponding clean zeolite spectrum prior to NO_2 adsorption has been subtracted.

Table 6.2 Assignment of Absorbance Bands Resulting from NO₂ Adsorption on Commercial NaY, Nanocrystalline NaY and Nanocrystalline CuY

Catalyst	Frequency (cm ⁻¹)	Assignment of Adsorbed Species	Reference
Aldrich NaY	1212	v(NO ₂ ⁻) of NO ₂ ⁻ ads on Na ⁺	87
	1308, 1395	v(NO ₃ ⁻) of NO ₃ ⁻ ads on Na ⁺	
	2180	v(NO ⁺) of [NO ⁺][NO ₂] on Na ⁺	
Nano NaY	1226	v(NO ₂ ⁻) of NO ₂ ⁻ ads on Na ⁺	70
	1326, 1394	v(NO ₃ ⁻) of NO ₃ ⁻ ads on Na ⁺	
	1555	v(NO ₃ ⁻) of NO ₃ ⁻ on EFAL	
Nano CuY	1313, 1397, 1498	v(NO ₃ ⁻) of NO ₃ ⁻ ads on Cu ²⁺	92

Absorption bands on nanocrystalline NaY following exposure to NO₂ appear at 1226, 1326, 1394, and 1555 cm⁻¹. These bands are easily assigned based on previous studies of urea-SCR of NO₂ over nanocrystalline NaY⁷¹. Similar to Aldrich NaY, NO₂ adsorption on nanocrystalline NaY resulted in adsorbed nitrite (1226 cm⁻¹) and nitrate (1326 and 1394 cm⁻¹) on sodium cationic sites. The band at 1555 cm⁻¹ is due to nitrate adsorbed on EFAL sites in a monodentate coordination, and is only observed in the nanocrystalline NaY. The intensity of the nitrate bands in nanocrystalline NaY relative to Aldrich NaY indicates the greater adsorption capacity of nanocrystalline NaY for NO₂. Formation of NO⁺ evidenced by a band at ~2080 cm⁻¹ is weak on nanocrystalline NaY. This is most likely due to increased surface reactive sites in nanocrystalline NaY that allow NO₂ to

adsorb as surface nitrate without the production of NO^+ , or promote the conversion of NO^+ to surface nitrite



Absorbance bands for the nanocrystalline CuY appear at 1313, 1397, and 1498 cm^{-1} . The three bands overlap and fall within the nitrate adsorption range observed for both NaY zeolites. These bands are assigned to nitrate adsorbed on copper cationic sites, and the nature of these surface species will be discussed in detail⁹². A shoulder at higher wavenumber is observed, most likely due to nitrate adsorbed on EFAL sites, as observed in nanocrystalline NaY.

6.3.3 Adsorption of NH_3 at $T = 298 \text{ K}$ FTIR spectra of Aldrich NaY, nanocrystalline NaY and nanocrystalline CuY with adsorbed NH_3 are shown in Figure 6.5. The assignment of absorbance bands resulting from NH_3 adsorption on all three zeolites is summarized in Table 6.3. The presence of NH_3 resulted in absorbance bands due to molecularly adsorbed ammonia and the formation of ammonium ions for all three zeolites. For nanocrystalline NaY, absorbance bands are observed at 1308, 1450, 1580, 3248, 3317 and 3389 cm^{-1} . The broad band at 1308 cm^{-1} is assigned to NH_3 adsorbed on Lewis acid sites, the intense band at 1450 cm^{-1} is assigned to NH_4^+ resulting from ammonia protonation by Bronsted acid sites, and the small peak at 1580 cm^{-1} is assigned to NH_3 adsorbed on EFAL sites⁹³. The band at 3248 cm^{-1} is likely due to ammonia hydrogen bonded to oxygen lone pairs of silicon-oxygen bridging sites^{94, 95}. The bands at 3317 and 3389 cm^{-1} are the symmetric and asymmetric stretches of ammonia adsorbed on surface hydroxyl groups^{80, 94, 95}.

Aldrich NaY showed adsorption bands at 1311 and 1475 cm^{-1} due to NH_3 on Lewis acid sites and NH_4^+ formation, respectively, but these bands were much weaker than those on the nanocrystalline sample. Additionally, there was no band resulting from NH_3 on EFAL sites for the Aldrich NaY. The greater intensity of the bands on the nanocrystalline NaY and the observation of NH_3 on EFAL sites are due to the increased concentration of surface reactive sites present in the nanocrystalline zeolite. The small, sharp band commonly reported by others at $\sim 1620\text{-}1630\text{ cm}^{-1}$ due to NH_3 adsorbed on Lewis acid sites of NaY was not observed on the Aldrich or nanocrystalline NaY samples^{96, 97}. This band could have been dominated by some adsorbed water on both NaY samples.

There were differences in ammonia adsorption between the nanocrystalline samples. Absorbance bands on the nanocrystalline CuY are seen at 1282, 1460, 1623 and 3327 cm^{-1} . The broad band at 1460 cm^{-1} is due to NH_4^+ formation, and the sharper bands at 1282 and 1623 cm^{-1} are assigned to NH_3 coordination with copper cations, resulting in a $[\text{Cu}(\text{NH}_3)_4]^{2+}$ complex⁷². The NH_4^+ band on the nanocrystalline CuY is weaker, and the NH_3 bands are more intense relative to the nanocrystalline NaY. This is due to the fact that ammonia formed strong coordination bonds with the copper cations, leaving fewer NH_3 molecules for protonation and NH_4^+ formation. The band at 3327 cm^{-1} is most likely the symmetric stretch of ammonia adsorbed on surface hydroxyl groups. This band has been observed to shift upon cation exchange⁸⁰.

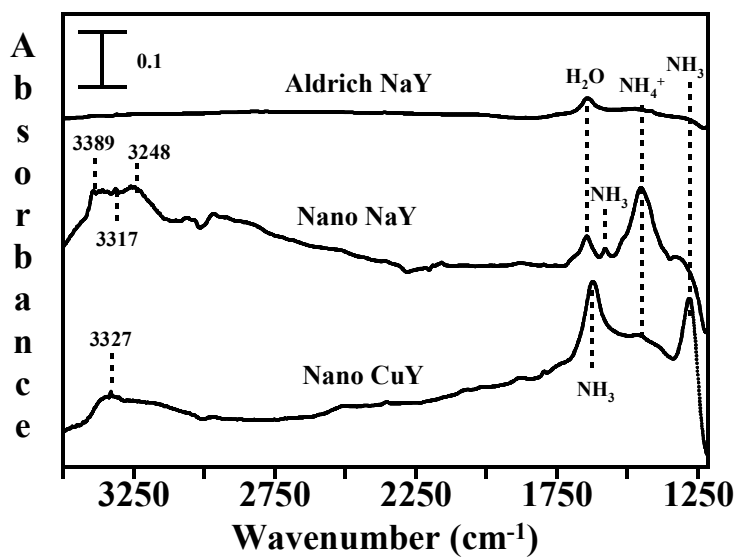


Figure 6.5 FTIR spectra of NH_3 adsorbed on Aldrich NaY, nanocrystalline NaY and nanocrystalline CuY at $T = 298$ K. The gas phase was pumped out prior to collecting each spectrum. The blank grid was used as a reference, and the corresponding clean zeolite spectrum prior to NH_3 adsorption has been subtracted.

Table.6.3 Assignment of Absorbance Bands Resulting from NH₃ Adsorption on Commercial NaY, Nanocrystalline NaY and Nanocrystalline CuY

Catalyst	Frequency (cm ⁻¹)	Assignment of Adsorbed Species	Reference
	1311	$\delta(\text{NH}_3)$ of NH ₃ on SiOH	
Aldrich NaY	1475	$\delta(\text{NH}_4^+)$ of NH ₄ ⁺ deformation	79, 94, 95
	1641	$\delta(\text{H}_2\text{O})$ of adsorbed H ₂ O	
	1308	$\delta(\text{NH}_3)$ of NH ₃ on SiOH	
	1450	$\delta(\text{NH}_4^+)$ of NH ₄ ⁺ deformation	
	1580	$\delta(\text{NH}_3)$ of NH ₃ on EFAL	93
	1641	$\delta(\text{H}_2\text{O})$ of adsorbed H ₂ O	
Nano NaY	3248	$\nu(\text{NH}_3)$ of NH ₃ on O ²⁻ of SiOH	
	3317	$\nu(\text{NH}_3)$ sym. stretch of NH ₃ on surface OH	79, 94, 95
	3389	$\nu(\text{NH}_3)$ asym. stretch of NH ₃ on surface OH	
	1282	$\delta(\text{NH}_3)$ of NH ₃ in [Cu(NH ₃) ₄] ²⁺	
Nano CuY	1460	$\delta(\text{NH}_4^+)$ of NH ₄ ⁺ deformation	71
	1623	$\delta(\text{NH}_3)$ of NH ₃ in [Cu(NH ₃) ₄] ²⁺	

6.3.4 NH₃-SCR of NO₂ at T = 298 K: Gas Phase A gas phase spectrum was collected prior to running the SCR reaction, with only NO₂ loaded in the reaction chamber. As described earlier, ammonia was added to begin the SCR, and the gas phase was monitored at 30-second intervals for the duration of the reaction. A final gas phase spectrum was collected after two hours of SCR. Results for nanocrystalline CuY before, during, and after SCR are shown in Figure 6.6. The nanocrystalline CuY gas phase spectra are representative of all three zeolite samples, since both NaY zeolites showed similar results to CuY. Prior to SCR, gas phase species present were NO₂, N₂O₄, NO (~1:3 ratio NO:NO₂) and a small amount of N₂O (~1:100 NO:NO₂). After two hours of NH₃-SCR at 298 K the peaks due to NO₂ and N₂O₄ completely disappeared, and small bands due to NO and N₂O still remained. Water was produced, and an ammonium nitrate intermediate was seen in the gas phase due to condensation on the IR cell windows. The absorption bands for ammonium nitrate remained in the IR spectrum after pumping out the gas phase and slowly disappeared with continued evacuation of the IR cell. This indicates ammonium nitrate was condensed on the IR cell windows rather than present in the gas phase. Nitrogen was also produced during SCR according to the overall equation for NH₃-SCR of NO₂



Gas phase NO and N₂O can remain after SCR of NO₂. These species are greenhouse gases, and can either be produced during SCR or be present prior to SCR in the NO₂ gas feed and remain unreacted. The gas phase concentrations of NO and N₂O during NH₃-SCR of NO₂ are shown in Figure 6.7. All three zeolite samples showed similar results for both NO and N₂O in the gas phase. The total concentration of gas phase NO was reduced

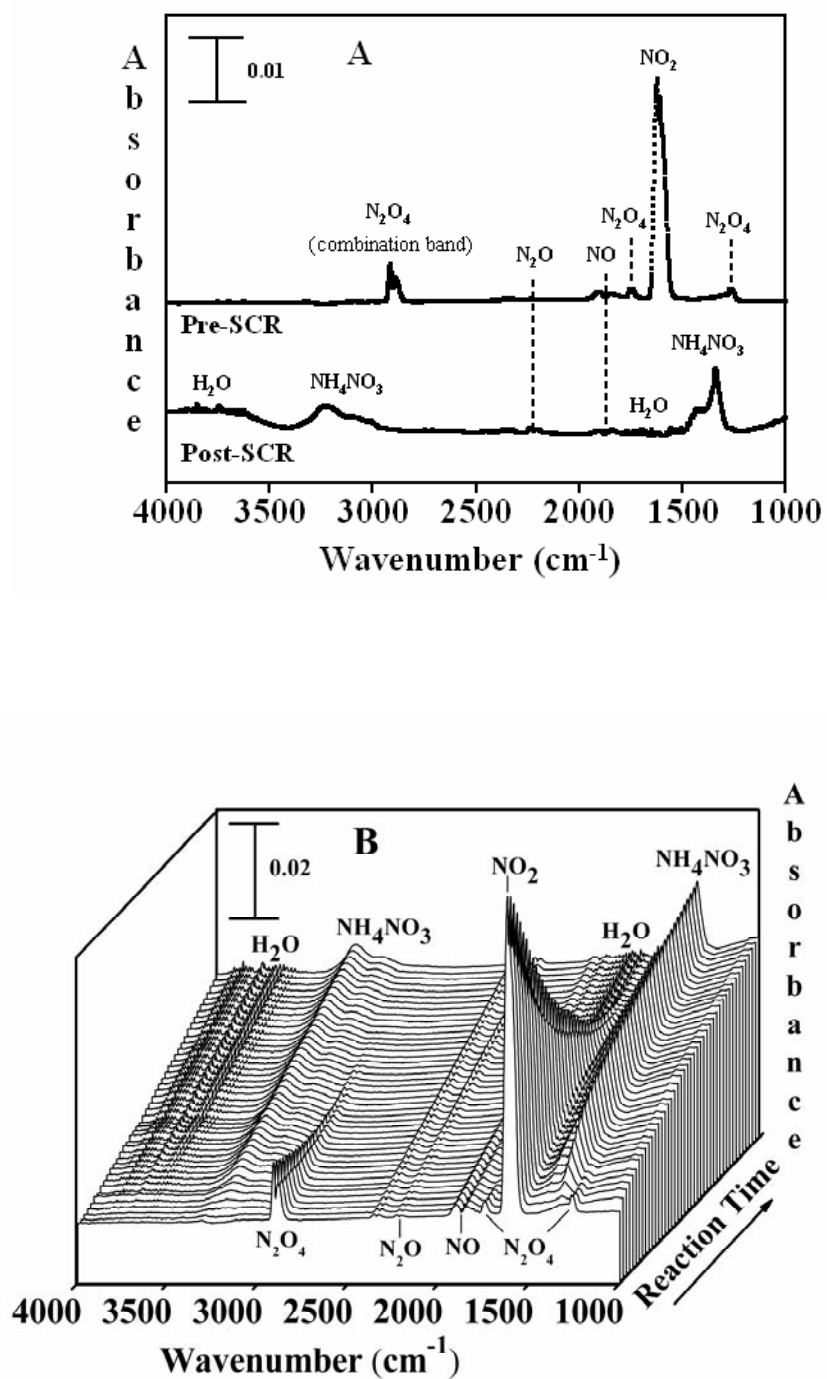


Figure 6.6 FTIR spectra of gas phase species detected (A) pre-SCR and post-SCR over nanocrystalline CuY at $T = 298$ K, and (B) at 30 second intervals for the first 30 minutes during SCR over nanocrystalline CuY at $T = 298$ K. The blank grid was used as a reference.

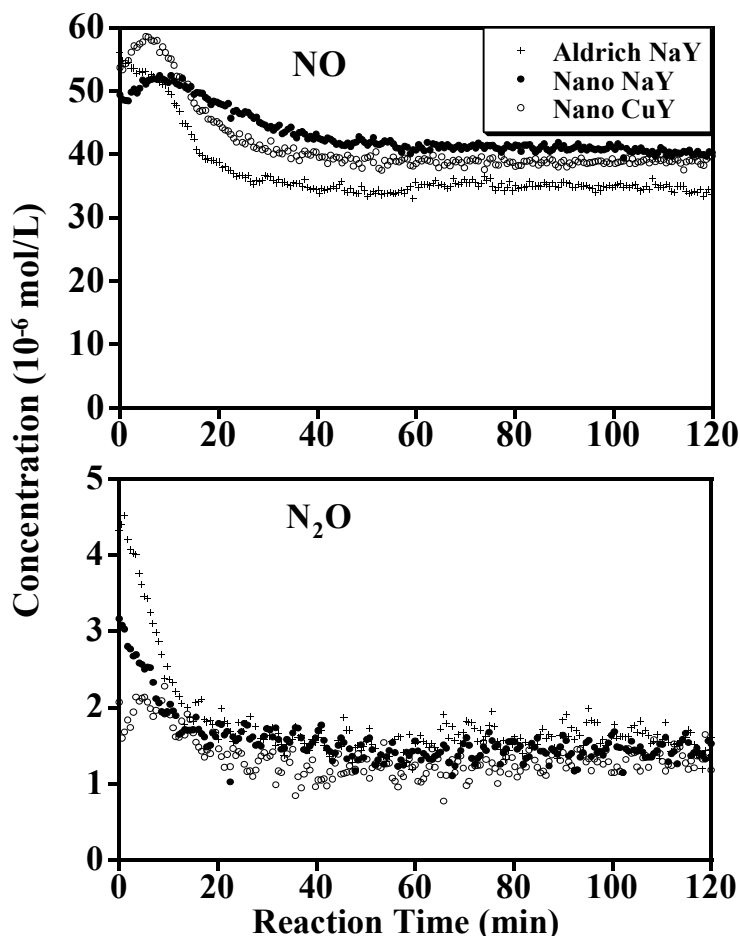


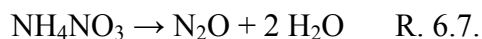
Figure 6.7 Concentrations of gas phase NO (upper) and N₂O (lower) over Aldrich NaY, nanocrystalline NaY and nanocrystalline CuY during NH₃-SCR of NO₂ at T = 298 K.

by ~30-40% during the SCR reaction. It could be expected that under typical lean burn exhaust conditions a greater amount of NO would be oxidized to NO₂ according to



and subsequently reduced during NH₃-SCR of NO₂.

In the presence of oxygen, N₂O can be produced from reactions with ammonia and NO. In the presence or absence of oxygen, N₂O can also be produced from the thermal degradation of ammonium nitrate



The results of this research show no production of N_2O during SCR. There was initially a small concentration of N_2O , which decreased during the course of the reaction.

Although ammonium nitrate was present, degradation producing N_2O did not occur since the ammonium nitrate remained in a condensed state due to the low temperature of the reaction.

6.3.5 NH_3 -SCR of NO_2 at $T = 298 \text{ K}$: Surface Species Prior to SCR, surface species observed on the zeolites were due to NO_2 adsorption only, which has been described previously (Figure 6.4). Results for the surface species detected post-SCR over Aldrich NaY, nanocrystalline NaY and nanocrystalline CuY are shown in Figure 6.8. All three zeolite samples showed NO_3^- remaining on the surface due to adsorption on cationic sites. Aldrich NaY had water remaining on the surface at 1638 cm^{-1} and nitrate at 1410 cm^{-1} . As mentioned earlier, two nitrate bands on NaY have been known to merge at higher NO_2 concentrations. Nitrate is seen as a merging of the two bands on the surface of nanocrystalline NaY post-SCR, with two maxima at 1335 and 1440 cm^{-1} . Nitrate adsorbed on EFAL sites in nanocrystalline NaY was more reactive than nitrate on cationic sites since no nitrate remained on EFAL sites post-SCR. For nanocrystalline CuY post-SCR, NO_3^- is seen as a broad band with a gradual slope increasing toward the right and centered at 1400 cm^{-1} . Comparing the shape and location of this band with the three nitrate bands seen on CuY pre-SCR (Figure 6.4) suggests the nitrate band post-SCR resulted from an overlapping of the three nitrate bands seen pre-SCR, similar to what was observed on the NaY samples. The intensity of the nitrate band on Aldrich NaY is significantly lower than on nanocrystalline NaY, and nanocrystalline CuY has an even

more intense nitrate band. The small peak at 1617 cm^{-1} on nanocrystalline CuY is most likely due to a small amount of adsorbed NH_3 remaining post-SCR⁹⁸.

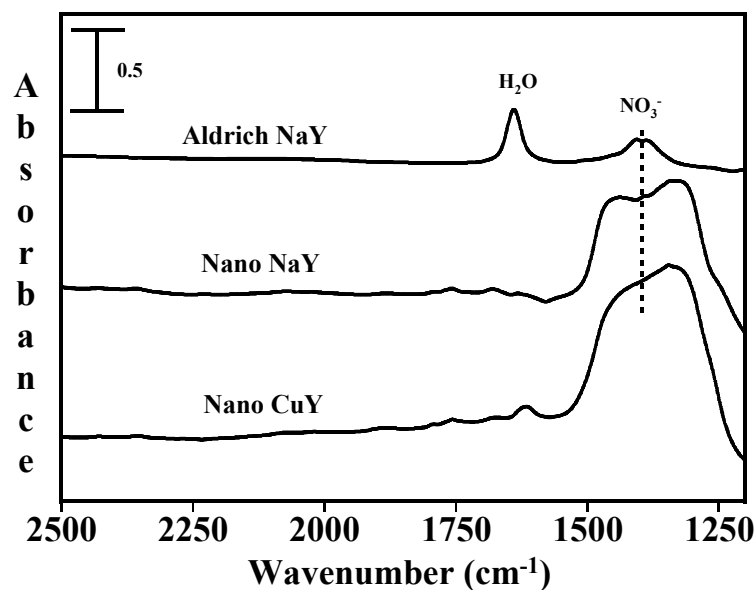


Figure 6.8 FTIR spectra of surface species detected post-SCR over Aldrich NaY, nanocrystalline NaY and nanocrystalline CuY at $T = 298\text{ K}$. The gas phase was pumped out prior to collecting each spectrum, and the blank grid was used as a reference. Corresponding clean zeolite spectra prior to SCR have been subtracted.

6.3.6 Nanocrystalline Zeolites: NaY vs. CuY A primary aim of this work was to compare nanocrystalline zeolites with sodium and copper cations for NH_3 -SCR of NO_2 . It is well known that copper cation exchange improves the performance of commercial zeolites for deNO_x applications, as determined by higher NO_x conversions, faster reaction rates and lower temperatures required for SCR^{65, 67-69}. Not surprisingly, similar results were observed for nanocrystalline zeolites. The concentration of NO_2 present in the gas

phase during SCR over Aldrich NaY, nanocrystalline NaY and nanocrystalline CuY is shown in Figure 6.9. The reaction between ammonia and NO_2 was zero order, as indicated by the linear nature of the time dependent NO_2 concentration, and occurred very quickly over the nanocrystalline zeolites, with greater than 97% conversion achieved in less than 20 minutes. The initial rates of reaction for nanocrystalline NaY and CuY are compared in Table 6.4, with Aldrich NaY used as a reference. Nanocrystalline CuY resulted in an increased reaction rate of 11% compared with nanocrystalline NaY, and 40% compared to Aldrich NaY. The superior performance of nanocrystalline NaY over Aldrich NaY for NH_3 -SCR of NO_2 is attributed to the enhanced properties of nanocrystalline zeolites compared with zeolites of larger particle size previously reported for SCR of NO_2 with propylene and urea as the reductants^{71, 79}. The superior performance of nanocrystalline CuY over nanocrystalline NaY requires an explanation that is independent of the nanocrystalline nature of the zeolite, but instead is specific to the identity of the cation present in the framework. This will be discussed in further detail below.

Temperature studies showed an interesting difference between the two nanocrystalline zeolites. SCR reactions were carried out at 298 K, 373 K, 423 K, and 473 K. Reaction rates for nanocrystalline NaY were independent of temperature, with less than 3% variation in the reaction rate at all four temperatures studied. Nanocrystalline CuY showed an inverse temperature dependence, with an average decrease in reaction rate of nearly 7% for each 50 K rise in temperature. This observation is related solely to the difference in cations, since the Aldrich NaY showed the same temperature dependence as the nanocrystalline NaY.

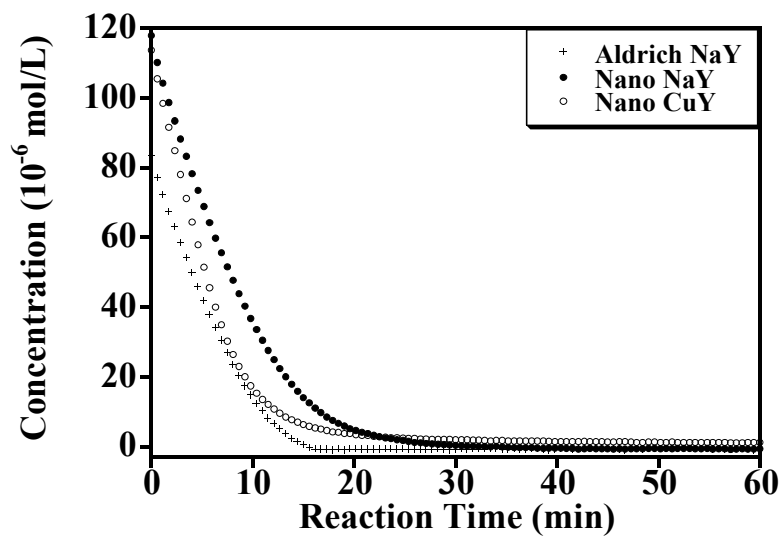


Figure 6.9 Concentration of gas phase NO_2 over Aldrich NaY, nanocrystalline NaY and nanocrystalline CuY during NH_3 -SCR of NO_2 at $T = 298 \text{ K}$.

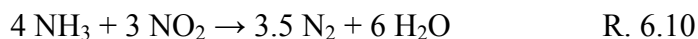
Table 6.4 Comparison of Initial Rates of Reactions for NH_3 -SCR Of NO_2 Over Commercial NaY, Nanocrystalline NaY and Nanocrystalline CuY

Zeolite Catalyst	Initial Rate ($\text{mmol}\cdot\text{L}^{-1}\cdot\text{min}^{-1}\cdot\text{mg}^{-1}$)	% Improvement Over Commercial NaY
Aldrich NaY	0.50	0
Nano NaY	0.70	29
Nano CuY	0.83	40

6.4 Discussion

6.4.1 NH₃-SCR of NO₂: Reactions Between NO₂ and NH₃ Ammonia can react with

NO_x during SCR according to



Typical combustion exhaust conditions contain ~16% water and an excess of oxygen, leading to numerous side reactions, including direct oxidation of ammonia to produce N₂, N₂O, NO₂, or NO, and oxidation of NO to NO₂⁸². The reaction resulting from NH₃ and an equimolar mixture of NO and NO₂ (R. 6.9) is said to be the fast SCR reaction, while mixtures containing greater fractions of NO₂ (R. 6.10) are said to proceed more slowly. Common intermediates in NH₃-SCR of NO_x include ammonium nitrite and ammonium nitrate.

Selective catalytic reduction of NO_x with ammonia is defined by the formation of N₂ as the preferred product. It is widely accepted that the N₂ product contains one nitrogen atom originating from NO_x and one from NH₃^{66, 71, 86}. In this work, the production of N₂ during SCR could be a composite of reactions based on the surface and gas phase species observed. Reactions would then involve adsorbed ammonia (NH₃, NH₄⁺) and/or gas phase NH₃ interacting with adsorbed NO₂ (NO₃⁻, NO₂⁻, NO⁺) and/or gas phase NO₂ (NO₂, N₂O₄, N₂O, NO) (Fig. 6.6). Insight into the probable interactions between NO₂ and NH₃ for the three zeolites can be gained by considering the surface species formed upon adsorption of the reactants on each zeolite.

All three zeolites showed similar major surface species upon adsorption of both NO₂

and NH_3 , but the reactive sites where adsorption occurred were different. The major surface species formed from NO_2 adsorption on Aldrich NaY was NO_3^- adsorbed on Na^+ sites. Minor surface species included NO_2^- and NO^+ on Na^+ sites. Ammonia resulted in a small amount of NH_3 adsorbed on silanol groups only. From the analysis of surface species formed upon reactant adsorption it is determined that SCR reactions between NO_2 and NH_3 over Aldrich NaY occurred primarily between nitrate on sodium cationic sites and NH_3 on silanol groups.

Similar to Aldrich NaY, the major surface species formed from NO_2 adsorption on nanocrystalline NaY was NO_3^- on Na^+ sites, and a minor surface species was NO_2^- on Na^+ sites. Unique to nanocrystalline NaY was NO_3^- adsorbed on EFAL sites as well. Nitrate adsorbed on EFAL sites was more reactive than nitrate on Na^+ sites since only nitrate on the Na^+ remained on the surface post-SCR. Also unique to nanocrystalline NaY was NH_3 adsorbed on EFAL sites in addition to NH_3 adsorbed on silanol groups. This indicates that SCR reactions between NO_2 and NH_3 over nanocrystalline NaY involved nitrate on sodium cationic sites *and* EFAL sites reacting with NH_3 on silanol groups *and* EFAL sites.

Adsorption of NO_2 and NH_3 on nanocrystalline CuY resulted in the same major surface species of NO_3^- and NH_3 , respectively. An interesting difference was that all the surface species identified on nanocrystalline CuY for both NO_2 and NH_3 were adsorbed on copper cationic sites. A small amount of NO_2 was also suggested to result from adsorption on EFAL sites. Therefore, SCR reactions between NO_2 and NH_3 over nanocrystalline CuY were determined to have occurred between nitrate on copper cationic sites and EFAL sites and NH_3 on copper cationic sites. This result suggests that

copper cation exchange not only resulted in faster NH_3 -SCR of NO_2 , but also indicates the copper cations played a greater role in facilitating the SCR than sodium cations, even dominating the Lewis and Bronsted acid sites primarily involved in SCR over zeolites.

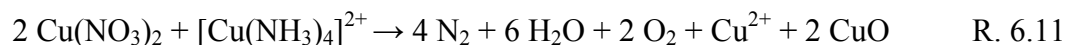
The production of N_2 was initiated by NO_2 dimerization and subsequent dissociation to NO_3^- and NO^+ , together with NO_2 and NO^+ interactions with surface oxygen anions to produce NO_3^- and NO_2^- according to R. 6.3 and R. 6.4. This work indicates that these surface species reacted solely with adsorbed NH_3 rather than gas phase NH_3 , since gas phase NH_3 concentrations remained constant at approximately zero throughout SCR for all three zeolites. In addition to N_2 production, H_2O and NH_4NO_3 were also produced during reactions between NO_2 and NH_3 . The water produced was entirely in the gas phase over both nanocrystalline samples, but water was in the gas phase and on the surface post-SCR over Aldrich NaY. Ammonium nitrate remained condensed on the IR cell windows for all three zeolites, and therefore did not contribute to the formation of undesired gas phase products such as N_2O , NH_3 and HNO_3 that could be produced through thermal decomposition.

6.4.2 Nanocrystalline CuY: Cationic Interactions To understand the enhancement resulting from the copper cation exchange it is necessary to consider how the nitrate and ammonia molecules interacted with cationic reactive sites of nanocrystalline CuY. The nature of nitrate interactions with metals was studied by Gatehouse et al. using IR spectroscopy⁹². The results showed that an ionic interaction between the NO_3^- ion and a metal cation could be distinguished from a coordinated nitrate complex based on the frequencies of the vibrational modes. The adsorption of NO_2 on nanocrystalline CuY resulted in three absorbance bands due to nitrate adsorption on copper sites (Figure 6.2).

The central band at 1390 cm^{-1} was assigned to the ν_3 mode of the NO_3^- ion in an ionic interaction with copper cations. Ionic interactions involving nitrate likely resulted from NO_3^- formed through the sequence in R. 6.1 and R. 6.2. The bands at 1313 and 1498 cm^{-1} resulted from the covalent interaction of nitrate bonded to copper through one oxygen atom and were assigned to the symmetric and asymmetric stretches (ν_1 and ν_4) of ONO_2 , respectively. Nitrate adsorption could have resulted from NO_2 adsorption on Cu-O and/or EFAL sites through surface oxygen, according to R. 6.3. Such adsorption is supported by the absence of a NO^+ band and seen as the shoulder to the left of the band at 1498 cm^{-1} . Comparatively, nitrate adsorption on sodium cationic sites for both NaY samples was the result of only ionic interactions. Thus, copper cation exchange introduced new sites for sorption and reaction of NO_2 in nanocrystalline CuY.

As previously mentioned, ammonia adsorption in nanocrystalline CuY resulted in two intense peaks due to the formation of $[\text{Cu}(\text{NH}_3)_4]^{2+}$. According to Flentge et al. NH_3 bonds in a square planar geometry in this complex and always in a 4:1 ratio for $\text{NH}_3:\text{Cu}^{98}$. It is likely the majority of the copper cations were initially in sodalite cages and migrated into the supercages upon coordination with ammonia molecules^{70, 73, 74, 98}.

Based on what has been discussed so far, an overall SCR reaction can be proposed that involves the exchanged copper cations in nanocrystalline CuY:



This reaction suggests 4 ammonia molecules coordinated on a copper cationic site reacted with nitrate ionically or covalently associated with copper cationic and copper-oxygen sites. A minor pathway could also involve cationic EFAL sites in place of the copper-oxygen sites. Such a reaction would produce N_2 , H_2O and O_2 , and Cu^{2+} and Cu-O would

be restored. This is in agreement with the results, noting that N_2 and O_2 cannot be detected using IR spectroscopy.

6.4.3 Temperature Effects NH_3 -SCR of NO_2 was carried out at 298 K, 373 K, 423 K, and 473 K over all three zeolites. The reaction temperature affected the rate of reaction (discussed earlier) and, in some instances, the formation/reduction of gas phase and surface species. The amount of gas phase NO remaining post-SCR decreased with increased temperature. Gas phase NO was reduced by ~30-40% at 298 K for all zeolite samples, but reduction climbed to greater than 50%, 50% and 60% at 473 K for Aldrich NaY, nanocrystalline NaY and nanocrystalline CuY, respectively. Interestingly, NO reduction over nanocrystalline CuY was maximized to over 75% at 423 K.

At elevated reaction temperatures the amount of gas phase N_2O initially decreased as seen at 298 K, then began increasing after a few minutes of reaction. This was accompanied by a decrease in the intensity of the NH_4NO_3 bands and an increase in the intensity of gas phase and surface H_2O bands observed post-SCR. These results indicate that ammonium nitrate began thermally decomposing at the higher temperatures according to R. 6.7. The amount of surface NO_3^- remaining post-SCR was reduced as reaction temperature increased, and adsorbed water increased on the zeolites post-SCR. This suggests that higher temperatures might result in a greater overall NO_x reduction, but also lead to an increase in N_2O formation.

6.5 Conclusions

Compared with Aldrich NaY of larger particle size, both nanocrystalline zeolites NaY and CuY showed an increased adsorption capacity for both NO_2 and NH_3 . The reactive sites involved in the formation of surface species from NO_2 and NH_3 adsorption were

distinct on all zeolite samples. Specifically, EFAL sites in nanocrystalline NaY and copper cationic sites in nanocrystalline CuY were responsible for the unique adsorption of reactants. Nanocrystalline NaY resulted in 29% faster initial reaction rate for loss of gas phase NO_2 compared with commercial NaY. This was understood by the enhanced nitrate adsorption capacity, increased external surface area and increased concentration of surface reactive sites in nanocrystalline NaY. Nanocrystalline CuY resulted in a faster initial reaction rate for loss of gas phase NO_2 of 40% compared with Aldrich NaY and 11% compared with nanocrystalline NaY. This is understood as a result of copper cation exchange that increased nitrate adsorption capacity. Additionally, ammonia was activated for SCR by coordination with copper cations. An ammonium nitrate intermediate was formed in the reaction and produced gas phase N_2 , O_2 and H_2O . Temperature studies showed reaction rates were independent of temperature for both Aldrich and nanocrystalline NaY, while reaction rates for nanocrystalline CuY were inversely related to temperature.

Nanocrystalline CuY zeolite has potential as a catalyst for enhanced NO_x emission reduction through NH_3 -SCR. The data presented from this work showed nanocrystalline CuY resulted in increased reaction rates for NO_2 loss at a low temperature and achieved the highest NO reduction at increased temperatures. Further studies will aim to optimize the performance of nanocrystalline CuY for de NO_x applications by identifying the most advantageous reaction temperature to maximize total NO_x reduction while maintaining faster reaction rates and by investigating the effects of oxygen and water as additional reactants.

6.6 Acknowledgements

This material is based on work supported by the Department of Energy (DE-FG-06NT42739) and the National Science Foundation (CRIF CHE-0639096).

CHAPTER 7

AGGLOMERATION, ISOLATION AND DISSOLUTION OF COMMERCIALY MANUFACTURED SILVER NANOPARTICLES IN AQUEOUS ENVIRONMENTS

7.1 Introduction

Nanoscience and nanotechnology offer new opportunities for making superior materials for use in industrial, health, and environmental applications⁹⁹⁻¹⁰⁵. As commercially manufactured nanomaterials become more commonplace, we can expect these manufactured materials have the potential to get into the environment sometime during production, distribution, use or disposal, i.e. sometime during the lifecycle of these materials. In particular, there exists the potential that nanomaterials may make their way into water systems, e.g. drinking water systems, ground water systems, estuaries, lakes etc.¹⁰⁵⁻¹⁰⁷. Nanosilver is currently one of the most common engineered nanomaterials and is used in many applications that lead to the release of silver nanoparticles and silver ions into aqueous systems^{45, 47, 108, 109}. Nanosilver also possesses enhanced antimicrobial activity and bioavailability that may pose a greater environmental risk compared with other manufactured nanomaterials¹¹⁰⁻¹¹². Nanoparticles, the primary building blocks of many nanomaterials, are of particular interest in the study presented here as the fate of nanoparticles in aqueous environments will depend to a large extent on the physical and chemical state of nanoparticles. For example, will nanoparticles be isolated or aggregated in aqueous environments? Will nanoparticles dissolve? What environmental conditions favor aggregation and/or favor dissolution?

Recent studies toward understanding the environmental fate of silver nanoparticles and their potential transformation in the environment have just begun in the past few years, and it is evident that aggregation is an important consideration in the fate of

nanoparticles^{6, 37, 109, 110, 113-115}. There are a number of factors, including pH and surface chemistry, which control both the propensity of nanoparticles to aggregate and the size of the aggregates¹¹⁶⁻¹¹⁸. It is quite clear from the literature there needs to be further systematic studies that integrate silver nanoparticle characterization, which includes physical and chemical bulk and surface properties, with morphology, dissolution and reactivity data under different environmental conditions. A recent review in Nanotoxicology outlining the knowledge gaps in the risk assessment of nanosilver points to the specific need for data examining nanosilver solubility and ion release under varying pH conditions⁴⁷. The importance of an integrated approach is central to understanding the environmental fate and transformation of silver nanoparticles as well as toxicity and nanoparticle-biological interactions^{5, 7, 119}.

In this study, laboratory experiments were conducted to investigate the physicochemical properties and pH dependent solubility of silver nanoparticles that can influence the fate and transformation of manufactured silver nanoparticles in aqueous environments. In particular, the state of the nanoparticles in aqueous environments is investigated under neutral and acidic conditions. Specifically, we are interested in whether silver nanoparticles are present as isolated particles or in the form of agglomerates in these aqueous solutions or will silver nanoparticles dissolve in these environments. These are important questions whose answers will ultimately provide the necessary information needed to predict the environmental fate of nanoparticles under different conditions. For example in transport models, the size regime that needs to be considered or modeled will be very different depending on the state of the nanoparticles. Thus, for a science that is “all about size”, this study focuses on important size issues

beyond just primary particle size that need to be fully understood if the environmental fate of nanoparticles can be predicted or modeled.

7.2 Experimental Methods

7.2.1 Materials Silver nanoparticles (99.9 % purity) were purchased in powder form from Nanostructured and Amorphous Materials, Incorporated (Houston, TX). The manufacturer specifies bare silver nanoparticles (no surface coating) with an average particle size of 10 nm. Optima® water (Fisher Scientific) was used for the neutral solution (pH = 6.5) and preparation of nitric acid solutions. Silver particles (10 μm flakes) were purchased from Sigma-Aldrich (St. Louis, MO).

7.2.2 Powder X-ray diffraction (XRD) A Siemens D5000 X-ray diffractometer with Cu K α target and nickel filter was used to collect a XRD powder pattern for the silver sample. The XRD pattern was collected between angles of 2θ from 10° and 90°.

7.2.3 X-ray Photoelectron Spectroscopy (XPS) A Kratos Axis Ultra XPS instrument was used to analyze the surface composition of the silver nanoparticle sample. The silver nanopowder sample was pressed into indium foil and mounted onto a copper stub. The copper stub with the sample was introduced into the surface analysis chamber, maintained at a pressure in the 10⁻⁹ Torr range during analysis. Silver foil and ion sputtered silver foil were analyzed with XPS for comparison.

7.2.4 BET Specific Surface Area Analysis Nitrogen adsorption isotherms were collected using a Quantachrome Nova 4200e multipoint BET apparatus. Approximately 0.5 g of sample was used for the measurements. Prior to surface area analysis, samples were heated at 160°C and degassed overnight.

7.2.5 Transmission Electron Microscopy JEOL JEM-1230 Transmission Electron Microscope with a Gatan UltraScan camera was used to acquire images of the silver nanoparticles, and ImageJ software was used generate a particle size distribution based on the images. The nanoparticles were deposited on copper TEM grids by placing the grids in the aerosol flow path of the scanning mobility particle sizer between the differential mobility analyzer and the condensation particle counter. Samples were atomized onto the grids for several hours (10).

7.2.6 Electro Spray-Scanning Mobility Particle Sizer (ES-SMPS) In this study, a novel method is used for determining whether commercially manufactured silver nanoparticles form agglomerates, behave as isolated particles, or dissolve as ions in neutral or low pH aqueous suspensions. In particular, an electro spray atomizer coupled to a scanning mobility particle sizer (ES-SMPS) is used to investigate the state of silver nanoparticles in water and aqueous nitric acid environments. The ES-SMPS system and methods were discussed in detail in Section 3.4.10. A schematic of this system is shown in Figure 3.2. Briefly, the electro spray generates an aerosol of nanoparticles that flow through a diffusion dryer and enter the SMPS for size determination. Particle size is determined based on mobility diameter, D_p . It should be noted that the data are shown in terms of bin and reported as, $dN/d\log D_p$ versus $\log D_p$.

An agglomeration of nanoparticles will flow through the system with the mobility of one larger particle and will, therefore, be measured as a larger particle. Different agglomerate configurations of spherical particles have been shown to produce unique particle size distributions with SMPS analysis¹²⁰. Therefore, a range of agglomerate

sizes within a sample can be discriminated according to shifts in the particle size distributions using the ES-SMPS system.

Silver nanoparticles were suspended in water and aqueous nitric acid solutions at each pH studied at 0.65 wt %. The suspensions were prepared by adding the aqueous solution to the powder sample and agitating with ~ 1 minute of sonication to disperse the particles without addition of the excess heat and energy of long sonication times. The samples remained as stable dispersions for hours ($\text{pH} < 3$) to days ($\text{pH} \geq 3$) and were suspended for the duration of ES-SMPS analysis. Each suspension was analyzed with the ES-SMPS system immediately upon adding the solution to the particles.

There is a recognized need to identify proper methods to measure nanoparticles in various media⁴⁵⁻⁴⁸. The ES-SMPS is well suited for determining particle size distributions and changes in those distributions for aqueous suspensions of metal and metal oxide nanoparticles and has shown excellent agreement with more conventional techniques such as TEM and SEM¹²¹⁻¹²⁶. Although DLS (Dynamic Light Scattering) is routinely used for aqueous nanoparticle size measurements, it has several drawbacks that make it ill-suited for many nanoparticle suspensions. It is not ideal for samples that undergo interparticle interactions or changes in particle size distribution due to a tendency to floc, aggregate, sediment or dissolve as this complicates light scattering measurements based on Brownian motion. DLS also requires significantly diluted samples^{48, 127, 128}. Such complications caused inconsistent and inaccurate DLS measurements of the samples in this study, thus DLS was not used as a complementary technique.

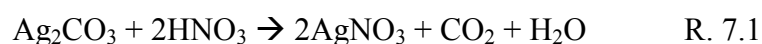
7.2.7 Zeta Potential Measurements Zeta potential measurements were conducted using the Zetasizer Nano ZS (Malvern, Southborough, MA). The silver nanoparticles were suspended in water and aqueous nitric acid solutions at each pH studied at a concentration of 1 mg/ml. The zeta potential determinations were based on electrophoretic mobility of the nanoparticles in the aqueous medium, which were performed using folded capillary cells in automatic mode.

7.2.8 Inductively Coupled Plasma/Optical Emission Spectroscopy (ICP/OES) A Varian Plasma Inductively Coupled Plasma Optical Emission Spectrometer (ICP/OES) 720-ES was used to determine the concentration of silver ions in solution for water and aqueous nitric acid solutions at each pH studied. The silver suspensions were filtered with 0.2 μm Xperten filters and centrifuged at 14,000 rpm for 30 minutes to separate nanoparticles from the solution. Five standard solutions with known silver concentrations were prepared as calibration standards. Exact concentrations of silver in the sample solutions were obtained by projection from the working calibration curve generated from standard solution data.

7.3 Results and Discussion

7.3.1 Characterization of Commercially Manufactured Silver Nanoparticles in the Dry State with XRD, XPS, BET, and TEM The commercial silver nanoparticles were analyzed in the dry state to characterize crystalline phases in the sample, surface composition and coatings, surface area, agglomeration state and size of the nanoparticles. The XRD patterns in Figure 7.1 compare the silver nanoparticle results with metallic silver and silver oxide (Ag_2O , AgO) references. The data show the nanoparticles are

metallic silver with no detectable silver oxide present. The silver nanoparticles were then examined with a surface sensitive technique, XPS, (Figure 7.2), to determine if there was a thin oxide surface layer present. Spectra were acquired and curve fitting applied by Dr. Jonas Baltrusaitis (laboratory of Dr. Vicki Grassian, The University of Iowa). Peak fitting was applied to the high resolution scans in the Ag3d (upper), O1s (middle), and C1s (lower) regions of the photoelectron spectrum. The Ag3d doublet at 368.2 eV and 374.2 eV is consistent with silver in the Ag⁰ oxidation state, and the shoulder at 367.8 eV is consistent with the presence of Ag(I), often attributed to formation of Ag₂O or Ag₂CO₃ on the surface¹²⁹. The O1s region does not show any oxygen peaks below 530 eV due to AgO or Ag₂O, but there is a peak due to CO₃²⁻ at 530.7 eV in the nanoparticle sample. The peaks at 531.4 (foil), 532.1 (foil and nanoparticles), and 533.2 eV (foil and nanoparticles) correspond to OH⁻, C=O, and C-O-C and C-OH, respectively. The C 1s region shows adventitious carbon present on both the foil and the nanoparticle samples. There are unique peaks on the nanoparticle sample at 287.3 and 288.7 eV attributed to C=O and CO₃²⁻, respectively. It can be seen in Figure 7.2 that for the foil these peaks all diminish in intensity upon Ar⁺ sputtering of the top few surface layers. In summary, for the nanoparticles, the XPS data indicate the presence of adventitious carbon, some carbon-oxygen functionality, likely due to the use of surfactants during synthesis to control particle size, and Ag₂CO₃ on the surface of the silver nanoparticles. The surface carbonate layer reacts with nitric acid to produce soluble silver nitrate:



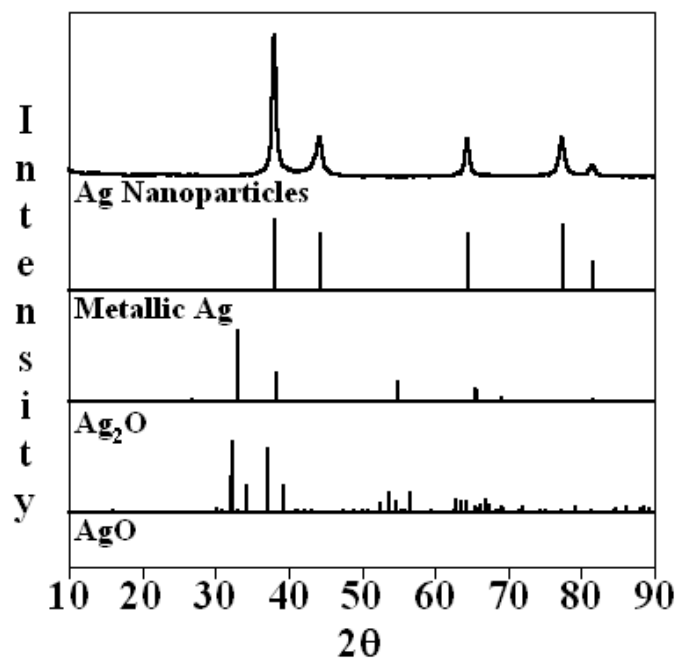


Figure 7.1 Powder x-ray diffraction patterns for silver nanoparticles with XRD patterns shown for several reference compounds.

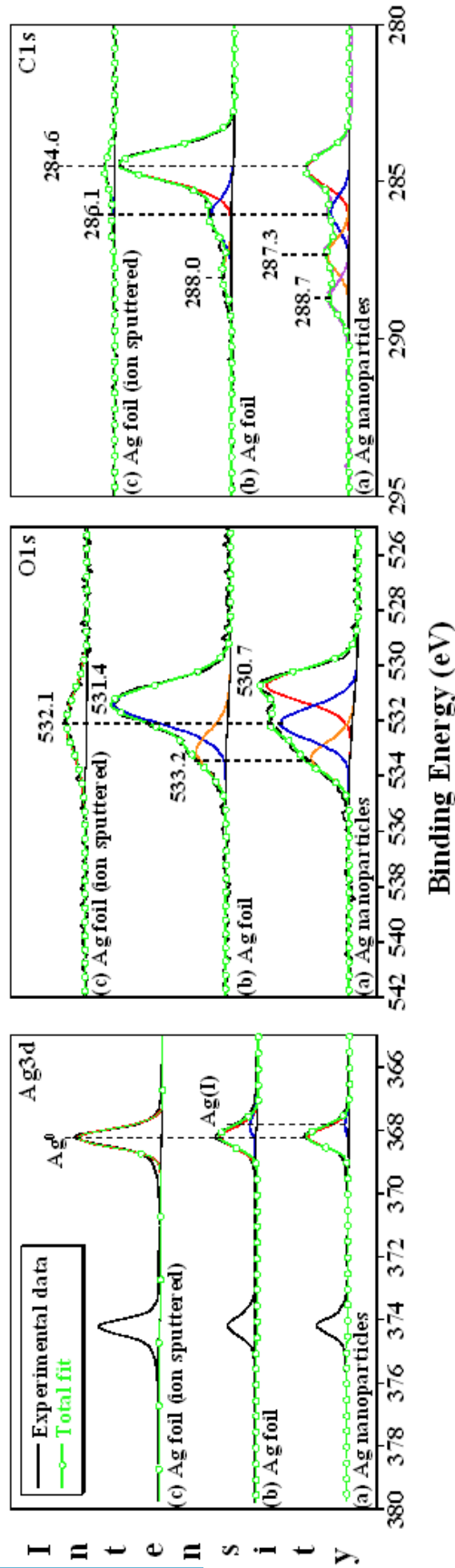


Figure 7.2 X-ray photoelectron spectra for silver nanoparticles (a), silver foil (b), and ion sputtered silver foil (c), showing the Ag 3d region (upper), the O 1s region (middle), and the C 1s region (lower). A peak-fit was applied to each region. The black solid line represents experimental data and the green line represents the total calculated fit. The blue, red, orange, and purple curves represent components used to curve fit the spectra. (Spectra acquired by Dr. Jonas Baltrusaitis, laboratory of Dr. Vicki Grassian, The University of Iowa). (Elzey, S.; Grassian, V. H. *Journal of Nanoparticle Research*.)

The data also show, in agreement with the XRD results, that there is no evidence of a surface oxide layer. The specific surface area of the silver nanoparticles was determined to be $3 \pm 2 \text{ m}^2/\text{g}$ using multi-point BET analysis.

The primary and agglomerate size of the silver nanoparticles in the dry state were characterized using TEM analysis (Figure 7.3). A particle size distribution was generated from the TEM images by measuring the diameter of more than 500 nanoparticles.

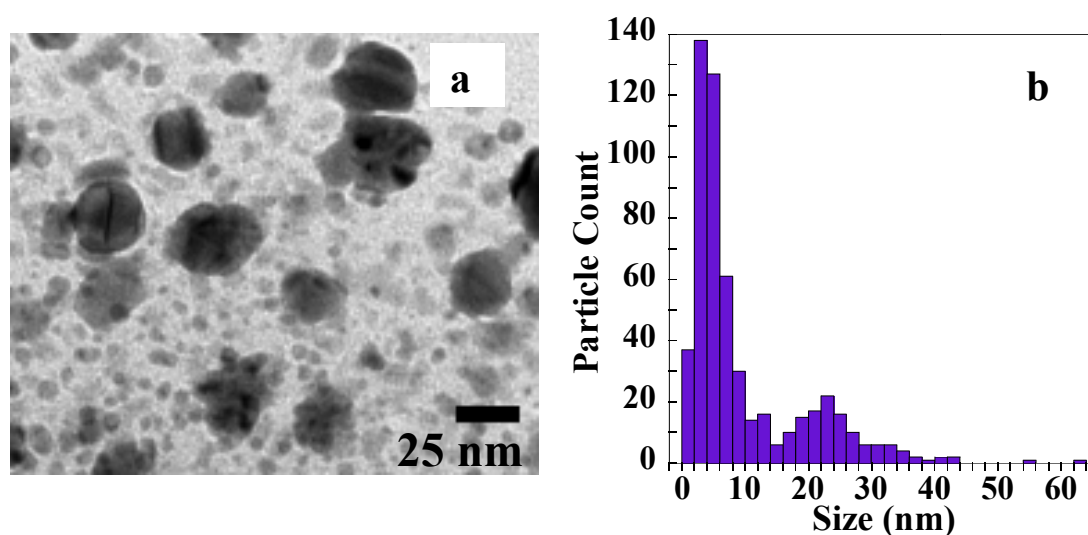


Figure 7.3 TEM image of silver nanoparticles substrate-deposited from a water suspension (a) with the corresponding particle size distribution using ImageJ software (b).

The TEM image in Figure 7.3a shows a majority of smaller particles in the range of 2-10 nm, and a small quantity of larger particles ~15-30 nm. The image also shows the smaller particles are primarily isolated but form agglomerates with diameters of ~10-40 nm. Therefore, the first mode of the bimodal particle size distribution, with a peak

maximum at 5 nm, is attributed to nanoparticles < 10 nm in diameter that account for ~85-90% of the total particle count. The second mode, with a peak maximum at 22 nm, is attributed to larger single particles and agglomerates of the smaller particles that account for $\leq 15\%$ of the total particle count.

7.3.2 ES-SMPS Analysis of Aqueous Suspensions of Silver Nanoparticles Particle

size distributions of the silver nanoparticles were determined for suspensions in neutral and aqueous nitric acid solutions over a range of pH values using ES-SMPS analysis.

The particle size distribution for the silver nanoparticles suspended in water is bimodal, with peak maxima at 5.3 and 23.3 nm (Figure 7.4a). These peak maxima agree well with the results from TEM analysis of the silver nanoparticles aerosolized from a water suspension, but the relative intensities of the two modes are inverted. This could be attributed to size biasing in the SMPS measurement in part to a greater loss of the smaller nanoparticles due to diffusion¹³⁰. However, it is also likely due to agglomeration of the smaller particles. The individual particles that form an agglomerate are often easily distinguishable in TEM images, and their diameters can therefore be measured separately for a particle size distribution that represents the primary particles. However, during ES-SMPS analysis, an agglomerate of primary particles is measured as one larger particle, and a single diameter is determined. Thus, the inverted intensities of the two modes in the particle size distribution from SMPS compared with TEM analysis indicate more agglomeration of the primary particles in the aqueous phase.

ES-SMPS analysis was used to determine particle size distributions for the silver nanoparticles suspended in acidic media. Data for aqueous nitric acid solutions at pH values ranging from 3.5 to 0.5 are shown in Figure 7.4b. At pH values greater than 3.5,

i.e. from 3.5 to 7.0, there were no significant differences compared with the neutral solution as seen by a small shift in the peak maximum of the particle size distribution of < 2 nm between the neutral

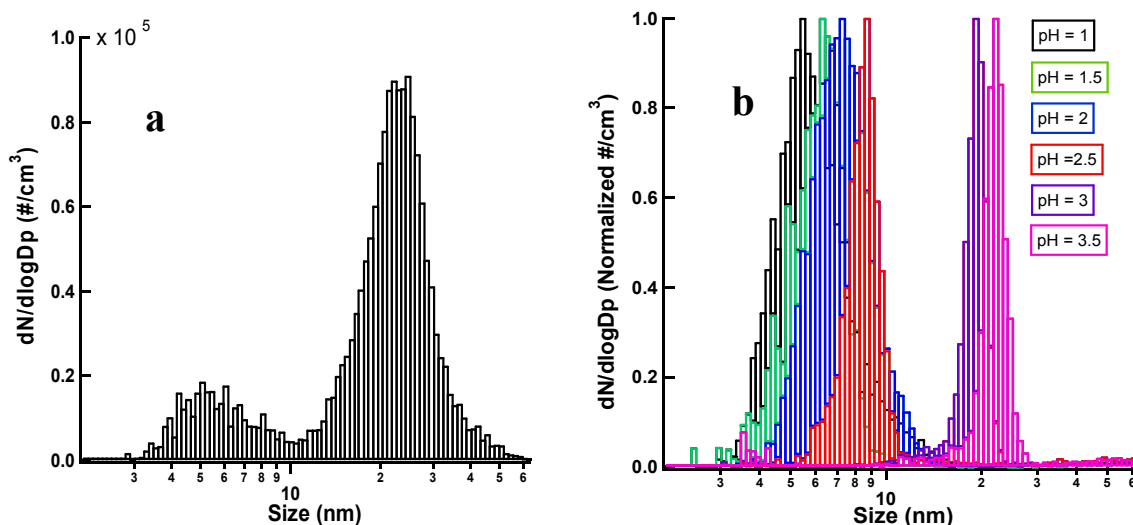


Figure 7.4 SMPS particle size distribution for silver nanoparticles aerosolized from a water suspension (a), and normalized SMPS particle size distributions for silver nanoparticles aerosolized from aqueous nitric acid suspensions at a range of pH values (b).

suspension and the acidic suspension at pH = 3.5. Similarly, from pH = 3.5 to pH = 3 there was a small shift of < 3 nm. However at lower pH, there was a significant shift of more than 10 nm between pH 3 and pH 2.5, and from pH 2.5 through pH 1 there were small shifts of < 1 nm – 1.5 nm. At pH 0.5 no particle size distribution was detectable. The shift in the particle size distribution at each pH value was immediate, and there was no change in the particle size distribution over time (measured for two months) with any

of the suspensions. ES-SMPS analysis was coupled with TEM analysis at pH 3 and pH 1 to compare the particle size distributions produced from both methods. The TEM images and corresponding particle size distributions in Figure 5 show excellent agreement between the two methods, with peak maxima at 18 nm (TEM) and 18.8 nm (SMPS) for pH = 3 and 5 nm (TEM) and 5.4 nm (SMPS) for pH 1.

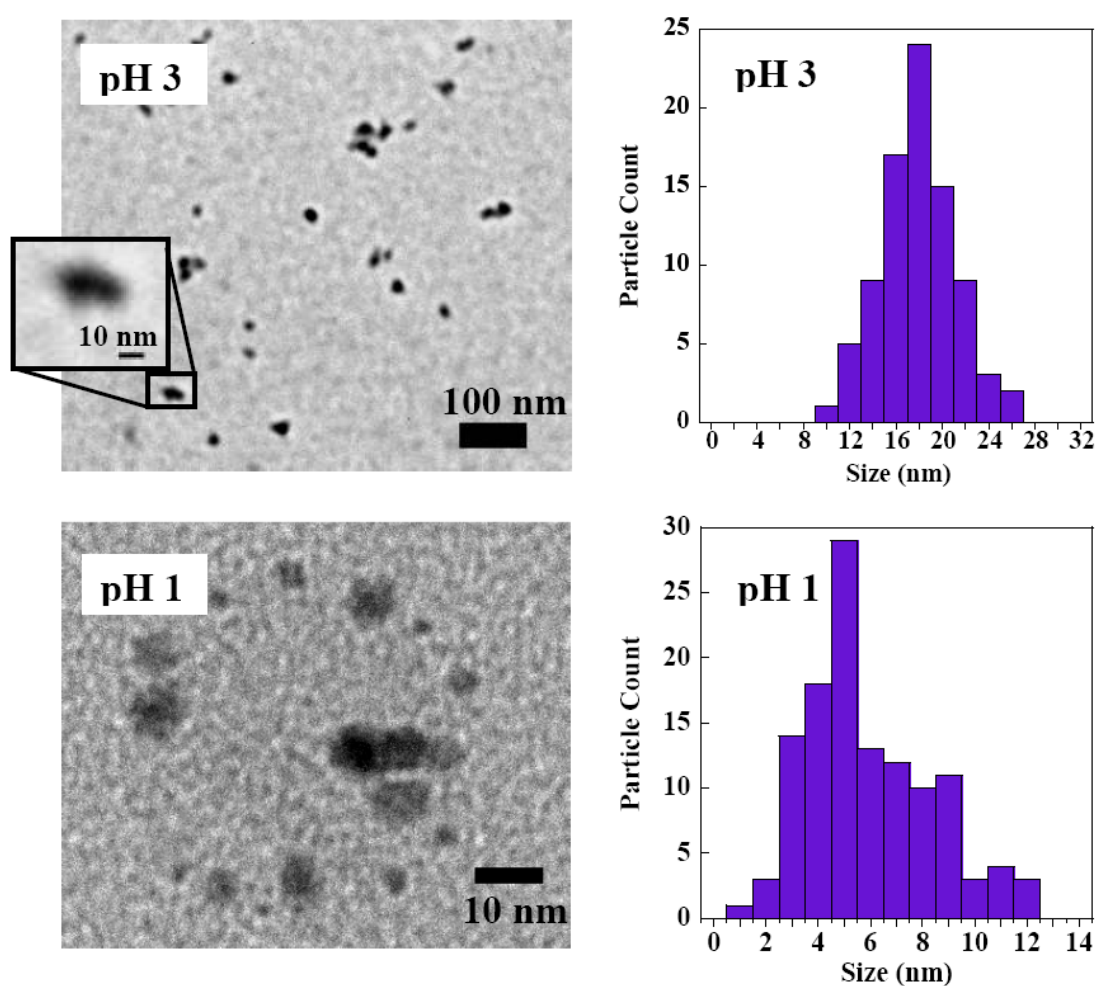


Figure 7.5 TEM images (left) and corresponding particle size distributions (right) using ImageJ software for silver nanoparticles substrate-deposited from aqueous nitric acid suspensions at pH 3 (upper) and pH 1 (lower).

In addition to the shifts in particle size distributions, changes in the color of the silver nanoparticle suspensions were observed (Figure 6a). Silver nanoparticles suspended in water appeared to be cloudy and dark brown in color. The aqueous nitric acid suspensions at pH 3.5 and pH 3 were similar in appearance to the neutral suspension. There was a significant change in color from a dark brown to a pale yellow suspension between pH 3 and pH 2.5, which are the same pH values that correspond to the large shift in particle size distributions. From pH 2.5 through pH 1 the suspension was cloudy and pale yellow, and at pH 0.5 the appearance was transparent and colorless. The silver nanoparticle suspensions were not stable indefinitely, but instead established an equilibrium between agglomeration and more soluble, dispersed particles. The nanoparticles and agglomerates remained dispersed for periods of hours (pH values of 1 - 2.5) to days ($\text{pH} \geq 3$) before larger agglomerates began to settle towards the bottom, while isolated nanoparticles still remained suspended in solution. The ES-SMPS system samples the suspended portion of the nanoparticles, and agitating the suspensions resuspended the settled portion. For comparison, an equal mass of bulk silver ($\sim 10 \mu\text{m}$) was put in nitric acid at pH 0.5 (Figure 6b). The larger silver particles settled and retained the appearance of solid silver.

The ES-SMPS data suggest the silver nanoparticles exist as agglomerates in aqueous nitric acid at pH values of pH 3 and greater. Agglomerate sizes were smaller than those in water by $\sim 2\text{-}5 \text{ nm}$, indicating the acidic solution causes slight deagglomeration at these pH values. At pH 2.5 the data show the silver nanoparticles significantly deagglomerate, and result in a particle size distribution consistent with isolated nanoparticles. The change in the color of the suspension at pH 2.5 is likely due to this

decrease in the size of the suspended particles¹³¹. From pH 2.5 through pH 1 the data remain consistent with the size of the isolated nanoparticles, and the small changes in the particle size distributions may be due to continued deagglomeration of the smallest particles < 3 nm in diameter or the isolated particles may have started to dissolve. The TEM images in Figure 7.5 show at pH = 3 there are indeed agglomerated particles, while at pH 1 the particles are isolated. At pH 0.5, the silver nanoparticles appear to completely

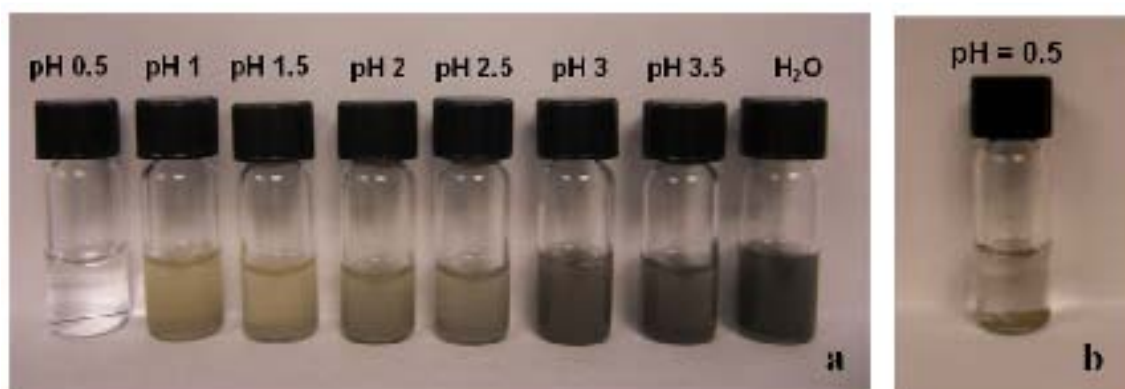


Figure 7.6 Digital photograph of silver nanoparticle suspensions in water and aqueous nitric acid solutions at various pHs (a) and bulk silver in aqueous nitric acid at pH = 0.5 (b).

dissolve in ~2 – 3 minutes, and there is no particle size distribution detected using ES-SMPS analysis. To understand the shift in particle size distribution with pH, complementary techniques were used to further investigate the stability of the silver suspensions. Solution phase measurements of zeta potential and silver ion concentration used to determine at which pH values and to what extent dissolution occurs.

7.3.3 In Situ Measurements Using Complementary Techniques Including Zeta Potential Measurements and ICP/OES

Zeta potential measurements were conducted to evaluate the stability of the silver suspensions (Figure 7.7). Zeta potential, ξ , is based on the mobility of a particle in an electric field and is related to the electrical potential at the junction between the diffuse ion layer surrounding the particle surface and the bulk solution. A high magnitude ($\xi \geq 25$ mV) indicates stability, and a value of zero corresponds to the isoelectric point (pI) when the particle is stationary in an electric field. DLVO (Derjaguin, Landau, Verwey, and Overbeek) theory assumes the stability of a colloidal suspension is the sum of attractive van der Waals forces (V_A) and repulsive electrostatic forces (V_R) between particles as they undergo Brownian motion¹³². The total potential energy (V_T) of a particle in solution can be expressed as

$$V_T = V_A + V_R \quad \text{Eq. 7.1,}$$

with V_A and V_R defined as

$$V_A = -A/(12 \pi D^2) \quad \text{Eq.7.2}$$

and

$$V_R = 2 \pi \epsilon a \xi^2 \exp(-\kappa D) \quad \text{Eq. 7.3}$$

where A = Hamaker constant, D = particle separation, a = particle radius, ϵ = solvent permeability, $1/\kappa$ = Debye length, and ξ = zeta potential.

A stable suspension requires a dominant repulsive force to maintain dispersion of the particles. If the attractive forces dominate, or particles collide with sufficient energy to overcome repulsion, they will begin to floc and eventually form agglomerates that sediment. Typically, particle adhesion is irreversible because there is a large energy barrier that prevents separation. In certain situations, interparticle repulsion decreases and

a second energy minimum with a small energy barrier exists. This can result in weak, reversible flocculation that occurs when the zeta potential is near zero. In this case, loose agglomerates are easily broken apart with agitation, and the primary particles are resuspended¹³³. The secondary minimum effect is consistent with the observation of quicker particle sedimentation that was easily reversed at lower pH values.

In water the silver suspension of agglomerates exhibits stability, with a high ξ magnitude of -42.7 mV. The magnitude decreases with pH but indicates moderate stability through pH 3 at -30.7 mV. At pH 2.5, the magnitude decreases significantly to -5.5mV, corresponding to a less stable suspension. This supports the suggestion that smaller silver particles are present at pH 2.5, since the smaller particles would be expected to be less stable due to increased surface free energy¹³⁴. The magnitude of ξ continues to decrease with pH, approaching the pI near pH 1.5. The ξ magnitude increases, transitioning to positive values of 6.7 mV at pH 1 and 13.1 mV at pH 0.5.

Inductively coupled plasma was used to quantify how much of the original silver concentration dissolved in each solution. Results for the silver nanoparticles are shown in Figure 7.8 with comparison to micron-sized silver particles (10 μm), and characterization data for silver nanoparticle suspensions are summarized in Table 7.1. A small but measurable amount of silver, 0.5 %, was detected in the water solution. An increasingly small amount of silver dissolved in the aqueous nitric acid solutions as the pH value decreased, but at pH 1.5 the amount of dissolved silver decreased slightly. This is most likely due to the fact that pH 1.5 corresponds closely to the isoelectric point (pI) of the suspension (where $\xi = 0$), and solubility can decrease at pH values corresponding

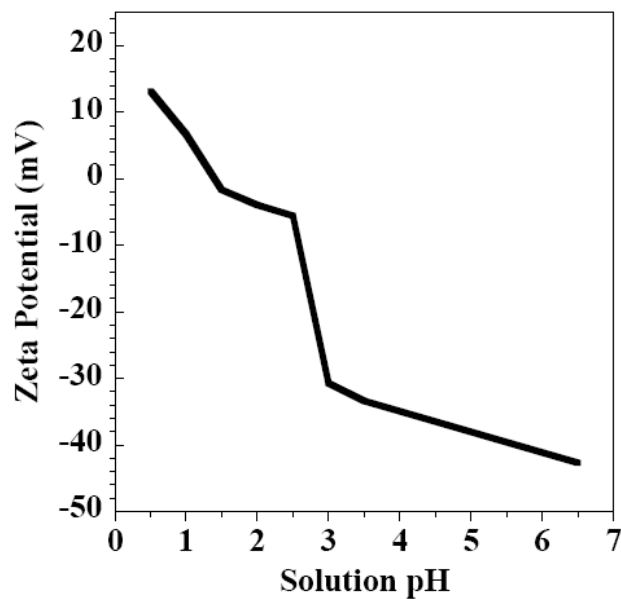


Figure 7.7 Plot of zeta potential measurements as a function of pH for silver nanoparticles suspended in water and acidified with nitric acid solutions after 24 hrs.

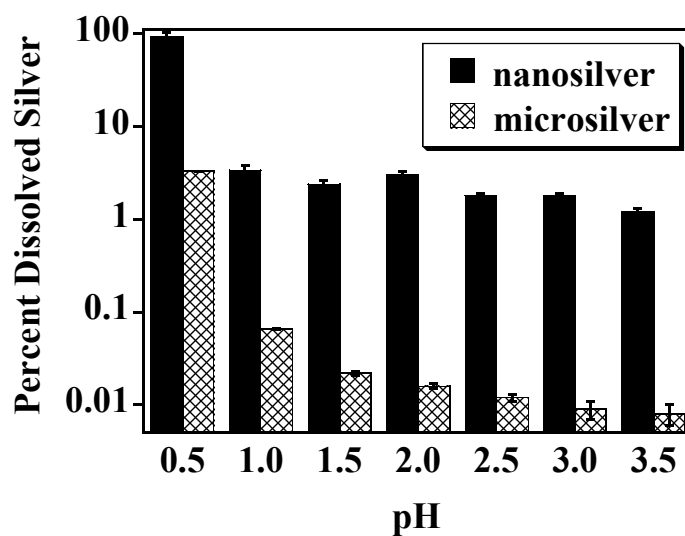
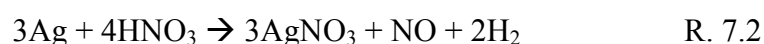


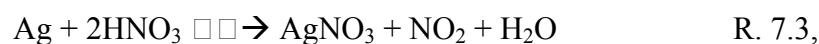
Figure 7.8 ICP results for percent dissolved silver for nanosilver and microsilver particles in aqueous nitric acid solutions after 24 hrs.

to the pI¹³⁵. From pH 3 to pH 2.5 the amount of dissolved silver did not increase. This supports the conclusion that the large shift in particle size distributions from pH 3 to pH 2.5 with ES-SMPS analysis was due to agglomerates that were present at pH 3 breaking apart into isolated nanoparticles at pH 2.5 rather than dissolution of the silver nanoparticles. At pH 0.5 there is a large increase in the amount of dissolved silver, with 93% of the total silver in solution. This result verifies the conclusion of silver nanoparticle dissolution indicated by the ES-SMPS analysis.

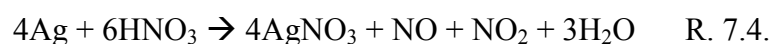
Bulk silver dissolution in nitric acid has been well researched^{136,137}, with a consensus that the important factors include acid concentration, reaction temperature, and particle size. Silver of larger particle sizes (10 – 800 μm) does not dissolve in nitric acid until the acid concentration is ~ 4 M and reaches a maximum at ~ 10 M. Faster reaction rates occurred with increased temperature. The dissolution mechanism has been modeled as a chemical reaction controlled process, according to reactions



and



with the net reaction



Reaction 7.2 occurs at with dilute acid concentrations (~4 -7 M) and R. 7.3 dominates higher concentrations (~7 – 10 M)¹³⁷. The data presented here show silver nanoparticles with a primary particle size of ~5 nm dissolve in acidic concentrations ~ 10 times weaker

Table 7.1 Summary of Analysis for Silver Nanoparticles Suspended in Water and Aqueous Nitric acid solutions

Ag Suspension	Appearance	SMPS Peak Max (nm)	Zeta Potential (mV)	ICP (% Ag dissolved) ^a
Water	Cloudy, brown suspension	23.3 and 5.3 ± 0.4	- 43 ± 1	0.50 ± 0.04
HNO ₃ pH 3.5	Cloudy, brown suspension	21.7 ± 0.6	- 33 ± 2	1.2 ± 0.1
HNO ₃ pH 3.0	Cloudy, brown suspension	18.8 ± 0.5	- 31 ± 1	1.8 ± 0.1
HNO ₃ pH 2.5	Cloudy, yellow suspension	8.5 ± 0.1	- 6 ± 2	1.8 ± 0.1
HNO ₃ pH 2.0	Cloudy, yellow suspension	7.1 ± 0.2	- 4 ± 1	3.0 ± 0.3
HNO ₃ pH 1.5	Cloudy, yellow suspension	6.3 ± 0.2	- 2 ± 3	2.4 ± 0.2
HNO ₃ pH 1.0	Cloudy, yellow suspension	5.4 ± 0.1	7 ± 2	3.4 ± 0.4

^a Ag ions or soluble Ag

^b Geometric mean is the sum of the particle concentrations in each bin divided by the total particle concentration.

^c n.o. = not observed

than the concentration required for dissolution of bulk silver particles, demonstrating unique, size dependent dissolution behavior for silver nanoparticles. The behavior trends of silver nanoparticles in different pH environments are summarized in Fig. 7.9 as a diagram of the state, color, electric potential and percent dissolved silver over the pH range studied.

7.4 Environmental Implications The primary purpose of this laboratory study is to contribute to the growing database of the potential environmental and health implications of nanoscience and nanotechnology. In particular, it is expected that these studies will help answer questions concerning the transformation and fate of manufactured silver nanomaterials and the conditions under which silver nanoparticles will form agglomerates and the size of the agglomerates, as this is related to the mobility of nanoparticles in aqueous environments. Furthermore, dissolution of silver nanoparticles will contribute to the concentration of silver ions in the environment in general and in water systems in particular^{47, 108, 109, 138}. Little is known about the propensity of silver nanoparticles to dissolve under various environmental conditions, as well as size dependence of the dissolution process. The data presented in this study show manufactured silver nanoparticles possess a greater likelihood of contributing to metal ions in aqueous environments due to a broader range of acid concentrations that facilitate dissolution of the nano-sized particles compared with larger micron sized silver particles.

Silver is one of the most commonly manufactured nanomaterials, second only to carbon⁴. As such, silver nanomaterials will undoubtedly make their way into the environment and interact with their surroundings. Due to its antimicrobial properties,

silver is commonly used in pharmaceuticals, medicines, cleaning (antibacterial soaps), water purification, and numerous

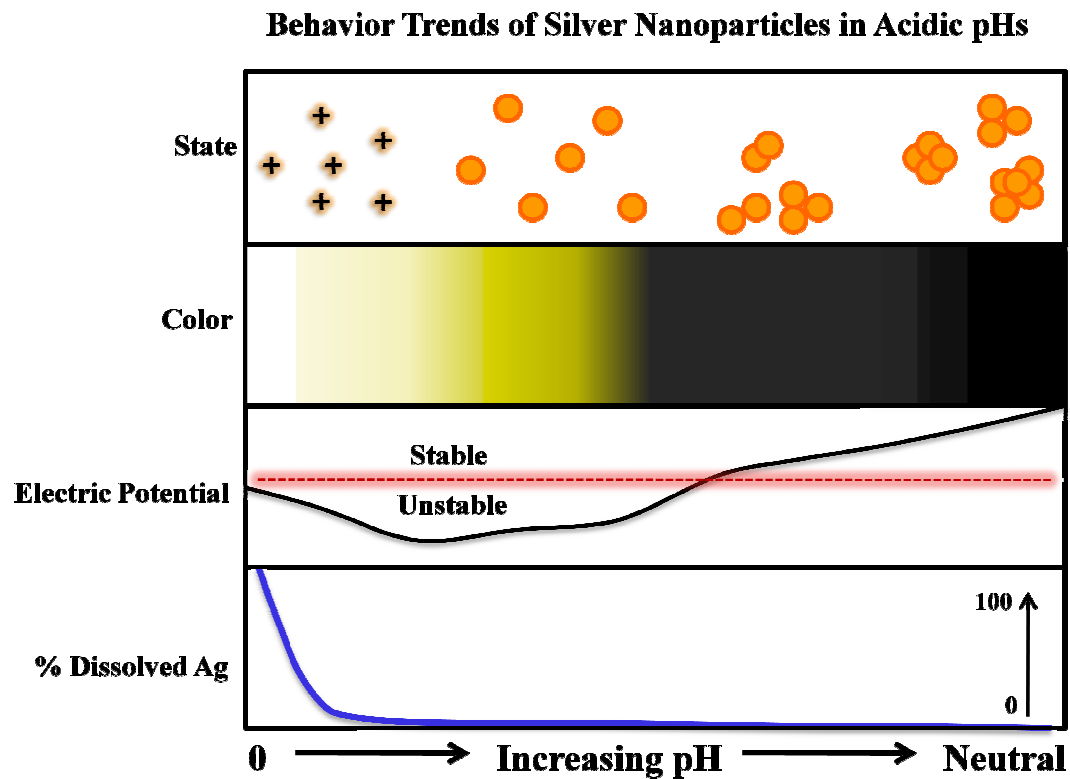


Figure 7.9 Summary of the behavior trend for commercially manufactured silver nanoparticles in aqueous acidic environments. The state of the nanoparticles (top) shows agglomeration at neutral pH, trending to deagglomeration, isolated particles, and silver ions at low pH. The color of the suspension trends from black (neutral) to gray to yellow to a colorless solution at low pH. The electric potential of the suspended particles trends from stable (neutral) to unstable, and becomes more stable after the isoelectric point minimum. The percent dissolved silver (bottom) is small but detectable at neutral pH and increases rapidly at $\text{pH} \leq 0.5$.

commercial products and processes¹³⁹. Silver is released into each environmental compartment, including agricultural land, aquatic environments and the atmosphere^{140, 141}. Current

calculations predict nanosilver will enter the air, soil and water, and water systems will have the highest associated risk based on predicted environmental concentrations¹³⁸. For micron-sized silver, only a small portion lost to the environment is biologically available, but this could grow as silver nanomaterials become increasingly incorporated into commercial applications^{47, 108, 140, 142}.

Nitric acid is used in production of explosives and manufacture of pharmaceuticals, medicines, fertilizers, pesticides, cleaning agents (clog remover), water purification as a nitrogen source for micro-bacteria, and is also a component of acid rain¹⁴². Comparison shows there is overlap among many applications and/or sources of nanosilver and nitric acid in the environment. Thus, silver nanomaterials and low pH aqueous nitric acid conditions have the potential to coexist in localized areas of the environment, most notably agricultural land and aqueous environments such as groundwater, waste water, and acid rain. While silver nanoparticles may have minimal solubility in neutral aqueous environments, once silver is solubilized (silver ions or soluble silver) it may remain soluble when transported in aqueous environments. Moreover, suspended silver nanoparticles were shown to cause toxicity in a variety of model aquatic organisms, and the lethal concentrations could not be attributed to dissolved silver ions. Certain species were even shown to be more susceptible to nanoparticles of silver than to soluble silver^{111, 143, 144}. Therefore, the fate of silver nanoparticles in aqueous environments needs to be considered even if silver ions are not generated.

Furthermore, the potential for nanodust as a new source of metals in the atmosphere has been discussed¹⁴⁵. Properties such as size, shape, surface composition and morphology will affect the propensity of a material to form dust, and nanomaterials may have a greater propensity to become airborne compared with larger-sized particles^{146, 147}. It is well known that mineral dust aerosol can react with acids in the atmosphere and undergo atmospheric processing, transport, and wet and/or dry deposition onto land and aqueous environments. Such acid-mobilization of metals from dust particles has been studied for naturally occurring iron-containing mineral dust¹⁴⁸, and may prove to be a significant process in the environmental transport and fate of engineered nanodust on a global scale^{145, 149}. Nitric acid is known to be an important gas-phase component of the atmosphere that can acidify dust particles to pHs less than 2 according to some recent atmospheric models¹⁴⁸. Therefore, the low pH aqueous environments considered in this study can be created around an aerosol particle surface, leading to increased soluble metal ions. The subsequent transport and deposition to land or water can release ions into the environment due to this atmospheric processing. The widespread use of silver in nanotechnologies and the presence of nitric acid in the atmosphere in significant concentrations may well lead to environmental conditions comparable to the simulated environment generated in this study

This study has shown silver nanoparticles can be transformed in size or state (soluble silver and silver ions) within minutes in low pH aqueous nitric acid, affecting the bioavailability, atmospheric chemistry, transport, and fate of silver nanomaterials in the environment. Low pH aqueous nitric acid conditions represent an existing environment in which silver nanoparticles, a specific commonly manufactured nanomaterial, may

enter, and the methods used in this study can be applied to a variety of nanoparticle-aqueous solution combinations of environmental interest.

7.5 Acknowledgements

The authors would like to thank Dr. Jonas Baltrusaitis for the XPS analysis. Although the research described in this article has been funded wholly or in part by the Environmental Protection Agency through grant number EPA R83389101-0 to VHG, it has not been subjected to the Agency's required peer and policy review and therefore does not necessarily reflect the views of the Agency and no official endorsement should be inferred. This research was also supported in part by the Department of Defense (DoD) through the National Defense Science & Engineering Graduate Fellowship (NDSEG) Program and by the Center for Health Effects of Environmental Contamination.

CHAPTER 8

NANOPARTICLE DISSOLUTION FROM THE PARTICLE PERSPECTIVE: INSIGHTS ON NANOSCALE PROCESSES FROM PARTICLE SIZING MEASUREMENTS

8.1 Introduction

The recent explosion in applications of nanomaterials requires proper methods for characterization and analysis to assess risk and facilitate advancements in nanoscience and nanotechnology^{150, 151}. The dissolution of nanoparticles is an important process in the evaluation of environmental, health and safety risks of nanomaterials, as particle size changes due to dissolution play a key role in transport, reactivity, bioavailability, translocation, and fate of nanomaterials^{7, 113, 152-155}. Nanoparticle dissolution is also an important consideration in drug development, as the pharmaceutical sector increasingly uses nanoparticles for controlled release of drugs and sensing agents^{156, 157}. A correlation of nanoparticle size data with in vivo dissolution data is recognized as an important approach in monitoring and predicting drug release^{158, 159}. However, many techniques used to monitor nanoparticle dissolution do not directly monitor PSDs. Instead, they may rely on light scattering, but results can be affected by interparticle interactions, and these techniques are particularly challenged by particles less than 10 nm⁷. Techniques that detect solution phase ion concentrations give bulk average concentrations and offer no detailed information on how particle size changes as a function of the dissolution process. Because nanoparticles exhibit unique, size-dependent behavior, particle size effects cannot be ignored and must be explicitly monitored so that a fundamental understanding of the underlying size-dependent processes on the nanoscale can be discerned¹²². This study investigates the acid-assisted dissolution of manufactured copper nanoparticles in

hydrochloric acid by monitoring PSDs. This work demonstrates a new application of the electrospray atomizer coupled with a scanning mobility particle sizer (ES-SMPS) for real-time monitoring of nanoparticle dissolution in the aqueous phase. ES-SMPS is a technique that has been used to characterize aerosol particles and is more recently used to characterize colloidal suspensions^{123, 160, 161}.

8.2 Experimental Methods

The acid-assisted dissolution of copper nanoparticles was monitored as a function of time using the ES-SMPS. The ES-SMPS system and operation were discussed in detail in Section 3.4.10. Copper nanoparticles (CuNPs) were purchased in powder form from Nanostructured and Amorphous Materials, Inc. (Houston, TX). Details of the CuNP characterization, including TEM, BET, XRD, and XPS data, can be found in Pettibone et al.¹⁶² Hydrochloric acid (0.5 M) was added to the CuNPs for a sample concentration of 1 wt % copper. The suspension was dispersed by agitation for < 30 seconds and immediately analyzed with the ES-SMPS. A PSD was acquired at intervals of approximately 3-6 minutes until no PSD could be detected. An inductively coupled plasma optical emission spectrometer (ICP/OES) was used to verify the concentration of copper ions in solution as discussed in Section 3.4.9.

8.3 Results and Discussion

The PSDs for the ES-SMPS dissolution are shown in Figure 8.1. Results show a shift in the peak maximum of the PSDs to smaller sizes with time, as expected; however, an unexpected feature is that the PSDs become more polydisperse. Unique features of the data are the bi- or tri-modal PSDs evident at $t > 0$. Similar multimodal PSDs have also been observed during solution phase nanoparticle growth as

monitored with in situ TEM¹⁶³. Analogous dynamic interparticle interactions, such as concurrent dissolution and/or coalescence, may be occurring at different rates due to variable surface energies and particle mobilities as size changes during dissolution. Studies investigating the size dependent dissolution of ZnO nanoparticles were unable to accurately model dissolution rates due to such dynamic processes¹⁵². Such studies support the usefulness of investigating nanoscale processes from the particle perspective by detecting PSDs. These complex processes cannot be easily detected by measuring the production of solution phase ions during dissolution using standard methods of analysis.

Surface chemistry studies of nanoparticles have shown that shifts in particle size as small as < 0.5 nm due to changes in surface chemistry, including molecular desorption, oxidation, and thin coating growth, can be detected through direct observation of PSDs¹⁶⁴⁻¹⁶⁶. Thus, real-time monitoring of PSDs during dissolution provides new insights into particle size changes during dissolution of nanoparticles. The particle number concentration varied during dissolution as smaller particles appeared to dissolve at an inherently faster rate, and larger particles generated PSDs with smaller peak maxima during dissolution. A PSD was detected at significant concentrations down to a size of $\sim 3-4$ nm, and there was a continual shift in the peak maximum as the larger particles in the sample moved toward this size and rapidly dissolved and disappeared from the PSD. Below 3-4 nm, the particles dissolved completely between subsequent scans. After 30 minutes, the PSD maintained a particle number concentration, peak maximum, and polydispersity indistinguishable from a 1 wt % Cu ion standard solution

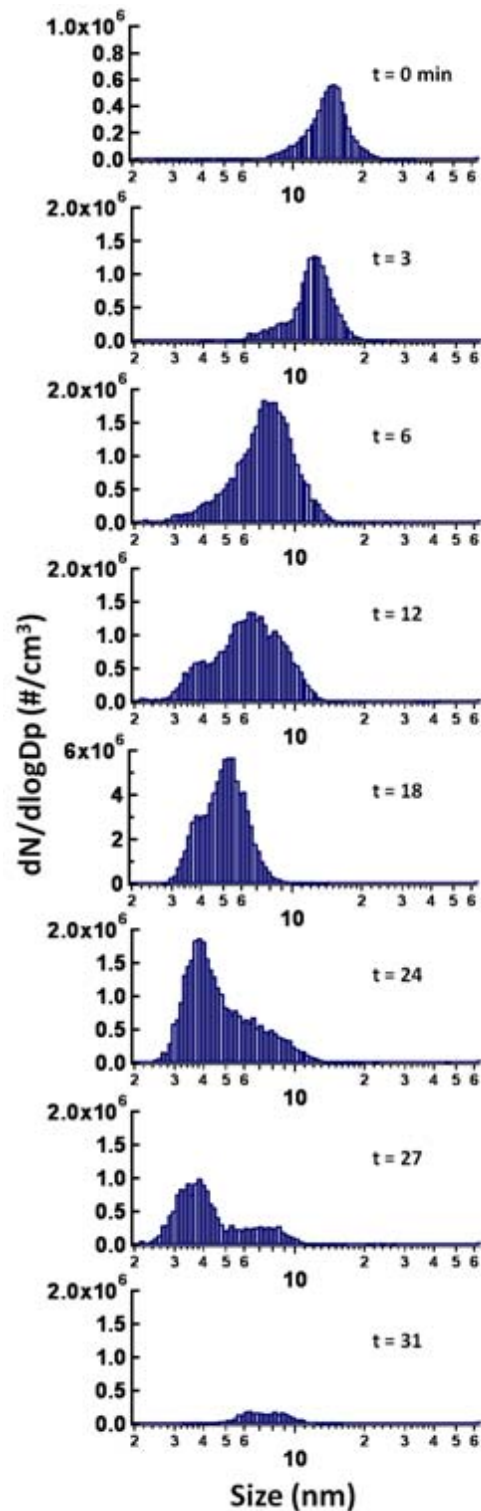


Figure 8.1. PSDs with time during CuNPs dissolution in 0.5 M HCl. Time (minutes) is shown in each PSD plot. It should be noted the data are presented in terms of size bins and reported as $dN/d\log D_p$ versus $\log D_p$, where N is the number concentration of particles and D_p is the particle diameter.

analyzed for comparison (Figure 8.2). These results indicate the copper sample completely dissolved, and the small signal observed after 30 minutes was due to particles formed from the copper ions during the generation of the aerosol.

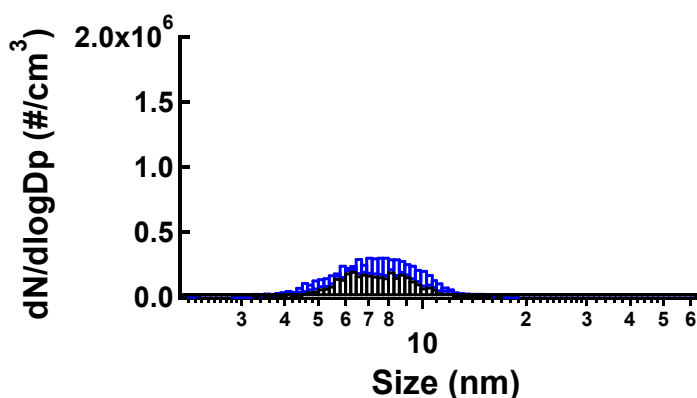
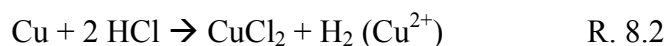
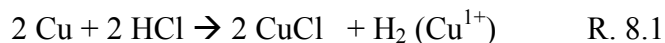
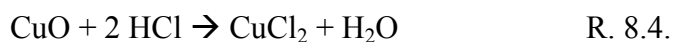


Figure 8.2 ES-SMPS PSD data for CuNPs in 0.5 M HCl after 30 minutes (black) and 1 wt % Cu ion standard solution (blue).

Reactions of copper metal with HCl



are not energetically favorable, but copper oxides are known to react according to



An inductively coupled plasma optical emission spectrometer was used to verify the

concentration of copper ions (Figure 8.3). The ICP/OES analysis confirmed complete dissolution of the CuNPs via detection of copper as solution phase ions. The ICP/OES data was compared with the ES-SMPS data using the peak maxima of the PSDs at each time to calculate the particle volume and the percent copper dissolved. Clean water and water with CuNPs removed were also analyzed to confirm no CuNPs were detected as ions. The results for percent copper dissolved using both methods agree well. However, the ES-SMPS data provide additional information about polydispersity and multimodal PSDs that cannot be extracted from analytical data that represent ion concentration.

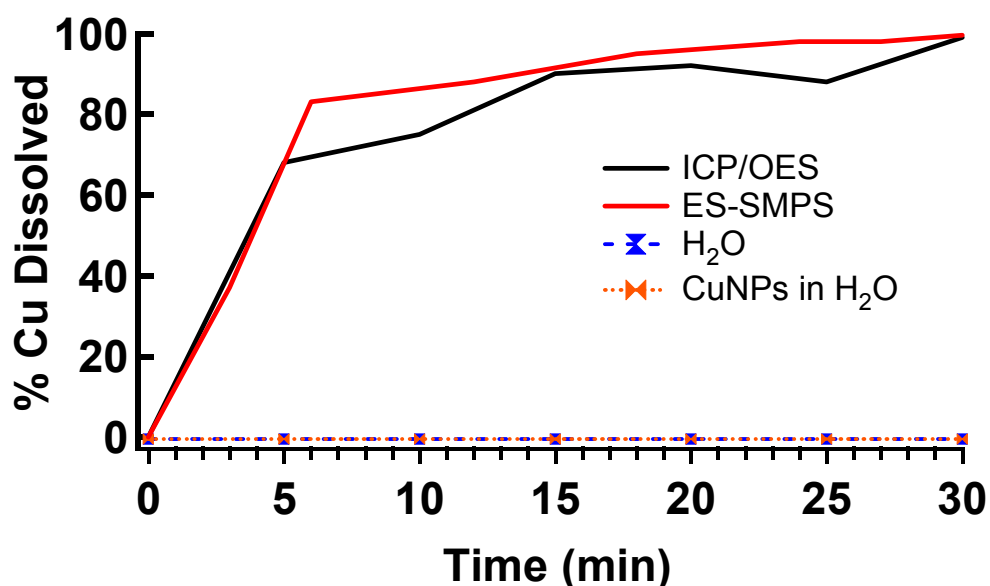


Figure 8.3 Percent copper dissolved with time based on ICP/OES analysis (black) and ES-SMPS data (red). Water and water with CuNPs removed are shown to confirm no CuNPs were detected as ions.

PSD data for the CuNPs in 0.5 M HCl are shown as an example, since similar multimodal results were seen with 0.25–0.75 M HCl, with faster dissolution rates for higher acid concentrations. At 0.5 M HCl, the acid is in excess for all potential reactions with copper and copper oxide layers (R. 8.1-8.4), and local concentration variations during dissolution are negligible. In solutions ≥ 0.75 M HCl, dissolution occurred so quickly that no PSD was observed after 1 or 2 scans. Solutions < 0.25 M did not completely dissolve the CuNPs, and solutions < 0.01 showed no change relative to the initial CuNP PSD.

Although these data are complex and not fully understood, it is clear that the smallest nanoparticles, less than 5 nm, dissolve at a faster rate compared to larger nanoparticles. This inherently faster dissolution of the smallest nanoparticles may be a result of a decrease in crystallinity at the surface for smaller particles, as it has been shown that ZnS nanoparticles ca. 3 nm are structurally disordered at the surface¹⁶⁷. Since crystallinity impacts dissolution with less crystalline materials dissolving at faster rates, this may explain some aspects of the data presented here.

8.4 Conclusions

In summary, measurements of PSDs can be used to monitor the initial primary particle size distributions and dissolution all the way to the complete formation of ions. To our knowledge, this work is the first experimental study to investigate nanoparticle dissolution via direct particle detection. The ES-SMPS approach can be used with a variety of nanoparticles (bare, coated, functionalized, monodisperse, polydisperse, aggregated, isolated) and a range of solvents (neutral, acidic, basic, high ionic strength), but may be limited to specific nanoparticle and solution concentrations. Advantages of

using the ES-SMPS to monitor nanoparticle dissolution include real-time analysis, small sampling volume, detection of the full nanosize range (~2–160 nm), and direct observation of polydispersity, including unique dissolution behavior such as bi- or tri-modal distributions and changes in particle number concentration. Thus, these experimental data, the first of its kind, provide insight into particle size effects on the nanoscale during dissolution.

8.5 Acknowledgements

Although the research described in this article has been funded wholly or in part by the Environmental Protection Agency through grant number EPA R83389101-0 to VHG, it has not been subjected to the Agency's required peer and policy review and therefore does not necessarily reflect the views of the Agency and no official endorsement should be inferred. This research was also supported in part by the Department of Defense (DoD) through the National Defense Science & Engineering Graduate Fellowship (NDSEG) Program and by the Center for Health Effects of Environmental Contamination. CRIF equipment grant 0639096 from the National Science Foundation is also gratefully acknowledged.

CHAPTER 9

COPPER-BASED NANOPARTICLE TRANSITION TO PARATACAMITE
NANOPARTICLES USING HYDROCHLORIC ACID9.1 Introduction

Metal nanoparticles are among the most common manufactured nanomaterials⁴ and, as such, are the subject of environmental and health studies to understand transformation and fate of synthetic nanoscale materials. Copper nanoparticles are of particular interest due to recent studies indicating higher toxicity relative to other manufactured metal nanomaterials^{162, 168, 169}. It is well known that toxicity of copper and copper oxides can be related to pH^{170, 171}, with copper sensitive ecological and biological environments known to exist in extreme acidic conditions, $\text{pH} < 2$ ¹⁷²⁻¹⁷⁴. Therefore, copper nanoparticle transformation must be considered in acidic pH conditions. Results can provide information on conditions that do not influence the particles, conditions that induce transformation, and the nature and degree of the transformations (i.e. size, shape, composition, chemical state, etc.). Previous work considered copper nanoparticles in low pH conditions capable of complete dissolution (submitted). The work presented here considers copper nanoparticles in low pH conditions that do not cause dissolution, but do cause particle transformation in size and chemical composition. Specifically, copper nanoparticles with an oxidized shell are shown to transition to paratacamite nanoparticles in hydrochloric acid solutions within a narrow concentration range. Paratacamite, $\gamma\text{-Cu}_2(\text{OH})_3\text{Cl}$, is a pale green copper chloride hydroxide that is normally prepared from copper chloride salts under basic conditions (vide infra).

$\text{Cu}_2(\text{OH})_3\text{Cl}$ occurs as four polymorphs, paratacamite (rhombohedral), atacamite (orthorhombic), batallackite (monoclinic), and clinoatacamite (monoclinic)^{175, 176}. These

basic copper chloride minerals occur naturally as a result of corrosion on copper-containing structures, referred to as “bronze disease”¹⁷⁷. There is a great deal of interest in these minerals for a number of chemically interesting yet quite distinct reasons. A body of literature has focused on the structures and properties of $\text{Cu}_2(\text{OH})_3\text{Cl}$ minerals due to their role in the degradation of ancient artifacts¹⁷⁷⁻¹⁷⁹. More recently, paratacamite has received attention as the active species in the heterogeneous catalysis of dimethyl carbonate (DMC) and diethyl carbonate (DEC) synthesis¹⁸⁰⁻¹⁸². As potentially green solvents, DMC/DEC application areas include advantages as non-toxic solvents, methylation and carbonylation agents, and fuel/lube additives^{180, 182-184}. More recently, as nanostructured aggregates, paratacamite has been noted for its performance in the reversible uptake and storage of hydrogen¹⁸⁵.

Paratacamite is a double salt, composed of the two simple salts CuCl_2 and $\text{Cu}(\text{OH})_2$ in a 1:3 ratio. It is typically prepared by addition of a hydroxide (NaOH, KOH) to aqueous copper chloride¹⁸⁶. The composition and phase of the resulting copper chloride hydroxide is sensitive to the Cu:OH ratio, heat treatment, and stirring^{180, 181, 186, 187}. Paratacamite is the most thermodynamically stable phase in ambient temperatures, and metastable phases of $\text{Cu}_2(\text{OH})_3\text{Cl}$ will recrystallize to paratacamite at ambient conditions¹⁸⁷.

In this work, the unique formation of paratacamite in acidic conditions is reported. Copper-based nanoparticles are transformed into paratacamite nanoparticles by addition of HCl in ambient conditions. The resulting paratacamite nanoparticles are ~8.5 nm in diameter. To our knowledge, this is the first report of paratacamite on the nanoscale, < 100 nm.

9.2 Experimental Methods

9.2.1 Materials Copper nanoparticles (~15 nm) were purchased in powder form from Nanostructured and Amorphous Materials, Inc.(Houston, TX). Copper microparticles (~10 μm) were purchased from Alfa Aesar (Ward Hill, MA). Aqueous hydrochloric acid solutions (0.025 M, 0.05 M, 0.075M, and 0.1 M) were added to copper samples at 1 wt % Cu in ambient conditions (~22 °C) and sonicated ~ 10 seconds to suspend the particles. Unless otherwise noted, samples were allowed to set overnight without stirring, and the resulting powder was collected by vacuum aspiration for analysis.

9.2.2 Electro Spray-Scanning Mobility Particle Sizer The suspended copper nanoparticles were analyzed immediately following addition of HCl. An electro spray atomizer coupled to a scanning mobility particle sizer (ES-SMPS) is used to investigate the particle size distributions (PSD) of the nanoparticles during reaction. Experimental methods using the ES-SMPS were discussed in detail previously¹⁸⁸. Briefly, the electro spray generates an aerosol from a nanoparticle suspension, and the aerosol flows through a diffusion dryer. Dry particles enter the SMPS for size classification and particle counting to produce a particle size distribution. Particle size is determined based on mobility diameter, D_p . It should be noted that the data are shown in terms of bin and reported as, $dN/d\log D_p$ versus $\log D_p$. Scans were collected at ~5 minute intervals for 40 minutes to monitor transitions in PSD in real time. Beyond 40 minutes, the PSD did not show continued transition, as monitored for an additional two hours.

9.2.3 High-Resolution Transmission Electron Microscopy A JEOL JEM 2100F with the field emission gun operating at 200 kV was used to acquire TEM images of the copper nanoparticles before and after reaction in 0.1 M HCl. TEM grids were purchased

from Ted Pella, Inc. (Redding, CA) as Formvar/Carbon 200 Mesh Nickel Grids. Samples were prepared for TEM analysis by sonication in methanol for 5 minutes, followed by deposition onto the TEM grids using a pipette.

9.2.4 Powder X-ray Diffraction A Siemens D5000 X-ray diffractometer with Cu K α target and nickel filter was used to collect a XRD powder pattern for the copper nanoparticle and microparticle samples before and after exposure to HCl solutions.

9.3 Results and Discussion

9.3.1 Electrospray-Scanning Mobility Particle Sizer The particle size of the copper nanoparticles suspended in water was analyzed using the ES-SMPS, and is referred to as the initial sample. The PSDs were monitored for copper nanoparticles in each HCl solution, and the final PSDs are shown in Figure 9.1. There is a shift to smaller sizes with increased HCl concentration, with a ~6 nm difference between the initial sample and the final 0.1 M HCl PSD. At the highest HCl concentration, 0.1 M HCl, the reaction time was 40 minutes with a shift from 14.6 nm particles to 8.5 nm particles. The change in particle volume with time at 0.1 M HCl is shown in Figure 9.2. These data do not simply represent a decrease in solid copper content, since the resulting particles are not copper, as discussed in detail in the next section, but these data do clearly show the endpoint for the reaction.

9.3.2 Copper Color Transitions in Hydrochloric Acid Solutions The color of the nanoparticle suspensions varied with HCl concentration (Figure 9.3). The initial sample was a black suspension due to the black color of the copper nanoparticle powder. Suspensions in acid concentrations below 0.025 M were black but changed to brown for acid concentrations in the range of 0.025 M < 0.1 M. The suspension at 0.1 M was a pale

green color. When complete dissolution into copper ions has occurred, the solution is a pale blue, as shown in Figure 3 for the 0.5 M sample. The color changes suggest a chemical reaction, and further analysis was performed to investigate the chemical composition of the samples.

The powder samples were filtered from the HCl solutions for both nanoscale and microscale copper. The color of the powder for both copper samples at each acid concentration is shown in Figure 9.4. The color of the microscale copper changed from orange in water to brown in acid but did not vary with acid concentration. The color of the nanoscale copper varied with acid concentration and is consistent with the color of the suspensions.

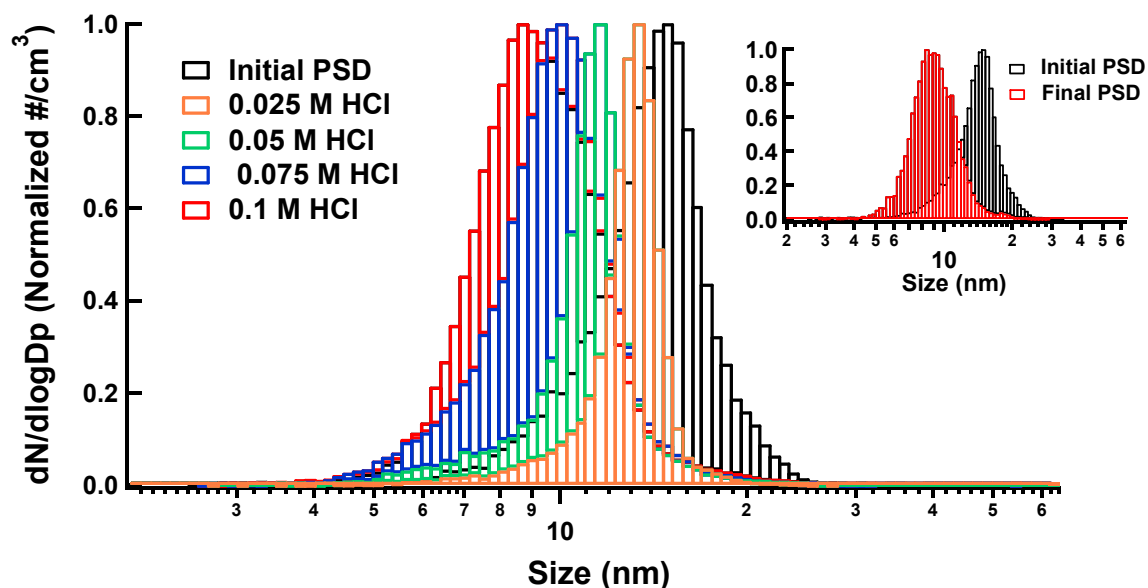


Figure 9.1 ES-SMPS particle size distributions for copper nanoparticles in 0 M HCl (initial), 0.025 M HCl, 0.05 M HCl, and 0.1 M HCl. The inset compares the initial (0 M HCl) and final (0.1 M HCl) PSDs.

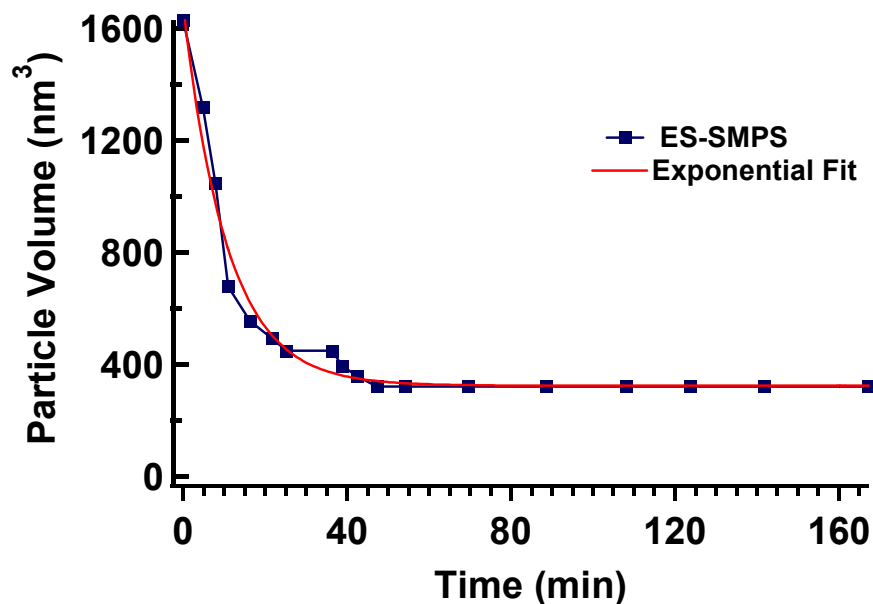


Figure 9.2 Particle volume versus reaction time for copper nanoparticles reacted in 0.1 M HCl. Volumes are based on the diameter of the peak maximum of the PSDs with time.

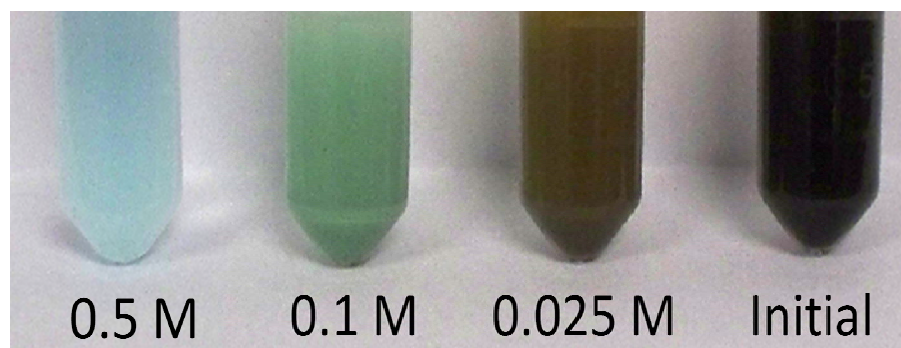


Figure 9.3 Sample color for copper nanoparticles in HCl during ES-SMPS analysis. Initial, 0.025 M, and 0.1 M samples are suspensions of particles in HCl, and 0.5 M sample with copper ions dissolved in HCl is shown for comparison.

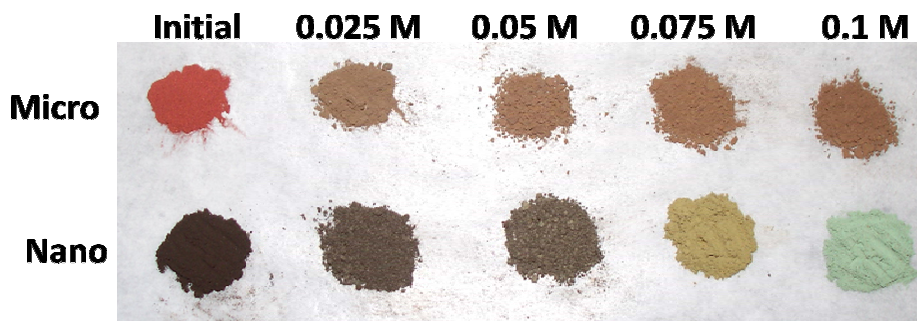


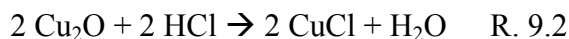
Figure 9.4 Sample color for powders collected after reaction of nanoscale and microscale copper particles with HCl solutions.

9.3.3 High-Resolution Transmission Electron Microscopy TEM images of the initial copper nanoparticle sample show highly aggregated particles that appear to be ~ 12-15 nm (Figure 9.5a). TEM images of the sample after reaction in 0.1 M HCl show isolated particles that are 5-10 nm (Figure 9.5b). These sizes agree with results from ES-SMPS analysis. The HCl reacted sample also shows very large particles with a highly organized, rectangular structure (Figure 9.5c). Increased magnification reveals these structures are composed of the < 10 nm particles. The existence of these rectangular nanostructured particles is unique to the HCl reacted sample and was not seen for the initial copper nanoparticles.

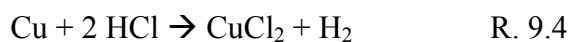
9.3.4 Powder X-ray Diffraction The bulk chemical composition of the powder samples was analyzed with powder XRD. Figure 9.6 shows the initial copper samples compared with copper metal, copper (I) oxide (Cu_2O), and copper (II) oxide (CuO) references. The microscale copper is pure copper metal with a small but detectable amount of Cu_2O . The nanoscale copper consists of copper metal, Cu_2O , and CuO . The intensity of the peaks indicates a greater CuO content relative to Cu_2O . The bulk chemical composition of the samples following reaction with HCl is shown in Figure 9.7. The upper set of spectra

show results for the nanoscale copper sample, with copper metal, Cu₂O, CuO, and paratacamite (γ -Cu₂(OH)₃Cl) references¹⁸⁹. At the lowest acid concentration, 0.025 M, the data show the presence of paratacamite and CuO, but there is no copper metal or Cu₂O present. As the acid concentration increases to 0.05 M, the paratacamite and Cu₂O content increase, while the CuO content decreases. At 0.075 M, the paratacamite content continues to increase, but the CuO and Cu₂O content decrease. At 0.1 M, the sample is paratacamite with a small amount of Cu₂O detected. In all samples, there is no copper metal detected. The peak at 17.4° is a small amount of the Cu₂(OH)₃Cl polymorph atacamite¹⁸⁹. The lower set of spectra in Figure 9.7 show results for the microscale copper sample with references. The microscale copper sample shows copper metal at all acid concentrations and no paratacamite. There is a small amount of Cu₂O but no CuO. The peaks at 28.4° and 47.3° are CuCl¹⁹⁰.

The XRD data show unique behavior for the nanoscale copper particles in the same chemical environment as the microscale particles. The microscale sample remains copper upon mixing with HCl solutions, while the nanoscale sample reacts to form a new compound. This is likely due to increased oxidation of the nanoparticles. Copper (II) and copper (I) oxides can react with HCl to produce copper (II) and copper (I) chlorides:



Reactions of copper metal with HCl



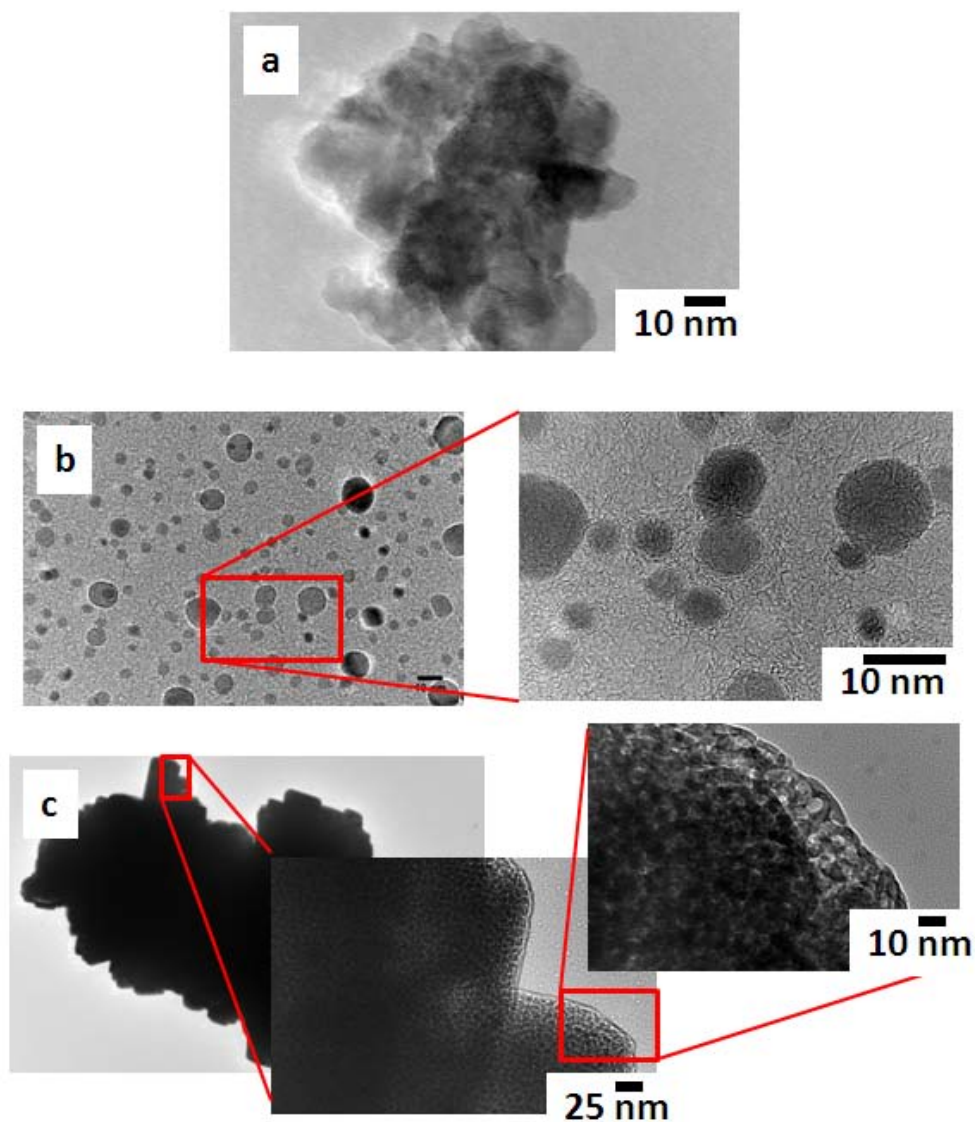


Figure 9.5 TEM images of the initial copper nanoparticles (a) and 0.1 M HCl reacted particles showing isolated nanoparticles (b) and rectangular nanostructured aggregates (c).

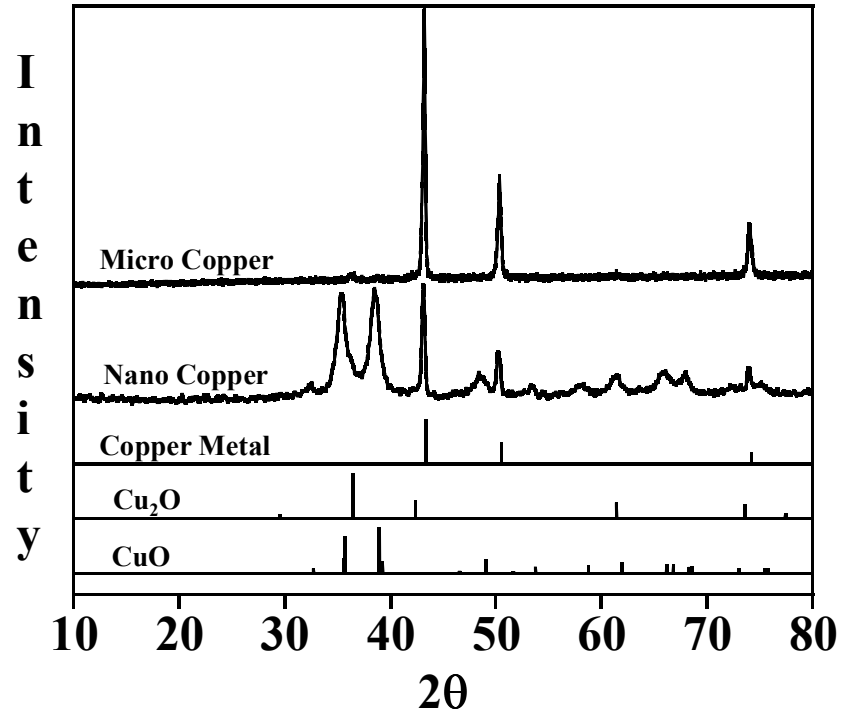


Figure 9.6 Powder XRD of initial nanoscale and microscale copper samples. Copper metal and copper oxides are shown for reference.

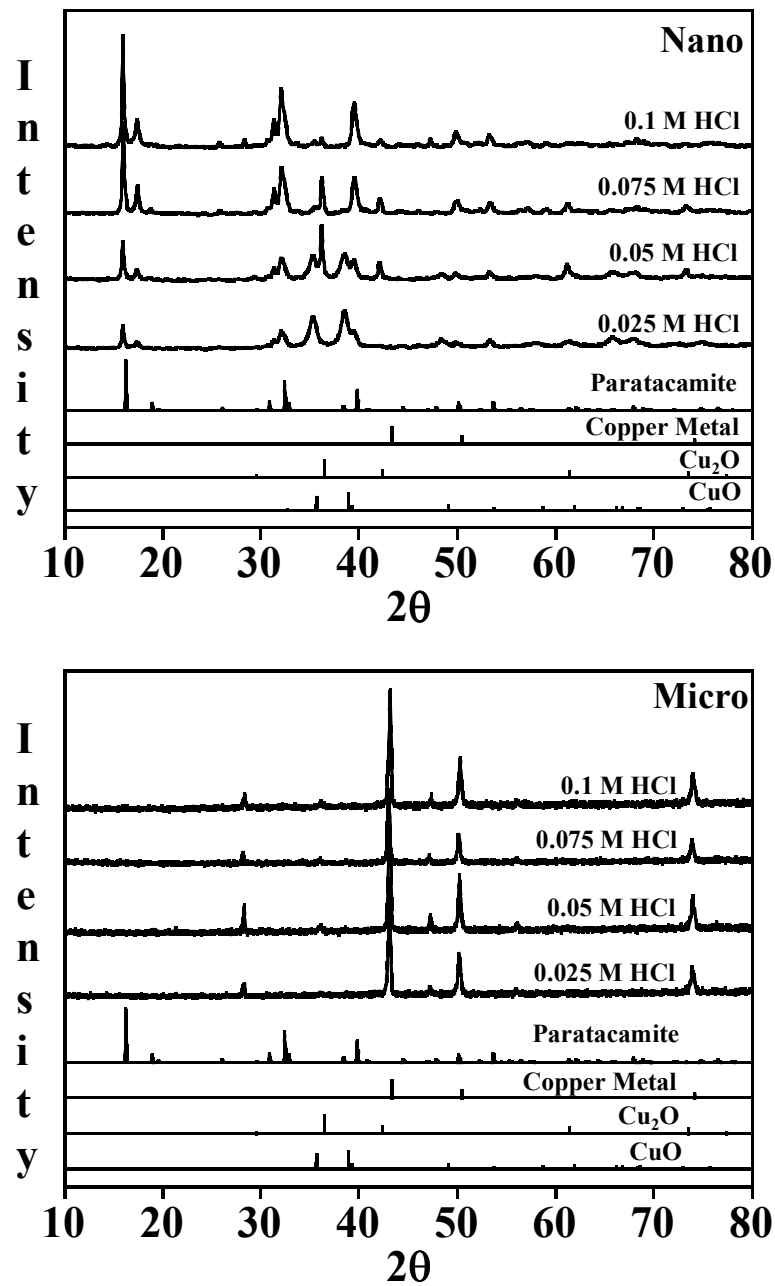
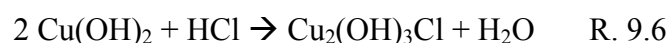


Figure 9.7 Powder XRD for nanoscale copper (upper) and microscale copper (lower) after reaction with HCl solutions. Copper metal, copper oxides, and the copper chloride hydroxide mineral paratacamite are shown for reference.

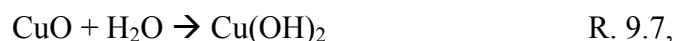
are not energetically favorable. Therefore, the oxide layers of the nanoscale copper could promote reactions with HCl that produce the copper chloride required to facilitate paratacamite formation. Although XRD patterns of the microscale copper show copper chloride, the copper metal was maintained, indicating little of the copper was liberated for further reactions. Typically, reactions of copper chloride leading to paratacamite formation involve a hydroxide (NaOH, KOH), according to



where subsequent reaction of copper hydroxide with HCl can form paratacamite as



The source of such a OH⁻ donor in the reaction containing copper samples, hydrochloric acid, and water, is unclear. It is unlikely that water is donating OH⁻ to form copper hydroxide



which could react according to R. 9.6 to form paratacamite, since no copper hydroxide was seen in the XRD pattern for the copper samples in water.

Another possible mechanism is formation of Cu₂(OH)₃Cl without copper chloride. Such a mechanism would support the absence copper chloride in the nanoscale XRD patterns, and account for the presence of copper chloride without formation of Cu₂(OH)₃Cl in the microscale XRD patterns. Figure 9.8 shows a possible route for Cu₂(OH)₃Cl formation that involves only the species present in the initial reaction mixture: copper nanoparticles, water, and hydrochloric acid.

Assuming the surface to be CuO, the surface may be hydrated and induced Cu(OH)₂ can exist on the particle surface due to association with water (Figure 9.8a). The HCl can

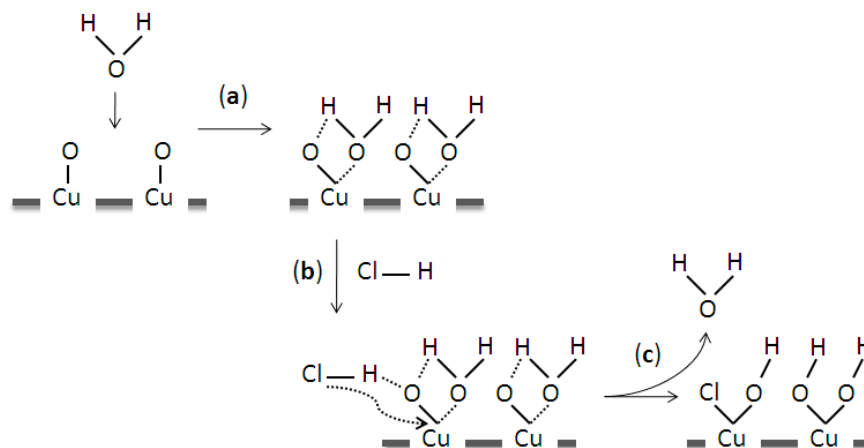


Figure 9.8 Possible mechanism of paratacamite formation in aqueous HCl solution on the copper-based nanoparticle surface.

react with the surface $\text{Cu}(\text{OH})_2$ species (Figure 9.8b) to form $\text{Cu}_2(\text{OH})_3\text{Cl}$ and water (Figure 9.8c). Figure 9.8 is a linear representation based on the stoichiometry of R. 9.6, as the crystalline structure of paratacamite is known to consist of copper coordinated as $\text{Cu}(\text{OH})_4\text{Cl}_2$ and $\text{Cu}(\text{OH})_6$ octahedra units¹⁸⁰. This mechanism is consistent with the XRD data and reaction conditions, as it does not rely on production of $\text{CuCl}/\text{CuCl}_2$ and solid phase $\text{Cu}(\text{OH})_2$ prior to $\text{Cu}_2(\text{OH})_3\text{Cl}$ formation, nor does it require addition of a base.

9.4 Conclusions

This study investigated properties of copper/copper oxide nanoparticles exposed to aqueous hydrochloric acid conditions. The nanoparticles were shown to shift to a smaller particle size and transition to a new chemical compound, paratacamite. XRD patterns showed a continued increase in paratacamite content and decrease in CuO followed by an initial increase then decrease in Cu_2O with HCl concentration. Comparison with micron-sized copper particles showed the larger particles did not have surface oxide layers and

retained the copper metal composition upon exposure to HCl at all concentrations. Future work is underway to determine if copper nanoparticles without surface oxide layers will react to produce paratacamite.

9.5 Acknowledgements

Although the research described in this article has been funded wholly or in part by the Environmental Protection Agency through grant number EPA R83389101-0 to VHG, it has not been subjected to the Agency's required peer and policy review and therefore does not necessarily reflect the views of the Agency and no official endorsement should be inferred. This research was also supported in part by the Department of Defense (DoD) through the National Defense Science & Engineering Graduate Fellowship (NDSEG) Program and by the Center for Health Effects of Environmental Contamination.

CHAPTER 10

CONCLUSIONS AND FUTURE DIRECTIONS

The work presented here consists of characterization of manufactured and synthetic nanomaterials to understand fundamental properties, an environmental application of nanomaterials, and evaluation or design of approaches/methods for analyzing nanomaterials for environmental, health, and safety studies. The methods used and the results published from these investigations can be applied to future work towards understanding and facilitating the safe application of nanomaterials for a variety of technologies.

Chapter 3 outlined and discussed the suite of bulk and surface techniques used for the analyses. Future work in nanomaterial characterization will likely include additional techniques as they become available at The University of Iowa. For example, the new Hi-Resolution TEM recently acquired by the Central Microscopy Research Facility will greatly enhance imaging and elemental analysis capabilities at the nanoscale, particularly < 10 nm. Such data will be especially insightful with regard to nanoparticle bulk/surface composition distinction. The ES-SMPS system can be modified with additional components to expand its analysis capabilities. Adding a second Classifier/DMA to the system immediately upstream of the existing Classifier/DMA (see Figure 3.2) would enable size-selecting for controlled studies of a specific nanoparticle size. Introduction of a gas-phase reaction zone would allow heterogeneous chemistry studies of nanoparticle aerosol/gas-phase reactions. Such analysis would be useful for atmospheric processing studies.

Chapter 4 presented collaborative studies consisting of the characterization of manufactured and synthetic nanomaterials. Carbon nanotube characterization evaluated

specific surface area, diameter distributions, conductivity, and contamination in preparation for toxicology inhalation experiments. The characterization was sufficient to determine the CNTs were adequate for toxicology studies, and future characterization for such studies can be performed using these techniques, or any combination of techniques outlined in Chapter 3 to acquire the desired property information.

Titanium dioxide and polymer-coated silver nanoparticle characterization used ES-SMPS analysis to determine particle size distributions as part of an investigation of nanoparticle aerosol generation methods. Future directions for method analysis should consider the application of the method (i.e., inhalation toxicology, for the study presented here) and determine criteria for acceptance based on the important factors related to the application. Studies investigating the application of methods for nanoparticle research can contribute to a database or consensus that specific methods are best suited to particular applications, and the selected method may vary based on the properties of the nanomaterial under consideration.

Polymer-coated silver nanoparticle characterization used the ES-SMPS coupled with TEM to measure polymer coating thickness. This coupled approach can be used in the future for any variety of organic-coated nanoparticles for accurate determination of coating thickness. Numerous nanoparticle applications are designed with surface coatings, and these coatings may account for large percentage of the total particle size, therefore, it is critical to have a method available to accurately analyze coating thickness. In general, coupled approaches counteract the limitations of one or more techniques by pairing them with the strengths of a counter technique. Since many analytical techniques operate on different principles and may encounter unique challenges on the nanoscale,

nanomaterial characterization is an area of research that will likely utilize coupled approaches to maximize property data.

Gold nanoparticle characterization used the ES-SMPS to investigate changes in particle size due to particle-solution interactions. Future work in this investigation needs to examine larger gold nanoparticles for a sufficient distinction between the nanoparticle PSD and the salt background. This is necessary so shifts in the nanoparticle PSD can be definitively attributed to the thickness of the citrate DL. This data would verify a new application of the ES-SMPS system for DL thickness determination. Future studies could consider different nanoparticles with a variety of surface compositions in various aqueous solutions to establish the broad applicability of the ES-SMPS for DL thickness measurements.

Chapter 5 presented a study on airborne monitoring to distinguish engineered nanomaterials from incidental particles for environmental health and safety. This study used TEM/EDX and SEM to correlate chemical composition with particle size and shape for lithium titanate nanomaterial collected on filters at a manufacturing facility. A second method used particle number and mass concentration, along with worker activity logs, to identify specific activities that correlate increased exposure to particles in the respirable range. This study effectively demonstrates the strengths of the two methods and how they fit together to provide a complete picture of worker exposure to airborne particles in an occupational setting. In the future, other facilities can use these same methods in combination to distinguish engineered nanomaterials from incidental particles, identify the elemental composition of airborne particles, and identify activities

that pose the greatest exposure risk for workers. This information is useful in selecting the required personal protective equipment and process enclosure/ventilation.

In Chapter 6, an investigation of selective catalytic reduction of NO_2 with ammonia using nanocrystalline NaY and CuY zeolites was presented. Results showed unique adsorption sites for the reactants on the nanocrystalline zeolites compared with the micron-sized sample. The nanocrystalline samples also showed enhanced rates for loss of NO_2 from the gas-phase. This study did not consider the effects of oxygen and water on the reaction rate and the adsorbed species. Future work could focus on these effects, and their temperature dependence, which may lead to a decrease in NO_3^- remaining on the nanocrystalline zeolite surface and facilitate degradation of the ammonium nitrate intermediate.

The state of silver nanoparticles in aqueous environments was presented in Chapter 7. The states of agglomeration, isolation of primary particles, and dissolution in neutral and aqueous nitric acid solutions were identified using the ES-SMPS, with TEM, ICP, and zeta potential as complementary analyses. The techniques used in this study could be applied to a variety of nanoparticles and solution media for environmentally or biologically relevant data. Since nanoparticles are being developed for a range of environmental applications, it is relevant to consider these nanoparticles the full pH range, as well as conditions that simulate ground water, waste water, etc. Nanoparticles are also being developed for therapeutic applications; therefore, it is relevant to consider conditions that simulate the blood stream, stomach acid, lung fluid, etc. The results in Chapter 7 show the ES-SMPS can provide useful data for such investigations.

Chapter 8 introduced a novel approach for investigating nanoparticle dissolution from

the particle perspective based on particle sizing measurements. This study used the ES-SMPS to monitor PSDs in real time to observe the decrease in mobility diameter as copper nanoparticles dissolved in hydrochloric acid. This application of the ES-SMPS can be used to provide insights into changes in particle size during chemical processes that may not be obtained from conventional methods. This could be particularly useful when the size of the nanoparticles is critical, such as studies considering transport and translocation of nanoparticles, where small changes in size may dictate how the particles are able to move in the environment or where they can pass in living organisms.

Chapter 9 presented the results of copper nanoparticle transition to paratacamite nanoparticles using hydrochloric acid. This study used the ES-SMPS to monitor particle size changes during reaction, and powder x-ray diffraction was used to identify the crystalline structure of copper nanoparticles exposed to varying concentrations of hydrochloric acid and compare them with micron-sized copper particles. These results demonstrate the unique chemical reactivity that nanoparticles can display relative to particles of larger size, and point toward the continued need for a full characterization of nanomaterials in a variety of chemical environments.

Nanoscience and nanotechnology offer new opportunities for developing advanced materials for use in industrial, environmental, and health applications. The continual need for risk assessment of manufactured nanomaterials is necessary to ensure safety of workers in occupational settings, health of the general public, and environmental habitats and ecosystems. Due to changes in physical and chemical properties of nanomaterials, there needs to be an assessment of the classical approaches used to investigate the properties and toxicity of materials to establish methods that are applicable for

nanomaterial-based products. Important correlations between physicochemical properties with biological responses can only be accomplished through collaboration of investigators in different scientific disciplines. This approach is interdisciplinary by nature, and it is evident that a research team approach is needed to tackle these issues.

Current knowledge base on the risks associated with nanomaterials is growing due an increase in the number of nanomaterial-based consumer products becoming commercially available. Databases are being compiled to provide accessible information on the most recent nanoscale scientific data. These databases include International Council on Nanotechnology (ICON) (Rice University), Project on Emerging Nanotechnologies (Woodrow Wilson International Center), Nanoparticle Information Library (NIOSH), Nanoscale Science and Engineering Center (University of Wisconsin, Madison), SAFENANO (Institute of Occupational Medicine) and Nanomedicine Research Portal. The application of nanoscience and nanotechnology in devices, equipment, and consumer products is predicted to maintain substantial growth in the next 10 years and beyond. Along with this growth, it is clear there are concerns and questions that need to be addressed and answered related to the potential impact nanotechnology will have on the environment, living organisms and human health. The work presented in this thesis contributes to the growing body of knowledge that will enable the environmental and health impacts of nanoscience and nanotechnology to be understood, and therefore properly controlled.

REFERENCES

1. In *ASTM International Committee E56 on Nanotechnology. ASTM E2456-06 Standard Terminology for Nanotechnology is available at www.astm.org.*
2. Erik, L.; Shawn, D.; Abbas, K.; Adam, S.; Shawn, F.; Aldo, P.; Weifeng, L.; Corrie, C.; Kenneth, J. K., Nanocrystalline Metal Oxides as Unique Chemical Reagents/Sorbents. *Chemistry - A European Journal* **2001**, 7, (12), 2505-2510.
3. Woodrow Wilson International Center for Scholars, Project on Emerging Nanotechnologies, Inventories: Consumer Products. <http://www.nanotechproject.org/> (January 20, 2010).
4. Maynard, A. D. *Nanotechnology: A research strategy for addressing risk*; Woodrow Wilson International Center for Scholars: 2006.
5. Oberdorster, G.; Maynard, A.; Donaldson, K.; Castranova, V.; Fitzpatrick, J.; Ausman, K.; Carter, J.; Karn, B.; Kreyling, W.; Lai, D.; Olin, S.; Monteiro-Riviere, N.; Warheit, D.; Yang, H., Principles for characterizing the potential human health effects from exposure to nanomaterials: elements of a screening strategy. *Part Fibre Toxicol* **2005**, 2, 8.
6. Guzman, K. A. D.; Taylor, M. R.; Banfield, J. F., Environmental risks of nanotechnology: National nanotechnology initiative funding, 2000-2004. *Environmental Science & Technology* **2006**, 40, (5), 1401-1407.
7. Borm, P.; Klaessig, F. C.; Landry, T. D.; Moudgil, B.; Pauluhn, J.; Thomas, K.; Trottier, R.; Wood, S., Research strategies for safety evaluation of nanomaterials, Part V: Role of dissolution in biological fate and effects of nanoscale particles. *Toxicological Sciences* **2006**, 90, (1), 23-32.
8. Phares, D. J.; Rhoads, K. P.; Johnston, M. V.; Wexler, A. S., Size-resolved ultrafine particle composition analysis - 2. Houston. *Journal of Geophysical Research: Atmospheres* **2003**, 108, (D7), 8420.
9. Bang, J. J.; Murr, L. E., Collecting and characterizing atmospheric nanoparticles. *Journal of the Minerals, Metals and Materials Society* **2002**, 54, (12), 28.
10. Brunner, T. J.; Wick, P.; Manser, P.; Spohn, P.; Grass, R. N.; Limbach, L. K.; Bruinink, A.; Stark, W. J., In Vitro Cytotoxicity of Oxide Nanoparticles: Comparison to Asbestos, Silica, and the Effect of Particle Solubility. *Environmental Science & Technology* **2006**, 40, (14), 4374-4381.
11. Agustina, T. E.; Ang, H. M.; Vareek, V. K., A review of synergistic effect of photocatalysis and ozonation on wastewater treatment. *Journal of Photochemistry and Photobiology C: Photochemistry Reviews* **2005**, 6, (4), 264-273.
12. Sunada, K.; Kikuchi, Y.; Hashimoto, K.; Fujishima, A., Bactericidal and Detoxification Effects of TiO₂ Thin Film Photocatalysts. *Environmental Science & Technology* **1998**, 32, (5), 726-728.

13. Borm, P. J. A., Particle Toxicology: From Coal Mining to Nanotechnology. *Inhalation Toxicology: International Forum for Respiratory Research* **2002**, 14, (3), 311 - 324.
14. Derfus, A. M.; Chan, W. C. W.; Bhatia, S. N., Probing the Cytotoxicity of Semiconductor Quantum Dots. *Nano Letters* **2003**, 4, (1), 11-18.
15. Hardman, R., A Toxicologic Review of Quantum Dots: Toxicity Depends on Physicochemical and Environmental Factors. *Environmental Health Perspectives* **2006**, 114, (2), 156.
16. Rebitzer, G.; Ekvall, T.; Frischknecht, R.; Hunkeler, D.; Norris, G.; Rydberg, T.; Schmidt, W. P.; Suh, S.; Weidema, B. P.; Pennington, D. W., Life cycle assessment: Part 1: Framework, goal and scope definition, inventory analysis, and applications. *Environment International* **2004**, 30, (5), 701-720.
17. Balbus, J. M.; Maynard, A. D.; Colvin, V. L.; Castranova, V.; Daston, G. P.; Denison, R. A.; Dreher, K. L.; Goering, P. L.; Goldberg, A. M.; Kulinowski, K. M.; Monteiro-Riviere, N. A.; Oberdörster, G.; Omenn, G. S.; Pinkerton, K. E.; Ramos, K. S.; Rest, K. M.; Sass, J. B.; Silbergeld, E. K.; Wong, B. A., Meeting Report: Hazard Assessment for Nanoparticles—Report from an Interdisciplinary Workshop *Environmental Health Perspectives* **2007**, 115, (11), 1654.
18. Schins, R. P. F.; Duffin, R.; Hohr, D.; Knaapen, A. M.; Shi, T.; Weishaupt, C.; Stone, V.; Donaldson, K.; Borm, P. J. A., Surface Modification of Quartz Inhibits Toxicity, Particle Uptake, and Oxidative DNA Damage in Human Lung Epithelial Cells. *Chemical Research in Toxicology* **2002**, 15, (9), 1166-1173.
19. Osier, M.; Oberdorster, G., Intratracheal Inhalation vs Intratracheal Instillation: Differences in Particle Effects. *Toxicol. Sci.* **1997**, 40, (2), 220-227.
20. Oberdorster, G.; Sharp, Z.; Atudorei, V.; Elder, A.; Gelein, R.; Kreyling, W.; Cox, C., Translocation of Inhaled Ultrafine Particles to the Brain. *Inhalation Toxicology* **2004**, 16, (6-7), 437-445.
21. Donaldson, K.; Aitken, R.; Tran, L.; Stone, V.; Duffin, R.; Forrest, G.; Alexander, A., Carbon Nanotubes: A Review of Their Properties in Relation to Pulmonary Toxicology and Workplace Safety. *Toxicol. Sci.* **2006**, 92, (1), 5-22.
22. Lam, C.-W.; James, J. T.; McCluskey, R.; Hunter, R. L., Pulmonary Toxicity of Single-Wall Carbon Nanotubes in Mice 7 and 90 Days After Intratracheal Instillation. *Toxicol. Sci.* **2004**, 77, (1), 126-134.
23. Poland, C. A.; Duffin, R.; Kinloch, I.; Maynard, A.; Wallace, W. A. H.; Seaton, A.; Stone, V.; Brown, S.; MacNee, W.; Donaldson, K., Carbon nanotubes introduced into the abdominal cavity of mice show asbestos-like pathogenicity in a pilot study. *Nat Nano* **2008**, 3, (7), 423-428.

24. Grassian, V. H.; Adamcakova-Dodd, A.; Pettibone, J. M.; O'Shaughnessy, P. T.; Thorne, P. S., Inflammatory response of mice to manufactured titanium dioxide nanoparticles: Comparison of size effects through different exposure routes. *Nanotoxicology* **2007**, 1, (3), 211-226.
25. Maynard, A.; Kuempel, E., Airborne Nanostructured Particles and Occupational Health. *Journal of Nanoparticle Research* **2005**, 7, (6), 587-614.
26. Pastorin, G.; Kostarelos, K.; Prato, M.; Bianco, A., Functionalized Carbon Nanotubes: Towards the Delivery of Therapeutic Molecules *Journal of Biomedical Nanotechnology* **2005**, 1, (2), 133.
27. Bianco, A.; Kostarelos, K.; Prato, M., Applications of carbon nanotubes in drug delivery. *Current Opinion in Chemical Biology* **2005**, 9, (6), 674-679.
28. Peng, X.; Li, Y.; Luan, Z.; Di, Z.; Wang, H.; Tian, B.; Jia, Z., Adsorption of 1,2-dichlorobenzene from water to carbon nanotubes. *Chemical Physics Letters* **2003**, 376, (1-2), 154-158.
29. In *US Environmental Protection Agency. Nanotechnology White Paper. 2007.*
30. Muller, J.; Huaux, F.; Lison, D., Respiratory toxicity of carbon nanotubes: How worried should we be? *Carbon* **2006**, 44, (6), 1048-1056.
31. Iijima, S., Helical microtubules of graphitic carbon *Nature* **1991**, 354, (7), 56.
32. Peng, Y.; Liu, H., Effects of Oxidation by Hydrogen Peroxide on the Structures of Multiwalled Carbon Nanotubes. *Industrial & Engineering Chemistry Research* **2006**, 45, (19), 6483-6488.
33. Rosca, I. D.; Watari, F.; Uo, M.; Akasaka, T., Oxidation of multiwalled carbon nanotubes by nitric acid. *Carbon* **2005**, 43, (15), 3124-3131.
34. Yang, D.-Q.; Rochette, J.-F.; Sacher, E., Functionalization of Multiwalled Carbon Nanotubes by Mild Aqueous Sonication. *The Journal of Physical Chemistry B* **2005**, 109, (16), 7788-7794.
35. Langley, L. A.; Villanueva, D. E.; Fairbrother, D. H., Quantification of Surface Oxides on Carbonaceous Materials. *Chemistry of Materials* **2005**, 18, (1), 169-178.
36. Heymann, D., Solubility of Fullerenes C₆₀ and C₇₀ in Seven Normal Alcohols and Their Deduced Solubility in Water. *Fullerene Science and Technology* **1996**, 4, (3), 509-515.
37. Lecoanet, H. F.; Bottero, J. Y.; Wiesner, M. R., Laboratory assessment of the mobility of nanomaterials in porous media. *Environmental Science & Technology* **2004**, 38, (19), 5164-5169.

38. Oberdorster, G., Toxicology of ultrafine particles: in vivo studies. *Philosophical Transactions of the Royal Society of London. Series A: Mathematical, Physical and Engineering Sciences* **2000**, 358, (1775), 2719-2740.
39. Sayes, C. M.; Wahi, R.; Kurian, P. A.; Liu, Y.; West, J. L.; Ausman, K. D.; Warheit, D. B.; Colvin, V. L., Correlating Nanoscale Titania Structure with Toxicity: A Cytotoxicity and Inflammatory Response Study with Human Dermal Fibroblasts and Human Lung Epithelial Cells. *Toxicol. Sci.* **2006**, 92, (1), 174-185.
40. Warheit, D. B.; Webb, T. R.; Sayes, C. M.; Colvin, V. L.; Reed, K. L., Pulmonary Instillation Studies with Nanoscale TiO₂ Rods and Dots in Rats: Toxicity Is not Dependent upon Particle Size and Surface Area. *Toxicol. Sci.* **2006**, 91, (1), 227-236.
41. Moss, O. R.; Wong, V. A., When Nanoparticles Get in the Way: Impact of Projected Area on In Vivo and In Vitro Macrophage Function. *Inhalation Toxicology* **2006**, 18, (10), 711-716.
42. Powers, K. W.; Palazuelos, M.; Moudgil, B. M.; Roberts, S. M., Characterization of the size, shape, and state of dispersion of nanoparticles for toxicological studies. *Nanotoxicology* **2007**, 1, (1), 42-51.
43. Sager, T. M.; Porter, D. W.; Robinson, V. A.; Lindsley, W. G.; Schwegler-Berry, D. E.; Castranova, V., Improved method to disperse nanoparticles for in vitro and in vivo investigation of toxicity. *Nanotoxicology* **2007**, 1, (2), 118-129.
44. Teeguarden, J. G.; Hinderliter, P. M.; Orr, G.; Thrall, B. D.; Pounds, J. G., Particokinetics In Vitro: Dosimetry Considerations for In Vitro Nanoparticle Toxicity Assessments. *Toxicol. Sci.* **2007**, 95, (2), 300-312.
45. Luoma, S. N. *Silver Nanotechnologies and the Environment: Old problems or New Challenges?* Woodrow Wilson International Center for Scholars. 2008.
46. Tinke, A. P.; Govoreanu, R.; Vanhoutte, K., Particle Size and Shape Characterization of Nano and Submicron Liquid Dispersions. *American Pharmaceutical Review* **2006**, September/October.
47. Wijnhoven, S. W. P.; Peijnenburg, W. J. G. M.; Herberts, C. A.; Hagens, W. I.; Oomen, A. G.; Heugens, E. H. W.; Roszek, B.; Bisschops, J.; Gosens, I.; Van De Meent, D.; Dekkers, S.; De Jong, W. H.; van Zijverden, M.; Sips, A. J. A. M.; Geertsma, R. E., Nano-silver – a review of available data and knowledge gaps in human and environmental risk assessment. *Nanotoxicology* **2009**, 3, (2), 109 - 138.
48. Xu, R. L., Progress in nanoparticles characterization: Sizing and zeta potential measurement. *Particuology* **2008**, 6, (2), 112-115.
49. Burdett, G. J.; Rood, A. P., A membrane filter, direct-transfer technique for the analysis of asbestos fibers or other inorganic particles by transmission electron microscopy. *Environ Sci Technol* **1983**, 17, 643-648.

50. Hudson, P. K.; Gibson, E. R.; Young, M. A.; Kleiber, P. D.; Grassian, V. H., A Newly Designed and Constructed Instrument for Coupled Infrared Extinction and Size Distribution Measurements of Aerosols. *Aerosol Science and Technology* **2007**, 41, (7), 701 - 710.
51. Chang, T., Radial breathing mode frequency of single-walled carbon nanotubes under strain. *Applied Physics Letters* **2008**, 93, (6), 061901-3.
52. Maejima, K.; Suzuki, O.; Uchida, T.; Aoki, N.; Tachibana, M.; Ishibashi, K.; Ochiai, Y., Raman and Transport Studies in Multi-Walled Carbon Nanotubes. *Journal of Physics: Conference Series* **2006**, 28, 33.
53. Schmall, L. H.; Elzey, S.; Grassian, V. H.; O'Shaughnessy, P. T., Nanoparticle aerosol generation methods from bulk powders for inhalation exposure studies. *Nanotoxicology* **2009**.
54. Hunter, R. J., *Introduction to Modern Colloid Science*. Oxford University Press: Oxford, England, 1993.
55. Liz-Marzán, L. M.; Giersig, M.; Mulvaney, P., Homogeneous silica coating of vitreophobic colloids. *Chemical Communications* **1996**, 731.
56. Roca, M.; Haes, A. J., Silica-Void-Gold Nanoparticles: Temporally Stable Surface-Enhanced Raman Scattering Substrates. *Journal of the American Chemical Society* **2008**, 130, (43), 14273-14279.
57. McCreanor, J.; Cullinan, P.; Nieuwenhuijsen, M. J.; Stewart-Evans, J.; Malliarou, E.; Jarup, L.; Harrington, R.; Svartengren, M.; Han, I.-K.; Ohman-Strickland, P.; Chung, K. F.; Zhang, J., Respiratory Effects of Exposure to Diesel Traffic in Persons with Asthma. *N Engl J Med* **2007**, 357, (23), 2348-2358.
58. Peters, A.; von Klot, S.; Heier, M.; Trentinaglia, I.; Hormann, A.; Wichmann, H. E.; Lowel, H.; the Cooperative Health Research in the Region of Augsburg Study, G., Exposure to Traffic and the Onset of Myocardial Infarction. *N Engl J Med* **2004**, 351, (17), 1721-1730.
59. Schulte, P.; Geraci, C.; Zumwalde, R.; Hoover, M.; Kuempel, E., Occupational Risk Management of Engineered Nanoparticles. *Journal of Occupational and Environmental Hygiene* **2008**, 5, (4), 239-249.
60. Maynard, A. D.; Aitken, R. J., Assessing exposure to airborne nanomaterials: Current abilities and future requirements. *Nanotoxicology* **2007**, 1, (1), 26-41.
61. Hinds, W. C., *Aerosol technology: properties, behavior, and measurement of airborne particles, 2nd Ed.* John Wiley & Sons, Inc.: New York, 1999.
62. Oberdörster, G.; Oberdörster, E.; Oberdörster, J., Nanotoxicology: An Emerging Discipline Evolving from Studies of Ultrafine Particles. *Environ Health Perspectives* **2005**, 113, (7), 823.

63. Ross, A. S.; Teschke, K. A. Y.; Brauer, M.; Kennedy, S. M., Determinants of Exposure to Metalworking Fluid Aerosol in Small Machine Shops. *Ann Occup Hyg* **2004**, 48, (5), 383-391.
64. Peters, T. M.; Elzey, S.; Johnson, R.; Park, H.; Grassian, V. H.; Maher, T.; O'Shaughnessy, P., Airborne Monitoring to Distinguish Engineered Nanomaterials from Incidental Particles for Environmental Health and Safety. *Journal of Occupational and Environmental Hygiene* **2009**, 6, (2), 73-81.
65. Li, M.; Yeom, Y.; Weitz, E.; Sachtler, W. M. H., Possible reasons for the superior performance of zeolite-based catalysts in the reduction of nitrogen oxides. *Journal of Catalysis* **2005**, 235, (1), 201-208.
66. Chen, H.-Y.; Sun, Q.; Wen, B.; Yeom, Y.-H.; Weitz, E.; Sachtler, W. M. H., Reduction over zeolite-based catalysts of nitrogen oxides in emissions containing excess oxygen: Unraveling the reaction mechanism. *Catalysis Today* **2004**, 96, (1-2), 1-10.
67. Song, W.; Li, G.; Grassian, V. H.; Larsen, S. C., Development of Improved Materials for Environmental Applications: Nanocrystalline NaY Zeolites. *Environmental Science & Technology* **2005**, 39, (5), 1214-1220.
68. Iwamoto, M.; Yahiro, H.; Kutsuno, T.; Bunyu, S.; Kagawa, S., Enhancement of Catalytic Activity of Copper Ion-Exchanged Y Type Zeolites for the Decomposition of Nitrogen Monoxide. *Bulletin of the Chemical Society of Japan* **1989**, 62, (2), 583.
69. Li, Y.; Armor, J. N., Catalytic decomposition of nitrous oxide on metal exchanged zeolites. *Applied Catalysis B: Environmental* **1992**, 1, (3), L21-L29.
70. Seiyama, T.; Arakawa, T.; Matsuda, T.; Yamazoe, N.; Takita, Y., Catalytic Reduction of Nitric Oxide with Ammonia over Transition Metal Ion-Exchanged Y Zeolites. *Chemistry Letters* **1975**, 4, (7), 781.
71. Li, G.; Jones, C. A.; Grassian, V. H.; Larsen, S. C., Selective catalytic reduction of NO₂ with urea in nanocrystalline NaY zeolite. *Journal of Catalysis* **2005**, 234, (2), 401-413.
72. Howard, J.; Nicol, J. M., Fourier-transform infrared studies of copper-containing Y zeolites. Dehydration, reduction and the adsorption of ammonia. *J. Chem. Soc., Faraday Trans. 1* **1989**, 85, (6), 1233.
73. Iwamoto, M.; Maruyama, K.; Yamazoe, N.; Selyama, T., Study of metal oxide catalysts by temperature programmed desorption. 2. Chemisorption of oxygen on copper(II) ion-exchanged Y-type zeolites. *Journal of Physical Chemistry* **1977**, 81, (7), 622.
74. Parrillo, D. J.; Fortney, J. P.; Gorte, R. J., A Comparison of Adsorption and Reaction Properties in Cu-ZSM-5 and Cu-Y. *Journal of Catalysis* **1995**, 153, (1), 190-193.
75. Valyon, J.; Hall, W. K., Studies of the Surface Species Formed from NO on Copper Zeolites. *Journal of Physical Chemistry* **1993**, 97, (6), 1204.

76. Wichterlová, B.; Sobalík, Z.; Skokánek, M., Effect of water vapour and ammonia on the solid-solid interaction of Cu oxide with Y-type zeolite: preparation of catalyst for reduction of nitric oxide with ammonia at low temperature. *Applied Catalysis A: General* **1993**, 103, (2), 269-280.
77. Delahay, G.; Kieger, S.; Tanchoux, N.; Trens, P.; Coq, B., Kinetics of the selective catalytic reduction of NO by NH₃ on a Cu-faujasite catalyst. *Applied Catalysis B: Environmental* **2004**, 52, (4), 251-257.
78. Li, G.; Larsen, S. C.; Grassian, V. H., An FT-IR Study of NO₂ Reduction in Nanocrystalline NaY Zeolite: Effect of Zeolite Crystal Size and Adsorbed Water. *Catalysis Letters* **2005**, 103, (1), 23-32.
79. Li, G.; Larsen, S. C.; Grassian, V. H., Catalytic reduction of NO₂ in nanocrystalline NaY zeolite. *Journal of Molecular Catalysis A: Chemical* **2005**, 227, (1-2), 25-35.
80. Gilles, F.; Blin, J. L.; Toufar, H.; Briand, M.; Su, B. L., Double interactions between ammonia and a series of alkali-exchanged faujasite zeolites evidenced by FT-IR and TPD-MS techniques. *Colloids and Surfaces A: Physicochemical and Engineering Aspects* **2004**, 241, (1-3), 245-252.
81. Kwak, J.; Peden, C.; Szanyi, J., Non-thermal Plasma-assisted NO_x Reduction over Na-Y Zeolites: The Promotional Effect of Acid Sites. *Catalysis Letters* **2006**, 109, (1), 1-6.
82. Madia, G.; Koebel, M.; Elsener, M.; Wokaun, A., Side Reactions in the Selective Catalytic Reduction of NO_x with Various NO₂ Fractions. *Industrial & Engineering Chemistry Research* **2002**, 41, (16), 4008-4015.
83. Szanyi, J.; Kwak, J. H.; Moline, R. A.; Peden, C. H. F., The adsorption of NO₂ and the NO+O₂ reaction on Na-Y,FAU: an in situ FTIR investigation. *Physical Chemistry Chemical Physics* **2003**, 5, 4045.
84. Szanyi, J.; Kwak, J. H.; Peden, C. H. F., The Effect of Water on the Adsorption of NO₂ in Na and BaY, FAU Zeolites: A Combined FTIR and TPD Investigation. *The Journal of Physical Chemistry B* **2004**, 108, (12), 3746-3753.
85. Yeom, Y. H.; Henao, J.; Li, M. J.; Sachtler, W. M. H.; Weitz, E., The role of NO in the mechanism of NO_x reduction with ammonia over a BaNa-Y catalyst. *Journal of Catalysis* **2005**, 231, (1), 181-193.
86. Yeom, Y. H.; Wen, B.; Sachtler, W. M. H.; Weitz, E., NO_x Reduction from Diesel Emissions over a Nontransition Metal Zeolite Catalyst: A Mechanistic Study Using FTIR Spectroscopy. *The Journal of Physical Chemistry B* **2004**, 108, (17), 5386-5404.
87. Jones, C. A.; Larsen, S. C., A ¹³C and ¹⁵N Solid State NMR Study of the Reactions of Acetone Oxime Adsorbed on FeZSM-5. *Catalysis Letters* **2002**, 78, (1), 243-249.

88. Sedlmair, C.; Gil, B.; Seshan, K.; Jentys, A.; Lercher, J. A., An in situ IR study of the NO_x adsorption/reduction mechanism on modified Y zeolites. *Physical Chemistry Chemical Physics* **2003**, 5, 1897.
89. Song, W.; Grassian, V. H.; Larsen, S. C., High yield method for nanocrystalline zeolite synthesis. *Chemical Communications* **2005**, 23, 2951.
90. Carl, P. J.; Larsen, S. C., Variable-Temperature Electron Paramagnetic Resonance Studies of Copper-Exchanged Zeolites. *Journal of Catalysis* **1999**, 182, (1), 208-218.
91. Carl, P. J.; Larsen, S. C., EPR Study of Copper-Exchanged Zeolites: Effects of Correlated g- and A-Strain, Si/Al Ratio, and Parent Zeolite. *The Journal of Physical Chemistry B* **2000**, 104, (28), 6568-6575.
92. Gatehouse, B. M.; Livingstone, S. E.; Nyholm, R. S., Infrared spectra of some nitrate-co-ordination complexes. *Journal of the Chemical Society* **1957**, 4222.
93. Li, G.; Xu, M.; Larsen, S. C.; Grassian, V. H., Photooxidation of cyclohexane and cyclohexene in BaY. *Journal of Molecular Catalysis A: Chemical* **2003**, 194, (1-2), 169-180.
94. Urban, M. W., *Vibrational Spectroscopy of Molecules and Macromolecules on Surfaces*. John Wiley & Sons, Inc.: 1993.
95. Wallin, M.; Grönbeck, H.; Lloyd Spetz, A.; Skoglundh, M., Vibrational study of ammonia adsorption on Pt/SiO₂. *Applied Surface Science* **2004**, 235, (4), 487-500.
96. Kosslick, H.; Berndt, H.; Lanh, H. D.; Martin, A.; Miessner, H.; Tuan, V. A.; Jänchen, J., Acid properties of ZSM-20-type zeolite. *Physical Chemistry Chemical Physics* **1994**, 90, 2837.
97. Niwa, M.; Nishikawa, S.; Katada, N., IRMS-TPD of ammonia for characterization of acid site in [beta]-zeolite. *Microporous and Mesoporous Materials* **2005**, 82, (1-2), 105-112.
98. Flentge, D. R.; Lunsford, J. H.; Jacobs, P. A.; Uytterhoeven, J. B., Spectroscopic evidence for the tetraamminecopper(II) complex in a Y-type zeolite. *The Journal of Physical Chemistry* **1975**, 79, (4), 354-360.
99. Anselmann, R., Nanoparticles and nanolayers in commercial applications. *Journal of Nanoparticle Research* **2001**, 3, (4), 329-336.
100. Doumanidis, H., The Nanomanufacturing programme at the National Science Foundation. *Nanotechnology* **2002**, 13, (3), 248-252.
101. Emerich, D. F.; Thanos, C. G., Nanotechnology and medicine. *Expert Opinion on Biological Therapy* **2003**, 3, (4), 655-663.
102. Falkenhagen, D., Small Particles In Medicine. *Artificial Organs* **1995**, 19, (8), 792-794.

103. Lowe, T., The revolution in nanometals. *Advanced Materials & Processes* **2002**, 160, (1), 63-65.
104. McAllister, K.; Sazani, P.; Adam, M.; Cho, M. J.; Rubinstein, M.; Samulski, R. J.; DeSimone, J. M., Polymeric nanogels produced via inverse microemulsion polymerization as potential gene and antisense delivery agents. *Journal of the American Chemical Society* **2002**, 124, (51), 15198-15207.
105. Wiesner, M. R.; Lowry, G. V.; Alvarez, P.; Dionysiou, D.; Biswas, P., Assessing the risks of manufactured nanomaterials. *Environmental Science & Technology* **2006**, 40, (14), 4336-4345.
106. Alvarez, P. J., Nanotechnology in the environment - The good, the bad, and the ugly. *Journal of Environmental Engineering-Asce* **2006**, 132, (10), 1233-1233.
107. Richardson, S. D., Water analysis: Emerging contaminants and current issues. *Analytical Chemistry* **2007**, 79, (12), 4295-4323.
108. Agency for Toxic Substances and Disease Registry (ATSDR), Toxicological profile for silver. In US Department of Health and Human Services; Public Health Service; Agency for Toxic Substances and Disease Registry, Eds. Atlanta, GA, 1990.
109. Benn, T. M.; Westerhoff, P., Nanoparticle silver released into water from commercially available sock fabrics. *Environmental Science & Technology* **2008**, 42, (11), 4133-4139.
110. Asharani, P. V. N.; Gong, Z. Y.; Hande, M. P.; Valiyaveetil, S., Potential health impacts of silver nanoparticles. *Chemical Research in Toxicology* **2007**, 20, (12), 99.
111. Griffitt, R. J.; Luo, J.; Gao, J.; Bonzongo, J. C.; Barber, D. S., Effects of particle composition and species on toxicity of metallic nanomaterials in aquatic organisms. *Environmental Toxicology and Chemistry* **2008**, 27, (9), 1972-1978.
112. Navarro, E.; Piccapietra, F.; Wagner, B.; Marconi, F.; Kaegi, R.; Odzak, N.; Sigg, L.; Behra, R., Toxicity of Silver Nanoparticles to *Chlamydomonas reinhardtii*. *Environmental Science & Technology* **2008**, 42, (23), 8959-8964.
113. Chen, Z.; Meng, H. A.; Xing, G. M.; Chen, C. Y.; Zhao, Y. L.; Jia, G. A.; Wang, T. C.; Yuan, H.; Ye, C.; Zhao, F.; Chai, Z. F.; Zhu, C. F.; Fang, X. H.; Ma, B. C.; Wan, L. J., Acute toxicological effects of copper nanoparticles in vivo. *Toxicology Letters* **2006**, 163, (2), 109-120.
114. Panyala, N. R.; Pena-Mendez, E. M.; Havel, J., Silver or silver nanoparticles: a hazardous threat to the environment and human health? *Journal of Applied Biomedicine* **2008**, 6, (3), 117-129.
115. Skebo, J. E.; Grabinski, C. M.; Schrand, A. M.; Schlager, J. J.; Hussain, S. M., Assessment of metal nanoparticle agglomeration, uptake, and interaction using high-illuminating system. *International Journal of Toxicology* **2007**, 26, (2), 135-141.

116. Chen, K. L.; Elimelech, M., Influence of humic acid on the aggregation kinetics of fullerene (C-60) nanoparticles in monovalent and divalent electrolyte solutions. *Journal of Colloid and Interface Science* **2007**, 309, (1), 126-134.
117. Huang, F.; Gilbert, B.; Zhang, H. H.; Banfield, J. F., Reversible, surface-controlled structure transformation in nanoparticles induced by an aggregation state. *Physical Review Letters* **2004**, 92, (15).
118. Moskovits, M.; Vlckova, B., Adsorbate-induced silver nanoparticle aggregation kinetics. *Journal of Physical Chemistry B* **2005**, 109, (31), 14755-14758.
119. Powers, K. W.; Brown, S. C.; Krishna, V. B.; Wasdo, S. C.; Moudgil, B. M.; Roberts, S. M., Research strategies for safety evaluation of nanomaterials. Part VI. Characterization of nanoscale particles for toxicological evaluation. *Toxicological Sciences* **2006**, 90, (2), 296-303.
120. Zelenyuk, A.; Cai, Y.; Imre, D., From agglomerates of spheres to irregularly shaped particles: Determination of dynamic shape factors from measurements of mobility and vacuum aerodynamic diameters. *Aerosol Science and Technology* **2006**, 40, (3), 197-217.
121. Bottger, P. H. M.; Bi, Z.; Adolph, D.; Dick, K. A.; Karlsson, L. S.; Karlsson, M. N. A.; Wacaser, B. A.; Deppert, K., Electro spraying of colloidal nanoparticles for seeding of nanostructure growth. *Nanotechnology* **2007**, 18, (10).
122. Grassian, V. H., When Size Really Matters: Size-Dependent Properties and Surface Chemistry of Metal and Metal Oxide Nanoparticles in Gas and Liquid Phase Environments. *Journal of Physical Chemistry C* **2008**, 112, (47), 18303-18313.
123. Pease, L. F.; Tsai, D. H.; Zangmeister, R. A.; Zachariah, M. R.; Tarlov, M. J., Quantifying the surface coverage of conjugate molecules on functionalized nanoparticles. *Journal of Physical Chemistry C* **2007**, 111, 17155-17157.
124. Suh, J.; Han, B.; Okuyama, K.; Choi, M., Highly charging of nanoparticles through electro spray of nanoparticle suspension. *Journal of Colloid and Interface Science* **2005**, 287, (1), 135-140.
125. TSI, I., Real-Time Measurement of Nanoparticle Size Distributions using Electrical Mobility Technique. In 2008; Vol. Application Note SMPS-004.
126. Shin, W.; Wang, J.; Mertler, M.; Sachweh, B.; Fissan, H.; Pui, D., Structural properties of silver nanoparticle agglomerates based on transmission electron microscopy: relationship to particle mobility analysis. *Journal of Nanoparticle Research* **2009**, 11, (1), 163-173.
127. Gupta, R. B.; Kompella, U. B., Physical Characterization of Nanoparticles. In *Nanoparticle Technology for Drug Delivery*. Gupta, R. B.; Kompella, U. B., Eds. Taylor & Francis Group: 2006; p 109.

128. Wada, Y.; Totoki, S.; Watanabe, M.; Moriya, N.; Tsunazawa, Y.; Shimaoka, H., Nanoparticle size analysis with relaxation of induced grating by dielectrophoresis. *Optics Express* **2006**, 14, (12), 5755-5764.
129. Gao, X. Y.; Wang, S. Y.; Li, J.; Zheng, Y. X.; Zhang, R. J.; Zhou, P.; Yang, Y. M.; Chen, L. Y., Study of structure and optical properties of silver oxide films by ellipsometry, XRD and XPS methods. *Thin Solid Films* **2004**, 455, 438-442.
130. Frank, B. P.; Saltiel, S.; Hogrefe, O.; Grygas, J.; Lala, G. G., Determination of mean particle size using the electrical aerosol detector and the condensation particle counter: Comparison with the scanning mobility particle sizer. *Journal of Aerosol Science* **2008**, 39, (1), 19-29.
131. Chen, Y.; Wang, C. G.; Ma, Z. F.; Su, Z. M., Controllable colours and shapes of silver nanostructures based on pH: application to surface-enhanced Raman scattering. *Nanotechnology* **2007**, 18, (32).
132. Becher, P.; Schuster, D., *Encyclopedia of Emulsion Technology: Basic Theory, Measurement, Applications*. 1988; Vol. 1.
133. Fornes, J. A., Secondary Minimum Analysis In The DLVO-Theory. *Colloid and Polymer Science* **1985**, 263, (12), 1004-1007.
134. Pettibone, J. B.; Elzey, S.; Grassian, V. H., An Integrated Approach Toward Understanding the Environmental Fate, Transport, Toxicity and Health Hazards of Nanomaterials. In *Nanoscience and Nanotechnology: Environmental and Health Impacts*, Grassian, V. H., Ed. John Wiley & Sons: 2008; p 47.
135. Kuchibhatla, S. V.; Karakoti, A. S.; Seal, S., Colloidal stability by surface modification. *Journal of the Minerals, Metals and Materials Society* **2008**, 57, (12), 52-56.
136. Ozmetin, C.; Copur, M.; Yartasi, A.; Kocakerim, M. M., Kinetic investigation of reaction between metallic silver and nitric acid solutions. *Chemical Engineering & Technology* **2000**, 23, (8), 707-711.
137. Sadrnezhaad, S. K.; Ahmadi, E.; Mozammel, M., Kinetics of silver dissolution in nitric acid from Ag-AU(0.04)-CU0.10 and Ag-Cu-0.23 scraps. *Journal of Materials Science & Technology* **2006**, 22, (5), 696-700.
138. Mueller, N. C.; Nowack, B., Exposure Modeling of Engineered Nanoparticles in the Environment. *Environmental Science & Technology* **2008**, 42, (12), 4447-4453.
139. Chen, X.; Schluesener, H. J., Nanosilver: A nanoparticle in medical application. *Toxicology Letters* **2008**, 176, (1), 1-12.
140. Howe, P. D.; Dobson, S., Silver and Silver Compounds: Environmental Aspects. In United Nations Environment Programme; International Labour Organization; World Health Organization; Inter-Organization Programme for the Sound Management of Chemicals, Eds. Geneva, 2002.

141. Eckelman, M. J.; Graedel, T. E., Silver Emissions and their Environmental Impacts: A Multilevel Assessment. *Environmental Science & Technology* **2007**, 41, (17), 6283-6289.
142. U. S. Environmental Protection Agency, High Production Volume Information System (HPVIS). In Agency, U. S. E. P., Ed. 2006.
143. Asharani, P. V.; Wu, Y. L.; Gong, Z. Y.; Valiyaveetil, S., Toxicity of silver nanoparticles in zebrafish models. *Nanotechnology* **2008**, 19, (25).
144. Lubick, N., Nanosilver toxicity: ions, nanoparticles-or both? *Environmental Science & Technology* **2008**, 42, (23), 8617-8617.
145. Grassian, V. H., New Directions: Nanodust - A source of metals in the atmospheric environment? *Atmospheric Environment* **2009**, 43, (30), 4666-4667.
146. Tsai, C. J.; Wu, C. H.; Leu, M. L.; Chen, S. C.; Huang, C. Y.; Tsai, P. J.; Ko, F. H., Dustiness test of nanopowders using a standard rotating drum with a modified sampling train. *Journal of Nanoparticle Research* **2009**, 11, (1), 121-131.
147. Schneider, T.; Jensen, K. A., Combined single-drop and rotating drum dustiness test of fine to nanosize powders using a small drum. *Annals of Occupational Hygiene* **2008**, 52, (1), 23-34.
148. Meskhidze, N.; Chameides, W. L.; Nenes, A.; Chen, G., Iron mobilization in mineral dust: Can anthropogenic SO₂ emissions affect ocean productivity? *Geophysical Research Letters* **2003**, 30, (21), 2085.
149. Meskhidze, N.; Chameides, W. L.; Nenes, A., Dust and pollution: A recipe for enhanced ocean fertilization? *Journal of geophysical research* **2005**, 110, D03301.
150. Englert, B. C., Nanomaterials and the environment: uses, methods and measurement. *Journal of Environmental Monitoring* **2007**, 9, (11), 1154-1161.
151. Hussain, S. M.; Braydich-Stolle, L. K.; Schrand, A. M.; Murdock, R. C.; Yu, K. O.; Mattie, D. M.; Schlager, J. J.; Terrones, M., Toxicity Evaluation for Safe Use of Nanomaterials: Recent Achievements and Technical Challenges. *Advanced Materials* **2009**, 21, (16), 1549-1559.
152. Meulenkamp, E. A., Size dependence of the dissolution of ZnO nanoparticles. *Journal of Physical Chemistry B* **1998**, 102, (40), 7764-7769.
153. Wang, J. X.; Liu, Y.; Jiao, F.; Lao, F.; Li, W.; Gu, Y. Q.; Li, Y. F.; Ge, C. C.; Zhou, G. Q.; Li, B.; Zhao, Y. L.; Chai, Z. F.; Chen, C. Y., Time-dependent translocation and potential impairment on central nervous system by intranasally instilled TiO₂ nanoparticles. *Toxicology* **2008**, 254, (1-2), 82-90.
154. Grassian, V. H., *Nanoscience and Nanotechnology: Environmental and Health Impacts*. John Wiley & Sons: Hoboken, NJ, 2008.

155. Lee, W. M.; An, Y. J.; Yoon, H.; Kweon, H. S., Toxicity and bioavailability of copper nanoparticles to the terrestrial plants mung bean (*Phaseolus radiatus*) and wheat (*Triticum aestivum*): Plant agar test for water-insoluble nanoparticles. *Environmental Toxicology and Chemistry* **2008**, 27, (9), 1915-1921.
156. Agasti, S. S.; Chompoosor, A.; You, C. C.; Ghosh, P.; Kim, C. K.; Rotello, V. M., Photoregulated Release of Caged Anticancer Drugs from Gold Nanoparticles. *Journal of the American Chemical Society* **2009**, 131, (16), 5728.
157. Rieter, W. J.; Taylor, K. M. L.; Lin, W. B., Surface modification and functionalization of nanoscale metal-organic frameworks for controlled release and luminescence sensing. *Journal of the American Chemical Society* **2007**, 129, (32), 9852.
158. Lieberman, H. A., *Pharmaceutical Dosage Forms: Disperse Systems*. Informa HealthCare: Livingston, NJ, 1996; Vol. 2.
159. Tinke, A. P.; Vanhoutte, K.; De Maesschalck, R.; Verheyen, S.; De Winter, H., A new approach in the prediction of the dissolution behavior of suspended particles by means of their particle size distribution. *Journal of Pharmaceutical and Biomedical Analysis* **2005**, 39, (5), 900-907.
160. Johnson, A.; Greenwood, P.; Hagstrom, M.; Abbas, Z.; Wall, S., Aggregation of Nanosized Colloidal Silica in the Presence of Various Alkali Cations Investigated by the Electro spray Technique. *Langmuir* **2008**, 24, (22), 12798-12806.
161. Tsai, D. H.; Pease, L. F.; Zangmeister, R. A.; Tarlov, M. J.; Zachariah, M. R., Aggregation Kinetics of Colloidal Particles Measured by Gas-Phase Differential Mobility Analysis. *Langmuir* **2009**, 25, (1), 140-146.
162. Pettibone, J. M.; Adamcakova-Dodd, A.; Thorne, P. S.; O'Shaughnessy, P. T.; Weydert, J. A.; Grassian, V. H., Inflammatory response of mice following inhalation exposure to iron and copper nanoparticles. *Nanotoxicology* **2008**, 2, (4), 189-204.
163. Zheng, H.; Smith, R. K.; Jun, Y.-w.; Kisielowski, C.; Dahmen, U.; Alivisatos, A. P., Observation of Single Colloidal Platinum Nanocrystal Growth Trajectories. *Science* **2009**, 324, (5932), 1309-1312.
164. Holm, J.; Roberts, J. T., Surface chemistry of aerosolized silicon nanoparticles: Evolution and desorption of hydrogen from 6-nm diameter particles. *Journal of the American Chemical Society* **2007**, 129, 2496-2503.
165. Holm, J.; Roberts, J. T., Thermal Oxidation of 6 nm Aerosolized Silicon Nanoparticles: Size and Surface Chemistry Changes. *Langmuir* **2007**, 23, (22), 11217-11224.
166. Zhang, B.; Liao, Y.-C.; Girshick, S. L.; Roberts, J. T., Growth of coatings on nanoparticles by photoinduced chemical vapor deposition. *Journal of Nanoparticle Research* **2008**, 10, (1), 173.

167. Gilbert, B.; Huang, F.; Zhang, H.; Waychunas, G. A.; Banfield, J. F., Nanoparticles: Strained and Stiff. *Science* **2004**, 305, (5684), 651-654.
168. Chen, Z.; Meng, H.; Xing, G.; Chen, C.; Zhao, Y.; Jia, G.; Wang, T.; Yuan, H.; Ye, C.; Zhao, F.; Chai, Z.; Zhu, C.; Fang, X.; Ma, B.; Wan, L., Acute toxicological effects of copper nanoparticles in vivo. *Toxicology Letters* **2006**, 163, (2), 109-120.
169. Griffitt, R. J.; Weil, R.; Hyndman, K. A.; Denslow, N. D.; Powers, K.; Taylor, D.; Barber, D. S., Exposure to Copper Nanoparticles Causes Gill Injury and Acute Lethality in Zebrafish (*Danio rerio*). *Environmental Science & Technology* **2007**, 41, (23), 8178-8186.
170. Lüderitz, V.; Nicklisch, A., The Effect of pH on Copper Toxicity to Blue-Green Algae. *Internationale Revue der gesamten Hydrobiologie und Hydrographie* **1989**, 74, (3), 283-291.
171. Swain, G. W. J.; Farrar, R. A.; Hutton, S. P., The use of controlled copper dissolution as an anti-fouling system. *Journal of Materials Science* **1982**, 17, (4), 1079-1094.
172. Singh, N., Effect of pH on the Tolerance of *Penicillium nigricans* to Copper and Other Heavy Metals *Mycologia* **1977**, 69, (4), 750.
173. Thomas, V. G.; McGill, I. R., Dissolution of copper, tin, and iron from sintered tungsten-bronze spheres in a simulated avian gizzard, and an assessment of their potential toxicity to birds. *Science of The Total Environment* **2008**, 394, (2-3), 283-289.
174. Starkey, R. L., Effect of pH on Toxicity of Copper to *Scytalidium* sp., a Copper-tolerant Fungus, and Some Other Fungi. *J Gen Microbiol* **1973**, 78, (2), 217-225.
175. Fleet, M. E., The Crystal Structure of Paratacamite, $\text{Cu}_2(\text{OH})_3\text{Cl}$. *Acta Crystallographica B* **1975**, B31, 183.
176. Jambor, J. L.; Dutrizac, J. E.; Roberts, A. C.; Grice, J. D.; Szymanski, J. T., Clinoatacamite, a new polymorph of $\text{Cu}_2(\text{OH})_3\text{Cl}$, and its relationship to paratacamite and "anarakite". *Can Mineral* **1996**, 34, (1), 61-72.
177. Casaletto, M. P.; De Caro, T.; Ingo, G. M.; Riccucci, C., Production of reference "ancient" Cu-based alloys and their accelerated degradation methods. *Applied Physics A: Materials Science & Processing* **2006**, 83, (4), 617-622.
178. Tronner, K.; Nord, A. G.; Borg, G. C., Corrosion of archaeological bronze artefacts in acidic soil. *Water, Air, & Soil Pollution* **1995**, 85, (4), 2725-2730.
179. Scott, D. A., Bronze Disease: A Review of Some Chemical Problems and the Role of Relative Humidity. *Journal of the American Institute for Conservation* **1990**, 39, (2), 193.

180. Han, M. S.; Lee, B. G.; Ahn, B. S.; Kim, H. S.; Moon, D. J.; Hong, S. I., The role of copper chloride hydroxides in the oxidative carbonylation of methanol for dimethyl carbonate synthesis. *Journal of Molecular Catalysis A: Chemical* **2003**, 203, (1-2), 137-143.
181. Punnoose, A.; Seehra, M. S.; Dunn, B. C.; Eyring, E. M., Characterization of $\text{CuCl}_2/\text{PdCl}_2/\text{Activated Carbon}$ Catalysts for the Synthesis of Diethyl Carbonate. *Energy & Fuels* **2001**, 16, (1), 182-188.
182. Briggs, D. N.; Lawrence, K. H.; Bell, A. T., An investigation of carbon-supported $\text{CuCl}_2/\text{PdCl}_2$ catalysts for diethyl carbonate synthesis. *Applied Catalysis A: General* **2009**, 366, (1), 71-83.
183. Olejniczak, J.; Staniewski, J.; Szymanowski, J., Extraction of phenols and phenyl acetates with diethyl carbonate. *Analytica Chimica Acta* **2005**, 535, (1-2), 251-257.
184. Delledonne, D.; Rivetti, F.; Romano, U., Developments in the production and application of dimethylcarbonate. *Applied Catalysis A: General* **2001**, 221, (1-2), 241-251.
185. Lee, S. C.; Park, S. H.; Lee, S. M.; Lee, J. B.; Kim, H. J., Synthesis and H_2 uptake of $\text{Cu}_2(\text{OH})_3\text{Cl}$, $\text{Cu}(\text{OH})_2$ and CuO nanocrystal aggregate. *Catalysis Today* **2007**, 120, (3-4), 358-362.
186. Brigandi, L. M.; Leber, P. A.; Yoder, C. H., Synthesis and Analysis of Copper Hydroxy Double Salts. *Journal of Chemical Education* **2005**, 82, (11), 1662.
187. Pollard, A. M.; Thomas, R. G.; Williams, P. A., Synthesis and stabilities of the basic copper(II) chlorides atacamite, paratacamite and botallackite. *Mineralogical Magazine* **1989**, 53, 557.
188. Elzey, S.; Grassian, V., Agglomeration, isolation and dissolution of commercially manufactured silver nanoparticles in aqueous environments. *Journal of Nanoparticle Research*. DOI: 10.1007/s11051-009-9783-y.
189. Downs, R. T. The RRUFF Project: an integrated study of the chemistry, crystallography, Raman and infrared spectroscopy of minerals. Program and Abstracts of the 19th General Meeting of the International Mineralogical Association in Kobe, Japan. O03-13. <http://rruff.info/>.
190. Sasai, J.; Tanaka, K.; Hirao, K., Preparation and second-order nonlinear optical properties of CuCl nanocrystal-doped glass films. *Scripta Materialia* **2001**, 44, (8-9), 1225-1228.